COPYRIGHT STATEMENT

COMPOSITE MATERIALS FILLED WITH FERROMAGNETIC MICROWIRE INCLUSIONS DEMONSTRATING MICROWAVE RESPONSE TO TEMPERATURE AND TENSILE STRESS

By

Vlad Zamorovskii

A thesis submitted to Plymouth University
in partial fulfilment of the degree of

MASTER OF PHILOSOPHY

School of Marine Science and Engineering
Plymouth University

May 2017

Acknowledgements

I would like to thank my supervisors Dr John Summerscales, Dr Dmitriy Makhnovskiy, and Dr Mansel Davies for their guidance and support throughout this research project.

I would also like to thank Mr Terry Richards and Mr Nicholas Fry for all their help during stress and impedance experiments. Special thanks to Dr Richard Cullen for his help and ideas during the manufacture of epoxy resin composite samples. I also wish to express my sincere gratitude to Mr John Eastment for his assistance with electronic circuit design.

I would like to thank Dr Dmitriy Makhnovskiy additionally for arranging a very memorable visit to MFTI Ltd. I would also like to thank Mr Vladimir Larin and his colleagues, for their hospitality and their time spent on making my visit to MFTI Ltd interesting and informative.

Author's Declaration

At no time during the registration for the degree of Master of Philosophy has the author been registered for any other University award without prior agreement of the Graduate Committee.

Work submitted for this research degree at the Plymouth University has not formed part of any other degree either at Plymouth University or at another establishment.

Chapter II of this thesis titled "Embedded ferromagnetic microwires for monitoring tensile stress in polymeric materials" is based on a paper published in the scientific journal "Composites Part A: Applied Science and Manufacturing" in June 2014.

An international trade fair and forum (details below) was attended for the purpose of investigating current technologies in the field of non-destructive testing (NDT) of composites.

Publications:

D. Makhnovskiy, V. Zamorovskii, J. Summerscales, *"Embedded ferromagnetic microwires for monitoring tensile stress in polymeric materials"*, Composites Part A: Applied Science and Manufacturing, V. 61, pp. 216–223, (2014).

Research trips:

Microwire company – "Microfir Tehnologii Industriale" (MFTI Ltd), Chisinau, Republic of Moldova, 14-16 April 2013.

10th European Trade Fair & Forum for Composites, Messe Stuttgart, Germany, 22-24 September 2015.

Word count of main body of thesis: ~ 26,000

Signed: Vlad Zamorovskii

Table of contents

List of figures and tables

Chapter I

Chapter II

Chapter III

Chapter IV

Chapter V

Appendix

Abstract

Amorphous and polycrystalline microwires cast from ferromagnetic Fe-based or Co-based alloys in glass envelope demonstrate unique magneto-anisotropic and high frequency impedance properties that make them very attractive for sensor applications. Magnetic anisotropies of different types result from the inverse magnetostriction effect (positive or negative) at the interface between the glass shell and the metal core, in the presence of the residual stresses induced during the Taylor-Ulitovski casting method. Therefore, the glass shell is not just isolation, but also is one of most important factors that defines the physical properties of microwires. In particular, magnetic anisotropy allows high frequency impedance to be tuned by external stimuli such as magnetic field, tensile stress, or temperature. In the project, these effects are explored for the creation of low density microwire inclusions that might introduce tuneable microwave properties to polymer composite materials.

The project aims to study high frequency impedance effects in ferromagnetic wires in the presence of tensile stress, temperature, and magnetic field. The integration of microwave equipment with mechanical and thermal measurement facilities is a very challenging task. In the project, we develop new experimental techniques allowing comprehensive study of composite materials with electromagnetic functionalities. The wire surface impedance recovered from such measurements can then be used to model the microwave response from wire-filled composites in free space. The obtained results significantly expand the horizon of potential applications of ferromagnetic wires for structural health monitoring.

Chapter I

A review on glass-coated ferromagnetic microwires

"This chapter will introduce microwires to the reader and explore some important fabrication technology processes relevant to understanding their properties. A visit to the Moldovan company, MFTI Ltd, currently the main producer of microwire, with which this research project started will also be briefly described. The principal facts presented in this chapter have been compiled from the book "Cast microwire and its properties (see [1.1])".

1.1. Introduction

Metal or metal alloy microwire in glass insulation is currently one of the prospective materials which allow solving problems in relation to miniaturisation, increasing precision and stability, and expansion of the acceptable range of mechanical effects in instrumentation.

Ultra-thin glass-coated microwires, with a typical core diameter of 3-50 μm (microns) and the thickness of glass shell of 2-10 microns, provide significant reduction of weight and dimension of components made of microwire and reduce their mechanical, thermal and electrical inertia. The continuous glass insulation protects the core material from external effects and is a prerequisite for the long-term stability, high reliability and accuracy of these components. High mechanical strength of the microwire is a guarantee of its processability in an industrial production environment and the relatively low cost makes microwire components economical.

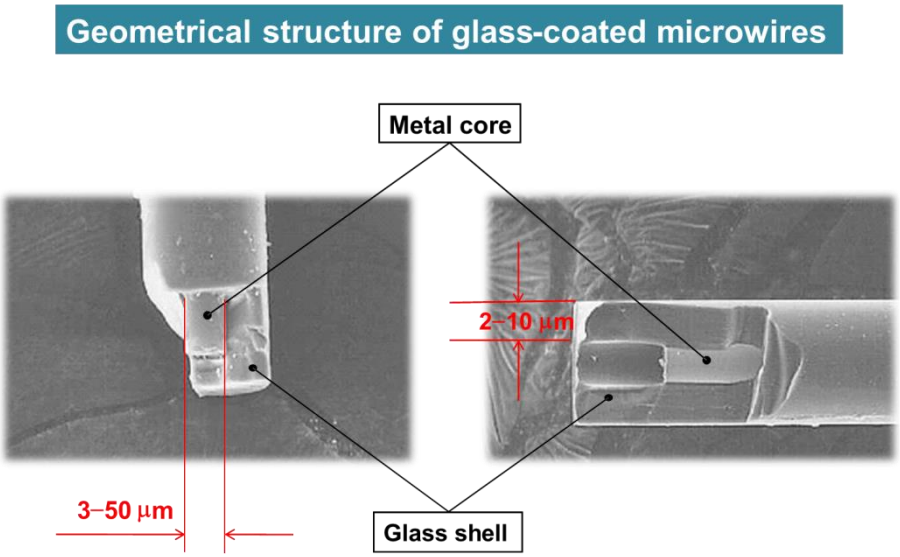

Fig. 1.1. Geometrical structure of a typical microwire in a glass shell [1.2].

1.1 A brief history of the microwire technology

The first thin metallic filaments (from liquid phase of the metal) in glass insulation were derived by Taylor in 1924 [1.3]. The method of obtaining microwires was improved by Makovsky in 1940. The principle of this method lays in the heating of a metal sample inside a horizontally positioned glass tube with a gas burner till the softening of the tube and the melting of the metal followed by rapid stretching of the tube. This method did not receive wide acceptance, as it produced microwires of limited lengths and their parameters were uncontrollable. A new method of casting of microwires was proposed by Ulitovski in 1948 [1.4]. The essence of this method is that a continuous liquid metal filling the capillary is drawn out from a vertically positioned glass tube. A metal sample is suspended in a high-frequency electromagnetic field, which heats it by the induced eddy currents and potentially permits obtaining microwires of long segments. The next major step was the establishment of the Research Institute of Electro-Instrumentation and the factory "Microwire" in 1958-59 in Chisinau, Moldova. This created the conditions for carrying out complex investigations of the casting process of microwire, leading to industrial technology for production and a comprehensive study of the properties and the development of methods and equipment for research and control. The scale of these works was associated with a constant increase in the volume of industrial production of components and devices made of microwires. In the early 1960's some research work in the field of microwires also appeared in Britain, Germany, France, USA and Japan. A Japanese company, UNITIKA Ltd, mass produces amorphous microwires but using different technology and without a glass shell.

1.2. Visit to “Microfir Tehnologii Industriale” (MFTI Ltd), Chisinau, Moldova, 14-16 April 2013

To gain first-hand knowledge about different glass-coated microwires, their design and features, along with understanding the various equipment and technologies involved during their manufacture, the research project included a visit to “Microfir Tehnologii Industriale” Ltd – currently the main provider of glass-coated microwires.

“Microfir Tehnologii Industriale” Ltd (www.microwires.com) is a R&D company with small production facility located in Chisinau, capital of Moldova. MFTI Ltd was founded in 2002, having accumulated vast experience and knowledge in the field of microwires in glass shells over 40 years of their production, research and applications. Visit to MFTI Ltd along with discussions with the company’s director, Mr Vladimir Larin, were a critical starting point of the research. Also, during this visit, glass-

coated ferromagnetic microwires with specific properties were manufactured, specifically for use in experiments of this research project.

As the Soviet Union disintegrated, well-established economic ties between the Soviet republics were destroyed and Moldova became one of the poorest countries in Europe [1.5]. During the Soviet period, technological and human resources potential that could solve complex economic problems within the planning system were formed in the republics. In the years following the disintegration, uncontrollable destruction and consequent aging of that potential took place. However, the foundation laid proved strong enough to survive even this difficult period. It was possible to retain a number of industries and create new national intellectuals. Even though the scope of tasks and funding were significantly reduced, scientific and production teams remained functional. In particular, Moldova inherited the unique high-tech production of the finest microwire of various alloys in glass shell that will be discussed in this work.

On the morning of 14 April 2013 at MFTI Ltd I met Mr Vladimir Larin. Vladimir Larin and his colleagues described the history of MFTI Ltd and the various activities in the field of research and production of the glass-coated ferromagnetic microwires that the company produced, and the fundamental physics concepts involved in their casting technology. Several technicians and experts from other scientific fields such as electronics, rheology and microscopy, introduced the different sciences involved in the fabrication of the microwires.

The main work that MFTI Ltd is involved in could be categorised into three main sections:

1. Industrial-scale production of glass-coated microwires for use in:
    a. Precision resistor elements for metrology measurements
    b. Fillers for composite materials that demonstrate wideband RF absorbing properties (“stealth technology”)
    c. Magnetic tags for fraud protection
    d. High sensitivity magnetic-field sensors based on the giant magnetoimpedance (GMI) effect
    e. Strain and displacement sensors
    f. Gas analyser and temperature sensors (micro-thermocouples)
2. Development and manufacture of equipment for production of microwires, i.e. microwire casting machine and control systems.
3. Development of equipment for quality control and winding of microwires.

This research project may be of interest to the company for their activities related with 1(b, d and e). During day one of the visit, a tour of the company facilities included areas such as the shop floor and those involved with production and testing of microwires. This was perfect opportunity to (i) understand and document the processes and equipment involved in the design, production and testing of the microwires, (ii) to witness first-hand from start to finish the microwire casting fabrication process of glass-coated ferromagnetic microwires, (iii) to obtain a clear overview of the entire production cycle of microwires, and (iv) understand more about the company, its business function and contributions to the local community, in terms of economics and local employment.

The second day involved a more in-depth investigation of the Taylor-Ulitovski fabrication technique of continuous glass-coated ferromagnetic microwires and the microwire casting machine, which uses this principle. A technician demonstrated operating a microwire casting machine and explained every feature of this unique equipment as continuous glass-coated microwires were formed and simultaneously wound onto a rotating bobbin.

The microwire casting machine also had a sort of a Manufacturing Execution System (MES), which provided real-time feedback and information from various sensors to a liquid-crystal display. The data displayed could be used for quality management and to make real-time changes to processes. The advantages and complexities of using microwire casting machines to produce glass-coated microwires were explained. A principal of the visit was to obtain information for the thesis detailing the microwire casting process machine and the microwire casting machine.

On the final day of the visit, the various quality inspections carried out on the microwire were observed. A small device was used post-production for measuring and confirming the diameters of microwires. A computer would produce graphical representations of thickness along the length of the microwire as it passed through this device. Another method for quick investigations of the diameters of glass-coated microwire segments, along with the thicknesses of the outer glass shells and the metal core post-production, was by the means of a microscope (see Fig. 1.2). A microwire was fixed on a glass plate and, with the help of a crosshair, various measurements of the microwire segments could be recorded. It was a simple and effective process.

Fig. 1.2. Optical inspection of microwires and their structural features. A piece of equipment from Soviet epoch – still works!

The microwire winding and rewinding processes such as from one reel onto another, or from bobbins, which initially collect microwires during their fabrication, onto reels for the purposes of storage or shipment were observed. This was done at high speed, using special devices. There was no apparent damage to the microwires during such high-speed industrial-scale processes.

Later, glass-coated ferromagnetic microwires suitable for this research project were manufactured. The high frequency measurement technique used to check impedance properties of microwires was introduced. During these demonstrations, basic impedance characteristics in the presence of stress and magnetic field were observed using a HP8720 Vector Network Analyser (VNA) and a solenoid coil (see Fig. 1.3).

Fig. 1.3. Demonstrations of microwire impedance properties using a VNA and solenoid coil.

Appendix A (see page 125) describes the journey and stay in Chisinau, Republic of Moldova and the journey from Chisinau, Republic of Moldova to Plymouth, United Kingdom (see page 126). During this visit to MFTI Ltd, the first-hand knowledge gained about microwires and their manufacture process was invaluable. Brief closing thoughts regarding this visit are also included in this appendix.

1.3. Taylor-Ulitovski method of casting of glass-coated microwires

One way of acquiring thin metal filaments is by pulling of molten metals in a viscous glass shell as first described by Taylor in 1924 [1.3]. In the Taylor patent application, there was a provision for the possibility of obtaining thin conductors in glass isolations in the form of short metal segments, the melting point of which was 150-200 °C below the softening temperature of the glass used [1.6].

In 1948 Ulitovski et al offered a new method of glass-coated cast microwire production [1.4]. The nature of formation of glass-coated microwire in his method (see Fig. 1.4) can be summarised as follows. A sample of metal of a few grams (see Fig. 1.4(a)) is placed in a glass tube which is then introduced into an inductor powered by a high-frequency generator (hundreds kiloHertz). Eddy currents remotely induced in the metal sample by the inductor heats it to the melting point and also soften adjoining walls of the glass tube. Depending on the properties of the metal used and the size of the obtained microwire, the quantity of metal in the micro-bath, i.e. droplets of molten metal in viscous glass shell at the end of the glass tube, can be continuously restored by a metal rod fed into it, as shown in Fig. 1.4(b) and Fig. 1.5. As a result of the mentioned methods of metal filling, the processes for obtaining microwire are categorised as either "drop" or "continuous."

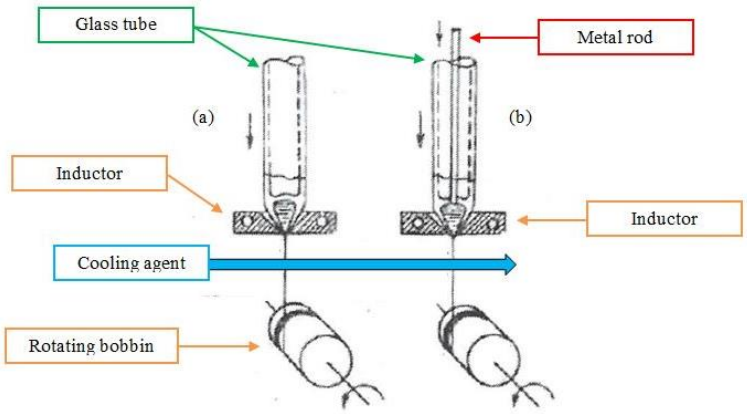

Fig. 1.4. Obtaining microwire in glass shell from melted metals by the Ulitovski method. (a) – “Drop” method; (b) – “Continuous” method. [1.1]

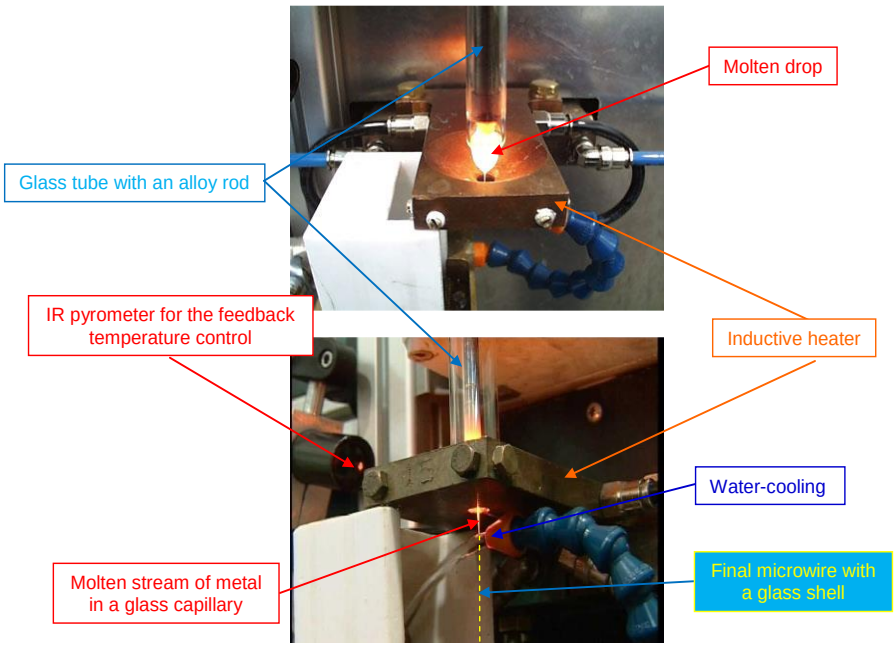

Fig. 1.5. A practical realisation of the continuous method (MFTI Ltd).

As well as melting the metal, the magnetic field of the inductor maintains the metal centrally in the inductor in a suspended state in the form of a micro-bath. Further, by touching the base of the micro-bath with a glass rod, as shown in Fig. 1.6, part of its shell is pulled on to a spool of a special receiving device (a rotating bobbin) as a glass capillary with a solid metal filling in the form of a continuous metal or metal alloy core. On the way from the micro-bath towards the spool of the receiving device, the microwire passes through a “crystalliser” in the form of a cooling agent jet such as water or inorganic oil. The process of forming a glass capillary is carried out continuously at the expense of glass, which is pulled from the surface of the micro-bath, during which the consumption of the glass is evenly compensated by the continuous supply of glass tube into the area of the inductor. Metal consumption to form the microwire core is limited by the initial sample in the micro-bath. Periodic replenishment disrupts the casting process of microwire and requires a new set-up process.

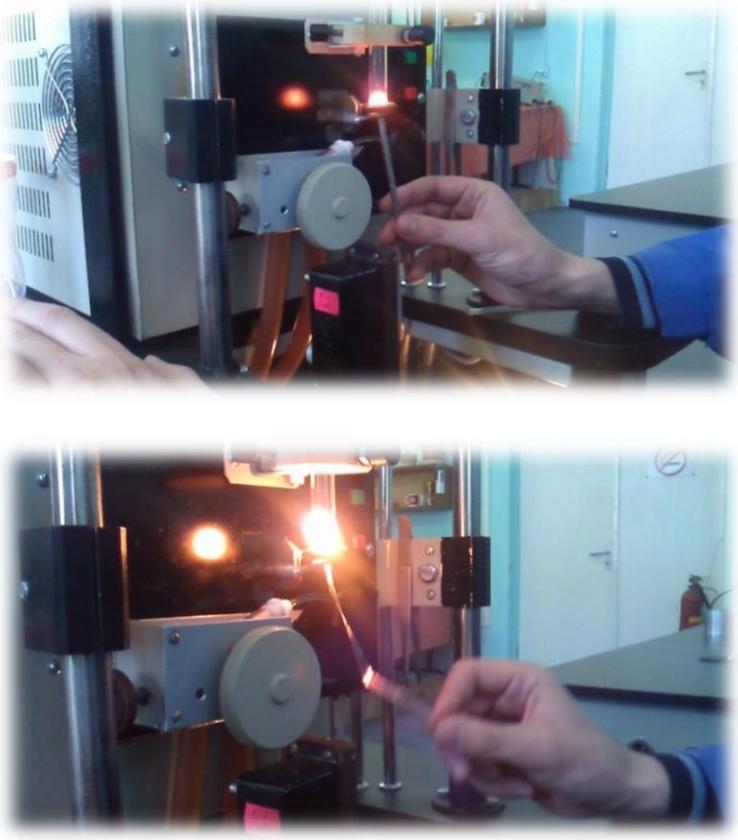

Fig. 1.6. Casting machine that utilises the Taylor-Ulitovski method. Continuous glass coated microwire is obtained by pulling from the melt micro-bath with subsequent cooling when passing through the water stream.

1.4. Physicochemical changes during microwire casting

The formation of the microwire within glass insulation has a complex dependency on physical and chemical processes occurring in the micro-bath under the influence of the high temperatures and the magnetic field of the high-frequency inductor.

Cast microwire is a metal core (pure metals or alloys preferably with a reduced content of soluble gases across the entire length) having an insulating coating in the form of a continuous glass shell. At the boundary of the core and the glass envelope there must be a uniform transition layer, consisting of a chemical solution of the glass shell elements and a conductive filament based on lower order oxides. A successful microwire with set parameters is closely linked to stabilisation of the chemical composition of the raw materials during the casting process. Alloys compositions must be chosen taking the specific characteristics of the microwire casting technology into consideration.

Every microwire alloy has specific technological casting process mode characteristics, dependent on the physical and chemical properties of the metal-glass pair. The technological casting process is generally characterised by a number of factors, the combined effect of which is determined by the parameters of the required microwire. Figure 1.7 summarises the factors influencing mechanical, physical, and chemical properties of microwires. In this project, the principal interest is magneto-anisotropic and conductive properties. The former will be defined by alloy compositions and the residual stresses between the core and glass shell induced during the casting process (due to the well-known magneto-striction effect, i.e. the property of ferromagnetic materials which causes them to undergo microscopic distortion in their molecular structures when subjected to a magnetic field [1.7]). In principle, while working with ready-made microwire samples it is necessary to consider how the thickness of glass, the composition of alloy, its dependence on the temperature and external stretching stress and the speed of crystallisation (amorphous and polycrystalline structure) can influence the type of magnetic anisotropy. However, all process parameters shown in Fig 1.7 can be taken into account only by an experienced technologist. As a result of the many years of MFTI Ltd expertise, it was possible to focus this project on sensor applications and not delve over technological details. MFTI Ltd cooperates with many physics laboratories, in a similar way, providing them with microwire samples for research. On the other hand, the measurements of physical properties allow correcting the microwire moulding technology and adapting it to the specific applications.

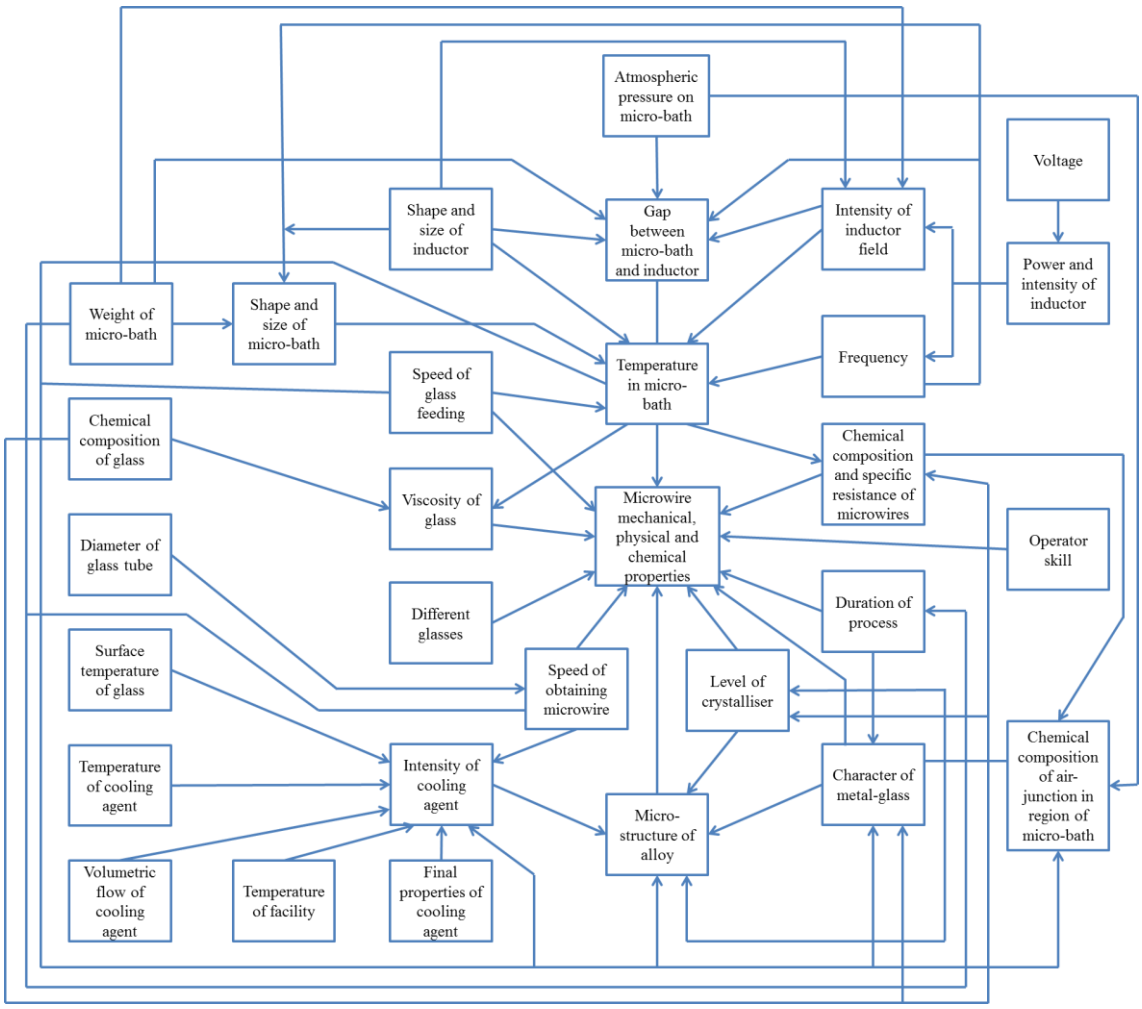

Fig. 1.7. Diagram of the factors of the technological process influencing mechanical, physical, and chemical properties of microwires [1.1].

The following section briefly discusses only the most important technological modes. Temperature regime of casting is characterised by the temperature of the start and the end of the process. In the specified temperature range, the formation of glass capillary and its filling with molten alloy takes place. Each metal-glass pair is characterised by a specific temperature range of casting. The microwire casting is carried out while overheating the alloy by 50-250 °C. This value is determined by the casting properties of the alloy, which improve with increase in temperature. Secondary factors such as the generator power and frequency, configuration of the magnetic field, weight of the alloy and pressure on the micro-bath, affect the temperature of the alloy in the micro-bath. A change in weight of micro-bath during the casting process, which results in the change of its temperature, is a typical feature of the drop casting method.

A decrease in temperature of the alloy in micro-bath causes the diameter of the microwire core to increase, as demonstrated in Fig. 1.8 for a manganin alloy. The degree of influence of temperature on the core diameter is not dependent on the glass used for casting. This effect of temperature on the diameters of microwires embedded in glasses with different physical and chemical properties (marked by symbols “A” and “B” in the graph below) investigated in the specified temperature range is the same. The temperature range specified on this graph is determined by the minimum and maximum allowable process temperature.

A noticeable effect of the temperature at the start of the casting process is the time the metal heats in the micro-bath. Sufficiently long exposure creates conditions for obtaining microwire with the core diameter of less than 1 micron.

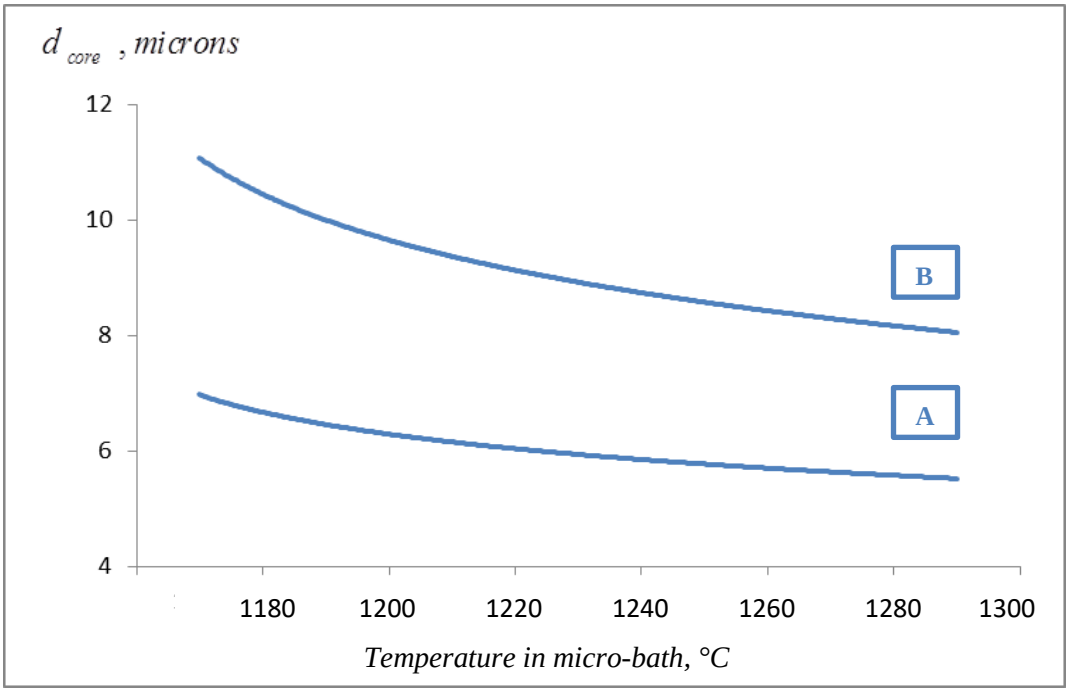

Fig. 1.8. Typical dependence of the core diameter on the temperature measured for two different manganin alloy microwires [1.1] embedded in different glasses represented by symbols “A” and “B”.

If the temperature regime of casting process enables the formation of a glass capillary and filling it with liquid alloy, then the formation of microwire itself occurs under the action of tensile forces that are expended on overcoming of the viscous forces and surface tension of the metal-glass system. The magnitude of the forming force is mainly determined by the tension in the microwire which, in turn, is dependent on the casting speed, i.e. the speed of the microwire exiting the crystallising liquid border. The

influence of the casting speed on the diameter of the core is demonstrated in Fig. 1.9 for a manganin alloy, which shows that with the increase of the casting speed, the core diameter reduces.

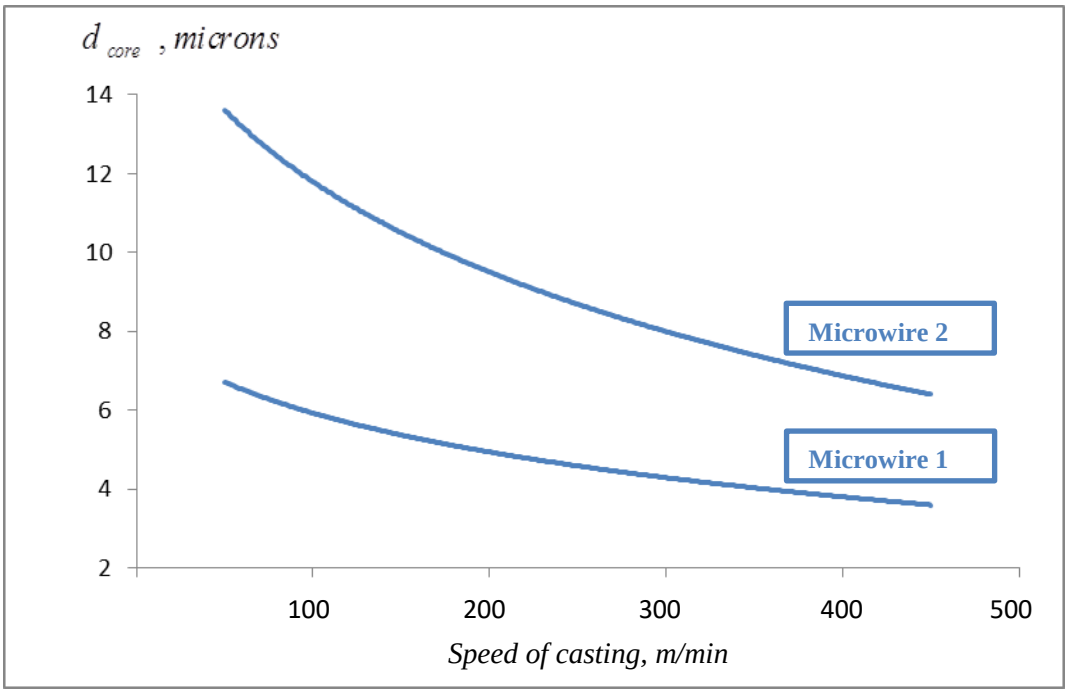

Fig. 1.9. Typical effect of casting speed on the core diameter measured for a manganin alloy microwires [1.1]. "Microwire 1" and "Microwire 2" represent two manganin microwires cast at different speeds.

The minimum microwire casting speed, taking into account the economic indicators of the drop method, should be regarded as 100 m/min. The maximum casting microwire speed is also limited. For example, during manganin microwire casting, the speed should not normally exceed 350 m/min. Increasing the casting speed causes the tension in the microwire to increase. As a result, the glass insulation and the core may experience intensive tension, which at casting speeds above 350 m/min leads to tearing of core, while at speeds exceeding 500 m/min there are frequent breakages of the microwire glass shell itself. The casting speed limits differ for other alloys.

There is another method of fabrication of microwires with a submicron (nanometre) diameter, where equal-length segments of glass-coated microwires are assembled into a bundle, put into a glass tube, and then stretched under proper heating conditions provided by an inductive heater which is similar to that of the usual continuous casting method shown in Figs. 1.4(b) and 1.5 [1.8]. The final structure is a multicore wire with a lattice of nano-wires randomly distributed in its cross section. These structures may be of great interest for sensor applications in the future.

The cooling of the micro-bath as a result of air suction from the inductor zone, or the changing temperature and shape on the account of creation of depression (negative) or extra pressure (positive) in the glass tube, can be viewed as possible channels of influence on the temperature and shape of micro-bath. The casting process productivity and quality of microwire under different conditions are closely linked with the choice of the optimal ratio of the inductor dimensions and glass tubes in use.

1.5. Raw materials for casting of microwire

Possibilities of microwire casting from a particular alloy are determined primarily by the presence of glass possessing the required viscosity in the working range of the casting process, in turn dependent on the melting point of the parent metal. Currently available glasses only allow the use of metals and alloys with a melting point below 1500 °C for casting of microwire. The casting technology itself does not put limitations on the melting point, and the development of materials with higher melting temperature is dependent on the development of appropriate glass.

Currently alloys with a temperature coefficient of expansion up to 20×10^{-6} °C^{-1} are used for microwire casting. Pyrex glass, usually used to manufacture the glass tubes, has a temperature coefficient of expansion of about 4×10^{-6} °C^{-1}. In general, difference between the temperature coefficients of the metal-glass pair expansion should be minimised, especially when casting of microwire with a core diameter above 25 microns. For the creation of magnetic anisotropy, this difference in expansion coefficient becomes important.

Materials used for casting should have a relatively low value of surface and interfacial tension, high adhesion value and coefficient of expansion. Currently, as a result of limited knowledge of these values, it is not possible to specify their exact limits in relation to the conditions of the casting. The manufacturability of a particular metal-glass pair, must take into consideration the ratios between adhesion work at the interface and the surface tension forces of the separate glass phases and the melt at the border with the gas medium. The stronger the forces of the chemical bond at the glass-metal border, the better the glass capillary will be filled with metal. In this case, a smooth formation of the intermediate phase, and surface tension between the metal and glass phases in a certain temperature range, become important.

The choice of glass for microwire casting is determined by many factors: the difference between the Coefficients of Thermal Expansion (CTE) between metal and glass, viscosity in the working

temperature range of the casting process, interfacial tension, crystallisation ability, quality of tubes, etc. Glass viscosity must also be considered as one of the factors that influence the output parameters of microwire, in particular, the thickness of the insulation. Increase in the viscosity increases the thickness of the insulation.

1.6. Typical mechanical properties of microwire

The high rate of crystallisation and micron sizes of microwire determine its mechanical properties. In microwire, the statistical nature of toughness and so-called extensive effects, i.e. the dependence of the durability characteristics on the transverse and longitudinal dimensions of the sample investigated, is clearly seen. The use of microwire in the electronic-measurement has put forward the research objectives of its characteristics such as gauge factor, coefficient of linear thermal expansion, coefficient of microwire friction while in contact with different materials. The description of the structure of the transition layer and the nature of the seam between glass and metal in the microwire are also specifically interesting. In all these questions the theory is not well developed, so results presented are largely semi-empirical. However, this does not reduce their usefulness in engineering applications.

1.6.1 The geometrical parameters of microwire

Geometric parameters of microwire include an outer diameter of insulation D, diameter of the metallic core d, one-sided (wall) thickness of insulation Δ, the ratio of the outer insulation to inner core diameters D/d and the length of the microwire segment on the reel l. Transverse cross-section of a microwire core normally is close to circular cross-section. Research on the eccentricity of core of microwire has not been conducted. However, it is known that the transverse dimensions of microwire do not remain constant along the segment, and represent themselves as random functions of its length. These functions comprise of periodic oscillations of a rather broad spectrum with a wavelength of 10 mm to 10 m. Fluctuations (a few percentage) of the diameter core and glass insulation, on one hand, are the effect of the presence of bubbles, poor fusion of glass, foreign matter, and other irregularities in the uniformity of the raw materials; on the other hand, they reflect casting peculiarities on the existing equipment (fluctuations of temperature, electric modes, wear of the reel, etc.).

The casting process of microwire is accompanied by interaction of the molten metal with the softened glass shell. The nature of this interaction largely determines the possibility of obtaining microwire from a given metal-glass pair. On the other hand, the result of this interaction directly influences microwire properties. There always exists a submicron transition layer between the core and the glass shell.

1.6.2 Tensile strength of microwire

The following chapters will use two systems of physical units – SI and Gaussian-cgs. SI is more convenient for presentation of experimental data, while Gaussian-cgs is widely used in the published theory. Tensile strength of microwire is measured by load F (N, SI units, or dyn, Gaussian-cgs units) at its breaking point. However, a comparison of strength of microwires of different brands is done by combining the tensile stresses in the insulation and in the core. Usually tensile stresses ($N \times m^{-2}$, SI, or $dyn \times cm^{-2}$, Gaussian-cgs) of the metal core σ_{core} and the glass shell σ_{shell} are calculated by the well-known formula of the theory of elasticity:

$$\begin{cases} \sigma_{core} = \dfrac{F \times E_{metal}}{E_{metal} S_{metal} + E_{glass} S_{glass}} \\ \sigma_{shell} = \dfrac{F \times E_{glass}}{E_{metal} S_{metal} + E_{glass} S_{glass}} \end{cases} \qquad (1.1)$$

where E_{metal} and E_{glass} are Young's moduli ($N \times m^{-2}$, SI, or $dyn \times cm^{-2}$, Gaussian-cgs) of the metal core and glass shell respectively, S_{metal} and S_{glass} are their cross-sections (m^2, SI, or cm^2, Gaussian-cgs).

For the core of a microwire, a linear relationship between force and extension (Hooke's law) is retained until the yield point, while the relative elongation is less than 1.5-1.8%. The fracture is preceded by a plastic deformation in the metal core of about 30% ("plastic flow"). This deformation results in non-uniform distribution of strains between core and insulation whereby along with the increase of external load, tensile stresses increase only in the glass insulation. Therefore, at a certain ratio of the transverse dimensions of core and the insulation, the glass insulation will be destroyed by the slightest increase of the tensile force. This will automatically lead to failure of the core. In this case, there are grounds for believing that Eq. (1.1) will give an acceptable approximation.

1.6.3 Influence of segment length on strength of microwire

Particular interest arises in connection with study of the dependence of strength on the diameter for microwire of one reel. Apart from the effect of increase of strength connected with a decrease in diameter (which echoes earlier work by Griffiths [1.9]), when decreasing the test segment length an increase in strength is detected in the microwire. A noticeable increase in strength is observed at lengths less than 60 mm. In the segment of microwire of >60mm lengths, with a probability very close to 1, it is possible to encounter any defect, including particularly hazardous surface and significant defects, such as micro-cracks, isthmuses in the core, etc. Cracks in the glass shell appear gradually, which is related to development of defects, in which stresses exceeding the tensile strength of glass are concentrated. At the points of faults the insulation has a rough appearance; leading to local damage then its detachment from the core.

1.6.4 Influence of humidity and temperature

During investigations of the influence of humidity on the strength of the microwire [1.10] it was determined that short time exposure of copper microwire samples of diameter of 10-70 microns to water does not reduce their strength. There was also no noticeable decrease in the strength of microwire with copper, silver or nichrome core after their exposure to 500 hours of air with a relative humidity of 95-98% at a temperature of 40 °C. Microwires used as sensor inclusions will be embedded into different media so knowledge of the influence of media, on the mechanical properties of microwires becomes of crucial importance for such applications. Unfortunately, these influences have not yet been investigated much.

The process of microwire casting can be considered as a kind of hot hydrostatic extrusion [1.11, 1.12] where the billet (metal core in our case) is completely surrounded by a pressurised liquid (glass shell), except where the billet contacts the die (exit of glass capillary which is similar to a circular die). This process can be done hot, warm, or cold, however the temperature is limited by the stability of the fluid used. Hot extrusion is a hot working process, which means it is done above the material's re-crystallisation temperature to keep the material from work hardening and to make it easier to flow the material through the die. The process must be carried out in a sealed cylinder to contain the hydrostatic medium. The microwire casting process enables both the hot and hydrostatic conditions, where the viscous glass shell plays the role of gyrostatic liquid and cylindrical container.

It is well-known that extrusion may strengthen the final item for some alloys. Most probably, this effect takes place in the microwire casting. Prolonged exposure to elevated temperature reduces the strength of microwire, while short-term exposure does not affect its strength. At 500 °C microwire completely loses its strength. For example, the strength of manganin microwire is reduced by an average of 25% after six-hour exposure at 300 °C. Loss of strength of microwire with a core from resistant alloys after prolonged heat treatment should be attributed to the loss of the effect of extrusion.

1.6.5 Hardening/strengthening of microwire

Under microwire casting conditions, when the rate of cooling is about 10^6 °C/second, the presence of large amounts of dopant components (chromium, manganese, silicon) may lead to formation of a recrystallised structure [1.13] and anisotropic stresses in the super-saturated solid solutions. Recrystallisation is usually accompanied by a reduction in the strength and hardness of a material and a simultaneous increase in the ductility.

With the rise in temperature from 300-400 °C hardening of microwire is observed, which increases with the thickness of the insulation. This hardening is linked with the decrease of adsorption of moisture during the heating of glass, along with the hardening of glass insulation. On further heating, the strength of microwire significantly reduces. The nature of breakage at temperatures up to 450-500 °C is brittle fracture. Above 500 °C, the breakages acquire a plastic character. Along with the rise in temperature the strength of the aged microwire decreases faster than usual.

Temperature treatments with/without magnetic field are also used for modification of magnetic properties of microwires. Since such treatments may significantly change mechanical properties, they must be re-examined on each occasion.

While treating a copper microwire in a glass shell with hydrofluoric acid, hardening effect of microwire manifests itself, indicating presence of micro-defects on its surface, the number of which grow with the increase in diameter. Other possibilities of hardening of microwires open during the use of the ion exchange and mortar ceramics methods. In the ion exchange method, during treatment of microwire in special solutions, for example in eutectic melts of chlorides and sulphates, sodium ion from glass shell is replaced with lithium ions from the melt in equimolar amounts. The hardening takes place due to

compressive stresses formed in the surface layer, while in the inner layers tensile stress occurs. The strengthening effect in this case amounts to 60-70%.

In the ceramic mortar method which allows to increase the strength of the microwire by 2-3 times, thin silicate film whose thickness varies from 100-2000 nm is applied to the glass insulation. Application of this film not only reduces the surface micro-defects in the glass insulation, but also promotes the formation of compressive stresses in the surface layer, which results in strengthening effect.

Surface hardening treatment techniques have not yet been used for magnetic microwires. However, since they alter the distribution of residual stress in the microwires, their influence on the magnetic properties can be significant (via magneto-striction effect). In principle, such surface treatments can be highly effective in obtaining new magneto-anisotropic properties. This question needs further research, but is beyond the scope of this dissertation.

1.6.6 Toughness of microwire while bending

The Critical Bend Radius (CBR) is understood as the smallest radius, on to which microwire can be wound without disruption of its integrity. An increase of the outer diameter of microwire causes a decrease in its flexibility, i.e. stiffening due to an increase of the critical diameter. However, dependence of the CBR on the transverse dimensions of microwire is not as simple as for glass fibre. The CBR represents itself as a function of both the outer diameter of microwire and the diameter of the solid metal filament core. For technological purposes it is convenient to describe flexibility of microwire using the ratio $2r_{cr} / D$, where r_{cr} is the critical radius and D is the outer diameter of insulation. Studies on glass fibres established that for small diameters, this ratio remains constant and lies in the range 19-22.

Further, depending on the relation between the internal and external diameters of microwire a situation can arise where the stresses in the metal core will be greater than in the glass shell. However, even when the CBR is achieved, the metal core is not destroyed. Bending microwire devoid of glass shell did not disintegrate the sample even at CBR, apparently, due to plastic deformations in the core. The glass shell itself undergoes brittle fracture, as evidenced by its rapid destruction at the attainment of CBR. The external environment may have a noticeable effect on the critical radius in pure bend. For example, exposure of microwire to water and/or transformer oil for 24 hours leads to critical bend radius increases of 10-15%.

This project does not study sensor properties that may be attributed to bending. All microwires are assumed to be straight, at least during measurements. However, during the processes of embedding of microwires into a composite matrix they may acquire some curvature that may influence magnetic properties through the stress-induced anisotropy. Tolerance to such effects must be additionally investigated when developing a particular sensor application.

1.6.7 Coefficient of thermal expansion of microwire

Heating of microwire is accompanied with the change of its length. The dependence of the length of the microwire on its temperature is normally taken to be linear and is written as:

$$l_2^{mw} = l_1^{mw}(1+\alpha_{mw}\Delta t) \tag{1.2}$$

where $\Delta t = t_2 - t_1$, t_1 and t_2 are the initial and final temperatures respectively, l_1^{mw} and l_2^{mw} are the initial and final lengths of the microwire (*mw*) segment respectively, and α_{mw} is the coefficient of linear thermal expansion of the microwire in a given temperature range $[t_1, t_2]$. Note that in Eq. (1.2), l_2^{mw} is the system displacement for the whole two-component composite structure.

Due to the different linear Coefficients of Thermal Expansion (CTE) of glass and metal (α_{glass} and α_{core}), heating of microwire gives rise to additional stresses in the structure (residual stresses after casting already present there), which by Hooke's law, for the core and the shell, respectively, are written as:

$$\frac{F}{S_{core}} = E_{core} \times \frac{l_2^{core} - l_2^{mw}}{l_1^{core}} = E_{core} \times \frac{l_1^{core}(1+\alpha_{core}\Delta t) - l_1^{mw}(1+\alpha_{mw}\Delta t)}{l_1^{core}} \tag{1.3}$$

$$\frac{F}{S_{glass}} = E_{glass} \times \frac{l_2^{mw} - l_2^{glass}}{l_1^{glass}} = E_{glass} \times \frac{l_1^{mw}(1+\alpha_{mw}\Delta t) - l_1^{glass}(1+\alpha_{glass}\Delta t)}{l_1^{glass}} \tag{1.4}$$

where F is the force of interaction between the core and glass capillary at t_2. In Eqs. (1.3)-(1.4), l_2^{core} and l_2^{glass} are the displacements if the core and glass shell are free (not in contact). The differences between these displacements and l_2^{mw} introduce a tension in one material and a compression in the other.

Theoretically, we may have $l_2^{core} < l_2^{mw} < l_2^{glass}$ or $l_2^{glass} < l_2^{mw} < l_2^{core}$, and F may be positive or negative. Balancing the forces in Eqs. (1.3) and (1.4), we obtain:

$$S_{core}E_{core} \times \frac{l_1^{core}(1+\alpha_{core}\Delta t) - l_1^{mw}(1+\alpha_{mw}\Delta t)}{l_1^{core}} = \\ = S_{glass}E_{glass} \times \frac{l_1^{mw}(1+\alpha_{mw}\Delta t) - l_1^{glass}(1+\alpha_{glass}\Delta t)}{l_1^{glass}} \tag{1.5}$$

Assuming $l_1^{core} = l_1^{glass} = l_1^{mw}$, we obtain:

$$S_{core}E_{core} \times \left[(1+\alpha_{core}\Delta t) - (1+\alpha_{mw}\Delta t)\right] = \\ = S_{glass}E_{glass} \times [(1+\alpha_{mw}\Delta t) - (1+\alpha_{glass}\Delta t)] \tag{1.6}$$

Solving Eq. (1.6) with respect to α_{mw}, we obtain:

$$\alpha_{mw} = \frac{S_{core}E_{core}\alpha_{core} + S_{glass}E_{glass}\alpha_{glass}}{S_{core}E_{core} + S_{glass}E_{glass}} \tag{1.7}$$

Putting $S_{core} = \pi d^2$ and $S_{glass} = \pi(D^2 - d^2)$, into Eq. (1.7), we obtain:

$$\alpha_{mw} = \frac{E_{core}\alpha_{core} + \left(\left(\frac{D}{d}\right)^2 - 1\right)E_{glass}\alpha_{glass}}{E_{core} + \left(\left(\frac{D}{d}\right)^2 - 1\right)E_{glass}} \tag{1.8}$$

Thus when materials of core and insulation are not changed, CTE of microwire is determined only by the ratio D/d. When using Eq. (1.8), differences between the experimental and calculated values of the CTE of microwire usually do not exceed 5%. The derivation of the above equations in the original source [1.1] has several misprints, and formula presented here has been rederived and confirmed by dimensional analysis.

Putting Eq. (1.8) into Eq. (1.3) and Eq. (1.4), the additional stresses caused by the temperature change can be found:

$$\Delta\sigma_{core} = \frac{E_{core}E_{glass}(\alpha_{core} - \alpha_{glass})\left(\left(\frac{D}{d}\right)^2 - 1\right)\Delta t}{E_{core} + \left(\left(\frac{D}{d}\right)^2 - 1\right)E_{glass}} \quad (1.9)$$

$$\Delta\sigma_{glass} = \frac{E_{glass}E_{core}(\alpha_{core} - \alpha_{glass})\Delta t}{E_{core} + \left(\left(\frac{D}{d}\right)^2 - 1\right)E_{glass}} \quad (1.10)$$

Since $\alpha_{glass} < \alpha_{core}$, for $\Delta t > 0$ the stress $\Delta\sigma_{core} > 0$ in Eq. (1.9) will be compressive. On the other hand, due to the same condition $\alpha_{glass} < \alpha_{core}$, the fast cooling during the casting process (see Figs. 1.5 and 1.6) will result in a residual compressive stress in the core (negative stress). The latter defines the magnetic anisotropy due to the magnetostriction effect. With increase of temperature, $\Delta\sigma_{core}$ will gradually compensate the residual tension thus resulting in a reduced anisotropy. Eq. (1.9) suggests that this compensation will be stronger for a thicker glass shell. This conclusion is confirmed in other works [1.14].

1.6.8 Resistive properties of microwires

Specific and linear electrical resistances of microwires are important parameters while creating various elements and devices on its basis. The resistivity ρ of microwire core is mainly determined by the specific resistance of metals and alloys, of which microwire is currently commercially produced. Table 1.1 shows comparative values ρ of some initial pure metals and their microwires at 20 °C. From the given data, ρ of microwire core differs from ρ of the initial metal, increasing in some cases by more than 50%.

Core materials	ρ of raw material, $\frac{\Omega \times mm^2}{m}$	ρ of microwire, $\frac{\Omega \times mm^2}{m}$	Change in ρ, %
Copper	0.017	0.022	30
Silver	0.016	0.020	25
Nickel	0.073	0.090	23
Gold	0.024	0.035	46
Cobalt	0.064	0.080	25
Palladium	0.108	0.134	24
Platinum	0.107	0.127	19
Iron	0.098	0.157	60
Lead	0.206	0.270	31
Tin	0.115	0.190	65

Table 1.1. Raw material and microwire resistivities for some pure metals [1.1].

The observed increase of resistivity is connected with a change in the chemical composition of the core during the casting process, caused by oxidation of metal, and also by diffusion of elements from the glass into the metal. Resistivity of microwire made of resistance alloys is governed by the composition of the alloys from which its casting has been carried out.

The Temperature Coefficient of Resistance (TCR) (Kelvin^{-1}) in a given temperature range is change in resistance caused by 1 °C temperature change from t_1 to t_2, and is defined by the formula:

$$\mathrm{TCR}(t_1, t_2) = \frac{R_2 - R_1}{R_1(t_2 - t_1)} \qquad (1.11)$$

where R_1 is the resistance at t_1, R_2 is the resistance at t_2.

TCR of microwires from metals, and their resistivity ρ, change during the casting process for identical reasons. TCRs for microwires made of pure metals are shown in Table 1.2.

Core materials	TCR of metal, 1/degree $\times 10^6$	TCR of microwire, 1/degree $\times 10^6$	Core materials	TCR of metal, 1/degree $\times 10^6$	TCR of microwire, 1/degree $\times 10^6$
Copper	4200	3000	**Palladium**	3700	2800
Silver	4200	3000	**Platinum**	3900	3300
Nickel	6700	5000	**Iron**	6600	4000
Gold	3500	3200	**Lead**	4200	3500
Cobalt	6600	4500	**Tin**	4400	3700

Table 1.2. The temperature coefficient of resistance for microwires made of pure metals [1.1].

In works reviewed in Ref. [1.1] in which microwire properties are analysed, the possibility of their use over a wide range of temperatures is emphasised. The stability at elevated temperatures is influenced by the microwire structure. Preliminary heat treatments influence the stability of the electrical resistance of manganin microwire. Microwires heat treated at 200-250 °C are most stable. Stability of microwire is also influenced by the physical and chemical properties of the glass from which the shell is made. Longevity of microwire is strongly dependent on temperature and on the permissible change in resistance.

Tensoresistive effect is the change in the electrical resistance of the conductor during its stretch deformation. For quantitative characterisation of this property of a microwire, the gauge factor is introduced as determined from the ratio:

$$S = \frac{\frac{\Delta R}{R}}{\frac{\Delta l}{l}} \qquad (1.12)$$

where R is the electrical resistance, l is the length, and ΔR and Δl are their respective changes.

The gauge factor S of a microwire depends on the conditions of its production and the properties of the initial alloy. For a number of metals and alloys used in microwire core, deviations from the elastic behaviour under deformation take place in the microwire. Tensosensitivity of such microwires changes

under repeated loading. Due to the instability of electrical resistivity of microwire its tensosensitivity changes with time. Heat treatment of microwire is recommended to reduce this instability.

This research project will study the high frequency impedance (tenso-, thermo-, and magnetic field-) effects in a microwire made of Co-based magnetic alloys. Specific microwire properties and alloy compositions used in experiments are described in Chapters II and IV. For sufficiently high frequencies (MHz range), the so-called skin effect takes place with the current density decreasing towards the central axis. Thus, the current experiences a larger effective resistance due to the reduced cross section. The linear relation between the current and voltage amplitudes generally becomes a complex number called the impedance, where the real part is the resistance and the imaginary part is the contribution of the effective inductance. The impedance in magnetic microwires may strongly depend on external stimuli such as magnetic field, tensile stress, and temperature. The dependence on the external stress can be called the tensoimpedance effect which will always prevail over the tensoresistive effect, and hence the latter can normally be neglected for sensor applications described in this work.

Chapter II

Embedded ferromagnetic microwires for monitoring tensile stress in polymeric materials

"*Considerable efforts have been made to develop non-destructive testing methods for polymer composite materials. This chapter introduces a new method of monitoring internal stresses. The method can be classified as an embedded sensing technique, where the sensing element is a glass-coated ferromagnetic microwire with a specific magnetic anisotropy. The microwire impedance acts as the controlled parameter which is monitored for a weak alternating current (AC) in the MHz range. The microwire impedance becomes stress sensitive in the presence of a weak constant axial bias magnetic field. This external parameter allows the impedance stress sensitivity to be easily tuned. In addition, a local bias field may also allow the reconstruction of stress profile when it is scanned along the microwire. The experimental results are analysed using simple magnetostatic and impedance models.*

This chapter has largely been published in Composites Part A: Applied Science and Manufacturing, V. 61, pp. 216–223, (2014)."

2.1. Introduction

Ferromagnetic microwires coated with glass can be used in several niche applications due to their specific magneto-anisotropic properties [2.1-2.3]. There are two types of microwires. The first type, known as bistable microwires, is characterised by an almost rectangular magnetic hysteresis loop (the relationship between the induced magnetic flux density and a magnetising force) measured along the microwire axis. These microwires, demonstrating natural ferromagnetic resonance, have found applications in microwave absorbing materials [2.4-2.6]. The second type of microwires is characterised by a narrow inclined hysteresis loop. The most remarkable property observed in these microwires is the so-called Magneto-Impedance (MI) effect: a large change in the microwire high frequency impedance under the influence of a longitudinal magnetic field [2.7, 2.8]. The Mohri et al review [2.9] describes implemented magnetic sensors based on MI.

In the embedded sensing techniques, some special particles or fibres are used which act as mediators between internal parameters of the medium and a readout device. Depending on the physical principle of this intermediary function, different physical quantities can be utilised as the measurement parameters which include: current, voltage, resistance or impedance, electric or magnetic fields, permeability or permittivity, reflected or transmitted electromagnetic waves (amplitude and phase). The

method of monitoring the internal tensile stresses, developed in this chapter, consists in embedding a MI glass-coated microwire into a polymer matrix and measuring its impedance using a weak high frequency current in the MHz range. As opposed to the usual MI, the tensile stress is used as the control parameter instead of the magnetic field. Before proceeding further, it would be useful to conduct a comparative analysis of several embedded sensing methods which are similar to the method presented either by the geometry of inclusions or some physical principles.

The undisputed leader in non-destructive testing of composites is the method using embedded optical fibres [2.10, 2.11]. The silica or polymer optical fibre may play the role of a sensor by itself or could transmit signals between the tested area, where the light interacts with a substance, and a readout device. Along with the extraordinary sensitivity, the optical method can also measure a wide range of parameters such as strain, temperature, pressure, humidity, and vibration. In addition, it is immune to electromagnetic interference. The experience gained by the integration of optical fibres into a polymer matrix is useful here because their diameters ($7-50\,\mu m$) are close to those of microwires. Since microwires are coated with glass, the bonding of microwire skin and fibre core interfaces should be comparable assuming similar surface treatments. Despite modest diagnostic capabilities as compared with optical fibres, the microwire-based sensor proposed in this work can be made tuneable and the instrumentation has much lower cost.

In impedance-based spectroscopy [2.12-2.16], the effective impedance of the mixture of conductive reinforcing fibres (steel or carbon) and a weakly conductive matrix is measured in a specific frequency range (normally MHz) between a pair of patch contacts attached to the sample surface. Since the volume fraction of fibres ($<3\%$) is usually below the percolation transition, the presence of a weakly conductive matrices is absolutely necessary to ensure the effective conductivity. An external stress does not change the electrical properties of non-magnetic conductive fibres. The piezoimpedance effect is caused by the fibre-matrix interface which has a capacitive nature due to the oxidation or polarization layers forming on the surfaces of steel and carbon fibres, respectively. Thereby, this method can scarcely be used in polymer matrixes as the conductivity is too small. On the contrary, the stress sensitivity of ferromagnetic microwires is caused only by their internal magnetic properties, and hence they can be used in any dielectric matrix allowing their embedding.

In magnetostrictive tagging, Terfenol-D magnetic micro-particles ($<300\,\mu m$ in size) are added to the composite matrix to produce the effective magnetic properties [2.17, 2.18]. Since Terfenol-D particles are almost nine times denser than the matrix resin, they tend to settle during cure. To prevent this process,

the sample is placed between the poles of a permanent magnet creating a homogeneous magnetic field perpendicular to the sample plane. Samples manufactured using this technique have aligned particle clusters and demonstrate an enhanced magnetostrictive response when they are loaded. Stress transferred through the matrix to the particles causes a change in the direction of equilibrium magnetisation due to the inverse magnetostrictive effect. Stress monitoring measures the longitudinal or transverse component of the magnetic field near the sample surface using a magnetometer. This inverse magnetostriction effect may also be used. However, the measured quantity is a high frequency MI of microwires that depends on the direction of magnetisation. The use of ready-made microwires eliminates the necessity of forming the magnetic properties during cure. Moreover, the MI microwires have a very narrow hysteresis loop that eliminates the problem of calibration when measuring a cyclic load.

Investigation of the matrix parameters which may affect the magneto-impedance of embedded microwires is of crucial importance for the development of not only the contact stress sensors, but also microwave smart materials. In the GHz range, microwires homogeneously distributed inside the matrix can be interrogated remotely using microwave beams. The short microwire inclusions will scatter the incident microwave in a similar manner to the miniature dipoles [2.19], while the long microwire strings will respond as the cold plasma of free electrons [2.20]. A local magnetic field, stress, and temperature will change the impedance of microwires and, as a consequence, the transmitted and reflected microwaves. The volume fraction of microwires required to introduce a tuneable microwave functionality is very small (much less than 1%) and thus reduces the impact of sensor inclusions on the mechanical properties of matrix. Composites based on ferromagnetic micro- and nano-microwires are being studied experimentally and theoretically by several research groups (see e.g. [2.21-2.26]). Despite the growing interest in tuneable microwave composites, only one work [2.27] seems to have published the effect of tensile stress on the free-space microwave properties of the wire-filled composites. Difficulty in carrying out such experiments is caused by the need to integrate a loading frame with microwave antenna measurements.

In this chapter, we return to contact impedance measurements with a ferromagnetic microwire embedded into a commercial epoxy resin matrix. The experiments are designed not only to demonstrate the physical effects, but also to address a number of practical issues that pertain to the embedded sensors. In particular, the relationship between the magnetic and mechanical response of microwires to the matrix elastic properties will be demonstrated.

2.2. Magnetostatic and impedance models for glass-coated microwires

In this section the magnetostatic and impedance models used later in Section 2.3 to analyse experimental results are introduced. The Gaussian-cgs system of units will be used within the formulation of theoretical models, while SI units are more convenient for the interpretation of experimental data. Unless stated otherwise, the physical dimensions specified in the brackets would refer to SI units.

As described previously in Section 1.3, glass-coated microwires are produced using the Taylor-Ulitovski casting method. As a result of quenching, an amorphous or polycrystalline metal core is obtained in the glass envelope. The initial process of quenching and the difference in thermal expansion coefficients of glass and metal create a tensorial residual stress, $\hat{\boldsymbol{\sigma}}$, inside the metal core which is responsible for the magnetic anisotropy [2.28-2.30]. The components of $\hat{\boldsymbol{\sigma}}$ can be further modified by an annealing treatment. In as-cast glass-coated microwires, the axial tensile stress σ_a produced by the glass shell is predominant over other residual stresses. For glass-coated microwires made of a Co-based alloy, which have a small negative magnetostriction, the predominant residual tensile stress σ_a will result in a circular magnetisation $\mathbf{M}_0$ in the near-surface layer of the metal core. In turn, this circular magnetised shell is divided into cylindrical domains with opposite magnetisation directions.

The direction of $\mathbf{M}_0$ can be controlled by the combined action of an external axial magnetic field H_{ex} and an external axial stress σ_{ex}. The total residual stress on the surface of the microwire metal core also needs to be taken into account. It can be decomposed into the axial tension σ_1 ($\sigma_1 = \sigma_a$) and the torsion (pure shear) which is a combination of tension and compression with equal intensity σ_2 perpendicular to each other and at $45°$ to the microwire axis [2.31]. In the frame of the Stoner-Wohlfarth model [2.32], the total magnetostatic energy per unit volume (erg/cm^3, Gaussian-cgs) can be written in the following form [2.33]:

$$U_t(\theta) = -M_0\left(\frac{1}{2}\sin(\lambda)H_K\cos^2(\alpha+\theta) + H_{ex}\cos(\theta) + H_b\sin(\theta)\right) \tag{2.1}$$

$$K = \frac{3}{2}|\lambda|\tilde{\sigma} \tag{2.2}$$

$$H_K = \frac{2K}{M_0} = \frac{3|\lambda|\tilde{\sigma}}{M_0} \tag{2.3}$$

$$\alpha = \frac{1}{2}\tan^{-1}\left(\frac{2\sigma_2}{\sigma_1+\sigma_{ex}}\right) \tag{2.4}$$

$$\tilde{\sigma} = \sqrt{(\sigma_1 + \sigma_{ex})^2 + 4\sigma_2^2} \qquad (2.5)$$

where α is the angle of magnetic anisotropy measured from the circular direction, $\sin(\lambda)$ is the sine of the magnetostriction constant λ, K is the anisotropy constant (erg/cm^3, Gaussian-cgs), H_K is the anisotropy field (Oe, Gaussian-cgs), $H_b = 2I_b / ca$ (Oe, Gaussian-cgs) is the circular DC magnetic field on the surface of metal core induced by a DC bias current I_b in the microwire, θ is the angle between $\mathbf{M}_0$ (emu/cm^3, Gaussian-cgs) and the wire axis, $M_0 = |\mathbf{M}_0|$ is the modulus of $\mathbf{M}_0$, the parameters $\sigma_{1,2}$ (dyn/cm^2, Gaussian-cgs) are assumed to be positive, the external axial stress σ_{ex} (dyn/cm^2, Gaussian-cgs) may be positive (tension) or negative (compression), a (cm) is microwire metal core radius and $c \approx 3.0 \times 10^{10}$ cm/s is the speed of light. The current I_b may improve the experimental MI characteristics by eliminating the circular domain structure [2.34].

The equilibrium direction of $\mathbf{M}_0(\theta_{eq})$ is found by minimising the magnetostatic energy: $\partial U_t(\theta)/\partial\theta = 0 \rightarrow \theta = \theta_{eq}$. For $\lambda < 0$, in accordance with the principle of minimum energy, the axial tension will rotate $\mathbf{M}_0$ towards the circular direction ($\theta \rightarrow 90°$), while the crossed tension and compression will rotate $\mathbf{M}_0$ towards a $45°$ axis. Thus, there are two competing rotations. As a result, in the absence of H_{ex} the equilibrium angle will be $45° \leq |\theta| \leq 90°$ with respect to the $0°$ axial microwire direction.

2.3. Impedance model for ferromagnetic microwires

The voltage V (V, SI) measured across a microwire with a length l (m, SI) carrying an alternating current $i = i_0 \exp(-j\omega t)$ (A) can be expressed through the ζ_{zz} component of the impedance tensor $\hat{\zeta}$ (Ω, SI) relating the axial electric field e_z (V/m, SI) and the circular magnetic field h_φ (A/m, SI) induced by the current [2.34]:

$$V = e_z l = \zeta_{zz} h_\varphi l \qquad (2.6)$$

Here, $h_\varphi = i/2\pi a$ is the circular magnetic field on the surface of the microwire metal core having the radius a (m, SI). Eq. (2.6) can be rewritten in the form of Ohm's law: $V = iZ$, where $Z = \zeta_{zz} l/2\pi a$ is the microwire impedance (complex resistance). The surface impedances in the two systems of units can be easily recalculated into each other: $\zeta^{\text{cgs}} = (10^9/4\pi c)\times\zeta^{\text{SI}} \approx 0.002654\times\zeta^{\text{SI}}$ (dimensionless in Gaussian-cgs), where ζ is a component of $\hat{\xi}$. The surface longitudinal impedance ζ_{zz} can be recovered from the measured microwire impedance Z (Ω, SI): $\zeta_{zz}^{\text{SI}} = 2\pi aZ/l$ or $\zeta_{zz}^{\text{cgs}} = 10^9 aZ/(2cl)$. During the measurements, the interpretation of Z or ζ_{zz} as a lumped parameter is true only if the length l of microwire sample is much smaller than the effective wavelength.

In Ref. [2.34], the component ζ_{zz} was calculated at the conditions of weak and strong current skin-effects (the time dependence $\sim\exp(-j\omega t)$):

$$\zeta_{zz}^{weak}(\theta) \approx \frac{kc\rho}{4\pi}\frac{J_0(ka)}{J_1(ka)} \tag{2.7}$$

$$\zeta_{zz}^{strong}(\theta) \approx \frac{(1-j)}{2}\sqrt{\frac{\omega\rho}{2\pi}}\left(\sqrt{\mu_{eff}(\theta,\omega)}\cos^2(\theta)+\sin^2(\theta)\right) \tag{2.8}$$

where J_0 and J_1 are Bessel functions of the first kind, ρ is the specific resistivity (s, Gaussian-cgs), a is the microwire radius (cm, Gaussian-cgs), $\mu_{eff} = 1+4\pi\chi$ is the effective permeability, $\gamma \approx 1.8\cdot 10^7$ (rad×s^{-1}×Oe^{-1}, Gaussian-cgs) is the gyromagnetic ratio, and $\tau << 1$ is a small spin-relaxation parameter. Other dynamic parameters are:

$$k^2 = \frac{4\pi j\omega(1+4\pi\cos^2(\theta)\chi)}{\rho c^2},$$

$$\chi = \frac{\omega_M(\omega_2 - j\tau\omega)+4\pi\omega_M^2}{(\omega_1 - j\tau\omega)(\omega_2+4\pi\omega_M - j\tau\omega)-\omega^2},$$

$$\omega_1 = \gamma\left(H_{ex}\cos\theta + H_b\sin\theta - H_K\cos 2(\alpha+\theta)\right),$$

$$\omega_2 = \gamma(H_{ex}\cos\theta + H_b\sin\theta + H_K\sin^2(\alpha+\theta)),$$

$$\omega_M = \gamma M_0.$$

Note that in Ref. [2.34] α was measured from the microwire axis, while in the above equations it is measured from the radial direction. A criterion should be proposed to choose between Eqs. (2.7) and (2.8) as these asymptotic formulae do not transform into each other when changing the frequency. The high frequency approximation (2.8) has to be used when $\delta_m / a << 1$, where $\delta_m = c\sqrt{\rho/(2\pi\omega|\mu_{eff}|)}$ is the so-called magnetic skin-depth.

2.4. Microwire stress-impedance

It will be shown that a longitudinal DC bias field is required to provide the tensile stress sensitivity of microwire impedance. The stress transformation properties of magneto-impedance characteristics measured in a microstrip cell in the MHz range are in a good agreement with the model formulated in Section 2.2. However, the stress impedance measurements conducted for a microwire embedded into a composite matrix reveal a significant discrepancy with the model and the stress impedance measurements in the RF cell. Some possible reasons of the discrepancy are discussed below.

As diameters of typical glass-coated microwires are in the range of $5-70$ microns, they can be easily embedded between individual layers of a composite structure. For the stress-monitoring, MFTI Ltd Co-based microwires with the composition $Co_{68}Fe_4Cr_3Si_{11}B_{14}$ (wt%) were used. The diameter of metal core and the thickness of glass shell were $\sim 25.3\,\mu m$ and $\sim 4\,\mu m$, respectively. The magnetisation curves $M_{axial}(H_{ex}) = M_0 \cos(\theta(H_{ex}))$ (Fig. 2.1) were measured for a 5 cm long microwire by means of the inductive method. The loops observed at the saturation region were caused by non-ideal balancing of the electronic circuit. In the middle part of magnetisation curves, magnetic hysteresis may also contribute to the loop opening. During these measurements, the upper end of the microwire was fastened, while its lower free end was loaded with different weights of mass M (grams) to produce an external tensile force $F = Mg$, where $g \approx 9.8$ m/s^2 is the gravitational acceleration. This stress is redistributed between the metal core of the microwire and its glass shell which each have different Young's moduli (E_m, E_g) and cross-sections (S_m, S_g), where subscripts m and g indicate metal core and glass shell respectively. The stress σ_{ex} in Eqs. (2.3)-(2.5) transferred to the metal core can be calculated on the basis of the principle of consistent deformations used in statically indeterminate systems (see Eq. (1.1) in Section 1.6.2):

$$\sigma_{ex} = \frac{E_m F}{E_m S_m + E_g S_g} \tag{2.9}$$

To estimate this stress in a glass-coated amorphous CoFeCrSiB microwire, the typical Young's moduli would be $E_m \sim 130$ GPa and $E_g \sim 70$ GPa [2.35].

The presence of linear central parts in the narrow hysteresis loops in Fig. 2.1 is a characteristic feature of glass-coated ferromagnetic microwires with a circular magnetic anisotropy ($\alpha \approx 0$). For these microwires, the transition from the inclined central part to the saturation region occurs at $H_{ex} = \pm H_K$. The anisotropy angle $\alpha \approx 0$ in Eq. (2.4) is measured from the circular direction and is achieved for $\sigma_1 >> \sigma_2$ when the axial residual stress prevails over other residual stresses. Using Eqs. (2.3),(2.5) with $\sigma_1 >> \sigma_2$ and Eq. (2.9), the residual tensile stress σ_1 can be estimated as:

$$\sigma_1 \sim \frac{\sigma_{ex} H_K(0)}{H_K(\sigma_{ex}) - H_K(0)} \tag{2.10}$$

where $H_K(0)$ and $H_K(\sigma_{ex})$ are the experimental anisotropy fields taken from Fig. 2.1 at $\sigma_{ex} = 0$ and any $\sigma_{ex} \neq 0$, respectively. For an experimental value $F = 1.06$ N (see Fig. 2.1), Eq. (2.9) gives $\sigma_{ex}(1.06\ \text{N}) \approx 1.512$ GPa. Putting $H_K(0) \approx 2$ Oe and $H_K(1.512\ \text{GPa}) \approx 13$ Oe (both taken from Fig. 2.1) into Eq. (2.10), we obtain $\sigma_1 \sim 275$ MPa. The failure force $F_f = 1.42$ N produces the tensile stress $\sigma_{ex} \sim 2$ GPa in the metal core.

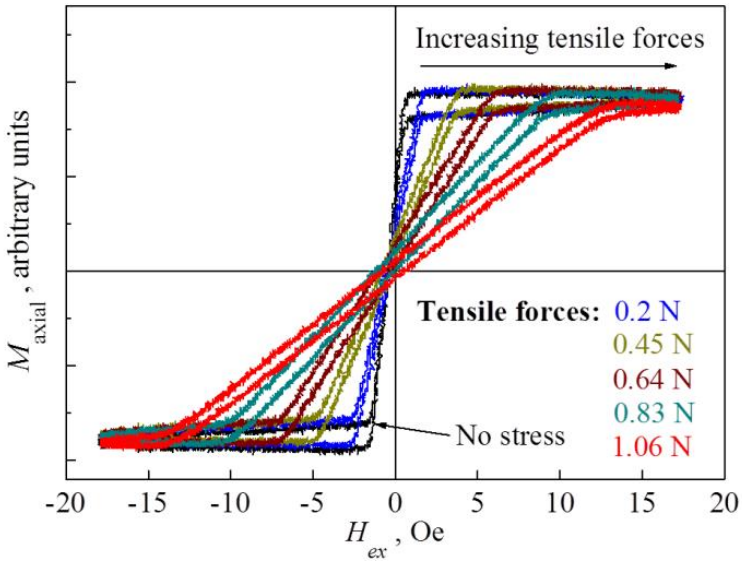

Fig. 2.1. The experimental magnetisation curves measured in the $Co_{68}Fe_4Cr_3Si_{11}B_{14}$ microwire at different tensile forces. The microwire has the total diameter $\sim 33.3\,\mu m$, the metal core diameter $\sim 25.3\,\mu m$, and the thickness of glass shell $\sim 4\,\mu m$.

The magnetostatic model in Eqs. (2.1)-(2.5) reproduces the experimental magnetisation curves and their transformations under the effect of external tensile stress. In Fig. 2.2, the theoretical curves $\cos(\theta(H_{ex})) = M_{axial}(H_{ex})/M_0$ were calculated for the following model parameters: $\sigma_1 = 275\times10^7$ dyn/cm^2 (from the estimated 275 MPa), $\sigma_2 = 5\times10^7$ dyn/cm^2 (any arbitrary value that provides a small loop opening), $\lambda = -10^{-7}$ (a typical value), $M_0 = 400$ emu/cm^3 (estimated from $M_0 = 3|\lambda|\sigma_1/H_K(0)$), and $H_b = 0$. The parameter σ_2 controls the width of hysteresis loop (very small in our microwire). On increasing the external stress, the anisotropy field $H_K(\sigma_{ex}) = 3|\lambda|\sqrt{(\sigma_1+\sigma_{ex})^2+4\sigma_2^2}/M_0$ as a function of σ_{ex} also increases, while the anisotropy angle α from Eq. (2.4) measured from the circular direction becomes smaller.

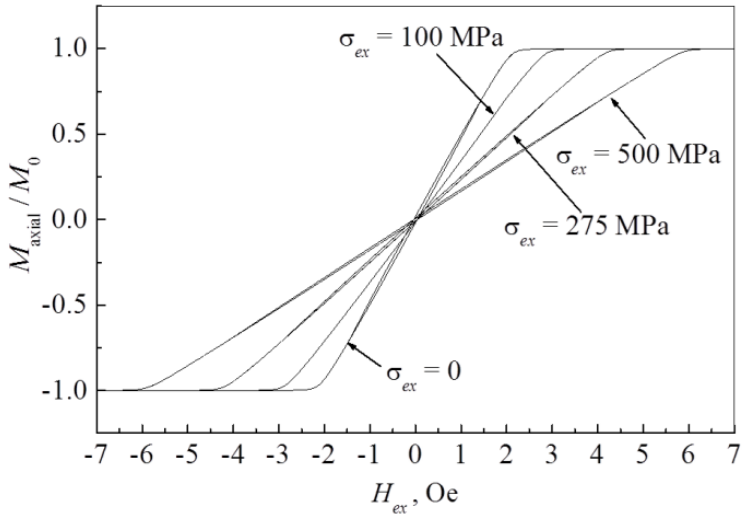

Fig. 2.2. The theoretical magnetisation curves with the external tensile stress as a parameter calculated for a microwire with an almost circumferential anisotropy using the magnetostatic model (2.1)-(2.5). The model parameters used for the calculations are: $\sigma_1 = 275\times10^7$ dyn/cm^2, $\sigma_2 = 5\times10^7$ dyn/cm^2, $\lambda = -10^{-7}$, and $M_0 = 400$ emu/cm^3. A small σ_2 was used to reproduce the narrow hysteresis loops observed in the experiment.

Since $Z \sim \zeta_{zz}$, further analysis will be conducted for ζ_{zz}. In Fig. 2.3, the field dependencies of $|\zeta_{zz}|$ with the tensile stress σ_{ex} as the variable parameter were calculated for a microwire with an almost circumferential anisotropy ($\alpha \approx 0$) using Eqs. (2.1)-(2.5) and (2.8). The excitation frequency was chosen to be 40 MHz. The magnetostatic parameters used for the calculations were the same as in Fig. 2.2. Other parameters used: $a = 12.65\times10^{-4}$ cm is the radius of microwire metal core and $\rho = 2.56\times10^{-16}$ (s, Gaussian-cgs) is its resistivity (estimated from experimental data), $\gamma = 1.8\cdot10^7$ (rad×s^{-1}×Oe^{-1}, Gaussian-cgs) is the gyromagnetic ratio, and $\tau = 0.1$ is a small relaxation parameter. As seen in Fig. 2.3, under the effect of tensile stress, the curve $|\zeta_{zz}(H_{ex})|$ becomes wider. The maxima of $|\zeta_{zz}(H_{ex})|$ are reached at $H_{ex} = \pm H_K$ (see Eq. (2.3)). In zero magnetic field, ζ_{zz} does not show any stress sensitivity because the magnetisation angle is already $90°$, and hence the direction of equilibrium magnetisation $\mathbf{M}_0$ will not be changed by an external tensile stress.

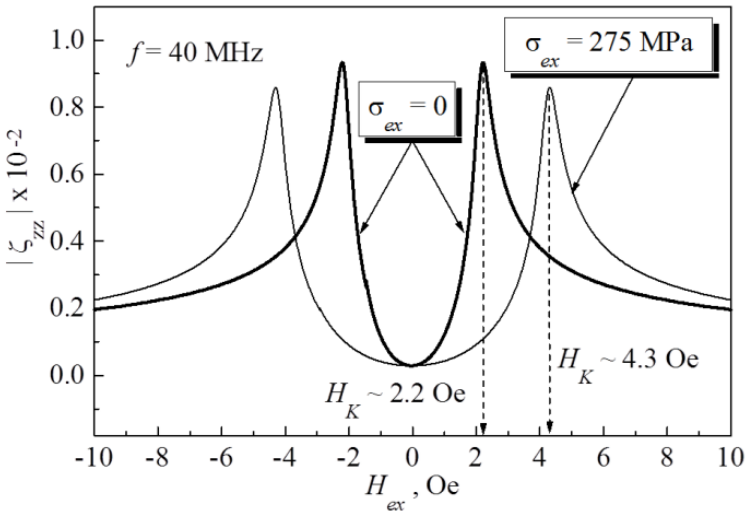

Fig. 2.3. The theoretical field dependencies of ζ_{zz} with σ_{ex} as a parameter calculated for a microwire with an almost circumferential anisotropy using Eq. (2.8) and the magnetostatic model (2.1)-(2.5). The excitation frequency is 40 MHz.

For $H_{ex} \neq 0$, the magnetisation will be deflected from its initial circular direction. In this case, ζ_{zz} becomes stress sensitive because the external tensile stress will rotate the magnetisation back to the circular direction. The largest stress sensitivity of ζ_{zz} is achieved at $H_{ex} = \pm H_K(0)$, where $H_K(0)$ is H_K at $\sigma_{ex} = 0$. For these bias fields, the saturation stress σ_s required to rotate the magnetisation back to nearly 90^0 is of the order of σ_1 (residual axial tensile stress). Using Eq. (2.3), σ_1 can be expressed through the anisotropy field. For the saturation strain $\varepsilon_s = \sigma_s / E_m \sim \sigma_1 / E_m$, we obtain ($\sigma_1 >> \sigma_2$):

$$\varepsilon_s \sim \frac{H_K(0) M_0}{3|\lambda| E_m} \qquad (2.11)$$

where E_m (dyn/cm^2, Gaussian-cgs) is the Young modulus of the metal core. The anisotropy fields of glass-coated microwires are typically in the range $1-20$ Oe.

The experimental field dependencies of $|Z(H_{ex})| \sim |\zeta_{zz}(H_{ex})|$ shown in Fig. 2.4 were measured for the same $Co_{68}Fe_4Cr_3Si_{11}B_{14}$ microwire as in Fig. 2.1. The measurement method is described below. A short piece of the microwire (~ 20 mm) is placed onto a PCB microstrip measurement cell (MMC) as shown in Fig. 2.4 (see Chapter III for design and fabrication processes of PCB MMCs). To enable the electrical contacts, the glass coating at the ends of microwire is mechanically removed and then the

microwire ends are attached to the microstrips using a conductive glue or paint, such as Electrolube SCP03B Silver Conductive Paint and CircuitWorks Conductive Silver Epoxy. The MMC has a single 3.5 mm connector between the ground plane and the microstrip.

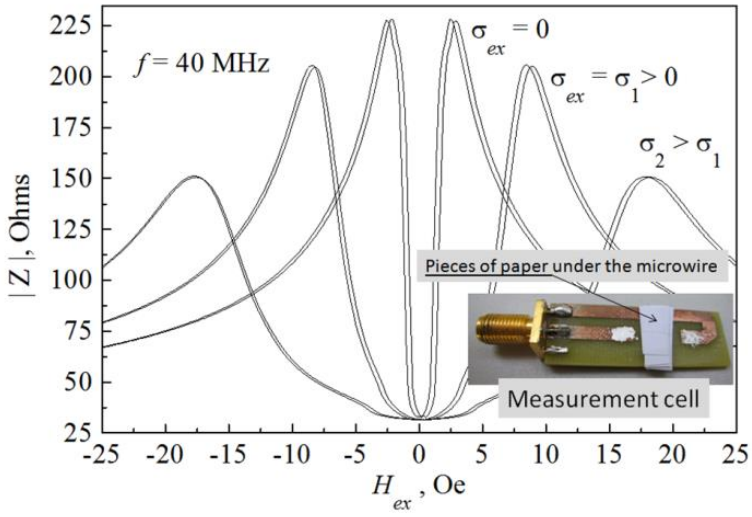

Fig. 2.4. The microwire impedance vs. the axial magnetic field measured in the same $Co_{68}Fe_4Cr_3Si_{11}B_{14}$ microwire as in Fig. 2.1 at different tensile stresses. The microstrip measurement cell is also shown. The excitation frequency was 40 MHz. The tensile stress was introduced by means of the pieces of paper placed under the microwire to slightly stretch it.

The 1-Port calibration procedure is performed to calibrate the coaxial cables connecting the measurement cell to the Analyser's port using the OPEN, SHORT and LOAD coaxial standards [4.3]. In a lower band of the MHz range, the microstrips will not introduce significant distortions in the microwire impedance response. The microwire impedance is calculated from the measured S_{11} parameter as $Z = 50\Omega \times (1+S_{11})/(1-S_{11})$. The S_{11} parameter (a complex reflection coefficient) is a component of the scattering matrix $\hat{\mathbf{S}}$ which is discussed in detail in Section 4.2. The microwire was fixed within the MMC strip gap using a conductive paint at positions 15 mm apart. Tensile stress was introduced by inserting up to 5 pieces of paper under the central 5 mm of the microwire to raise the middle of the microwire by ~ 0.1 mm per piece of paper. The geometrical parameters of each piece of paper (width ~5 mm and thickness ~0.1 mm) and the strip gap (15 mm) permit estimation of the maximum strain for 5 pieces as 3.33×10^{-3} as shown in Fig. 2.4. Whilst using such a method, the stress cannot be accurately controlled, but its effect on $|Z(H_{ex})|$ can be clearly demonstrated. The experimental field dependencies of $|Z(H_{ex})|$ shown in

Fig. 2.4 and their stress-transformational properties are in qualitative agreement with the theoretical ones in Fig. 2.3.

Fig. 2.3 and 2.4 demonstrate that the magnetostatic and impedance models (2.1)-(2.8) will work well at least for the chosen microwire. However, these models remain oversimplified. The kHz range and the lower band of MHz range are always problematic for the impedance model (2.7), (2.8) as they completely neglect the domain structure and the corresponding susceptibility caused by the high frequency oscillations of domain walls. Fig. 2.5 shows the typical behaviour of the field impedance measured in a Co-based microwire at a low MHz frequency.

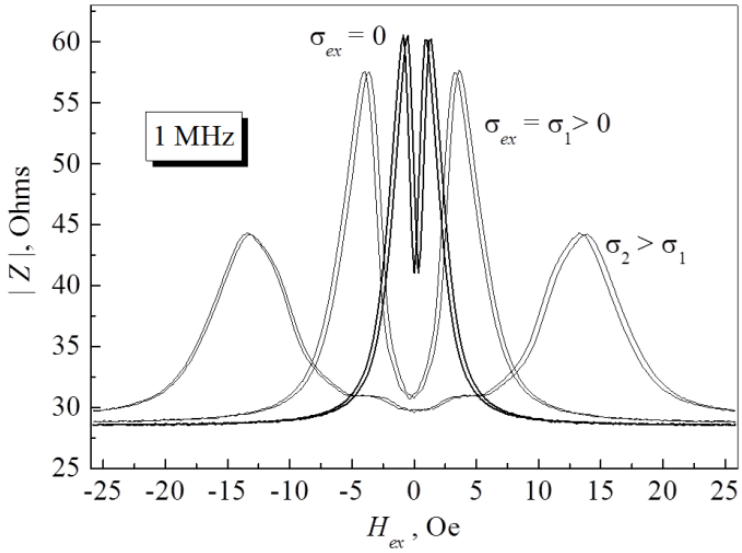

Fig. 2.5. The typical behaviour of the field impedance at lower MHz frequencies. The impedance was measured in the same microstrip cell as in Fig. 2.4.

Now, the minimum impedance in zero field is not global. Furthermore, as the frequency decreases, this minimum impedance increases and finally transforms into the global maximum. All these effects are due to the domain susceptibility which will not be taken into account in this work. A moderate tensile stress will deepen the minimum at zero field. The anisotropy field increases with the application of tensile stress. Thus, at lower MHz frequencies, a microwire becomes stress-sensitive even in zero field. However, such stress sensitivity is of little interest for monitoring purposes due to its irregularity. Actually, the field characteristic of $|Z(H_{ex})|$ at 1 MHz can be made similar to that of 40 MHz by applying a small DC bias current (tens mA) through the microwire. Such current will eliminate the circular domain structure thereby

making the impedance model more suitable [2.34]. The model will work better for higher band MHz range and GHz frequencies where the oscillations of domain walls are strongly damped.

2.5. Monitoring of internal tensile stress in polymer materials using the microwire stress-impedance

The experimental setup used for the stress impedance measurements is shown in Fig. 2.6. It comprises an Agilent VNA, a 3.5 mm coaxial cable between the microwire and the Analyser, a bias magnetic coil (short solenoid) wound around the test part of the sample, and an Instron 5582 screw-driven universal test machine. The complex-valued microwire impedance is calculated as $Z = 50\Omega \times (1+S_{11})/(1-S_{11})$. The dog-bone sample was made of a commercial epoxy resin without reinforcements (Sicomin SR8100 epoxy with SD8824 polyamine blend standard hardener resin system). The test gauge length and cross-section are 70 mm and 5×12 mm^2, respectively. A $Co_{68}Fe_4Cr_3Si_{11}B_{14}$ microwire was embedded into the epoxy resin during the sample fabrication along its length as shown in Fig. 2.7. Obtaining reliable electrical connections between external conductors and the glass-coated microwires remains one of the most serious difficult for this type of sensor. The glass can be removed mechanically or chemically, and then the exposed end must be connected to a conductor while minimising mechanical stresses on the microwire. The method used here is as follows. The ends of the microwire and an external wire connector are put into a miniature metal tube (clamp) from opposite sides and then strongly compressed. The compression destroys the glass coating on the microwire end and provides a reliable electrical contact with the external connector. To improve the contacts, a conductive glue can be injected into the clamps before their compression. Both the contacts were then embedded into the matrix together with the microwire.

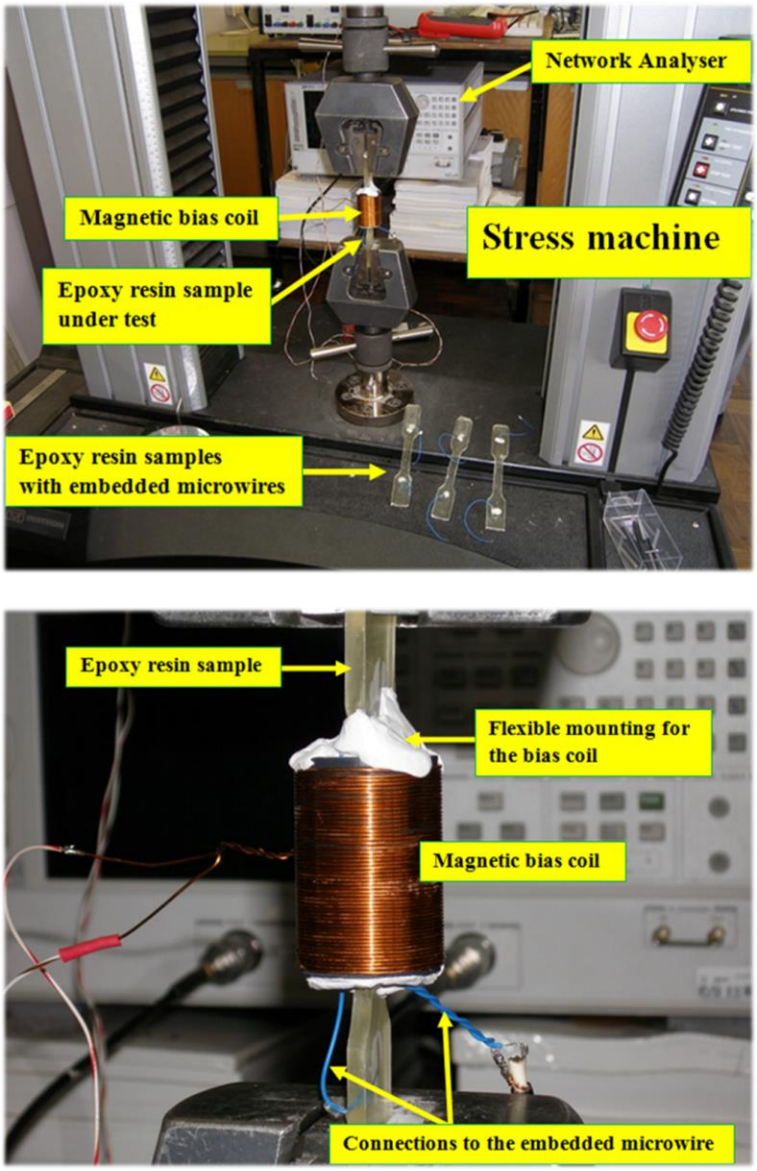

Fig. 2.6. The experimental setup and the test samples used for the stress impedance measurements.

The force-strain characteristic of the sample in Fig. 2.7 is typical of viscoelastic materials where the elastic stress monotonically transforms into the plastic one without a yield plateau. Since the stress characteristics of viscoelastic materials are time-dependent even for a constant stress or a constant strain [2.35], the test conditions must be clearly specified. In Fig. 2.7, the stress was applied in the load steps with ~ 1 min time intervals. During the pauses, the microwire impedance was automatically measured at 11 frequency points within a fixed frequency range $1-40$ MHz. This range was selected based on the dispersion properties of the stress impedance and some limitations associated with contact measurements. Below 1 MHz the stress impedance characteristics become irregular. For frequencies higher than 40 MHz,

the electronic circuitry will be much more complicated, and also the microwire impedance response becomes very sensitive to the environment. The microwire failure strain $\sim 1\%$ was found by measuring the microwire DC resistance until it became infinite when the microwire broke. Young's modulus E measured at low strain was ~ 2.5 GPa. The sample failure strain and stress were $\sim 6.5\%$ and ~ 38 MPa, respectively.

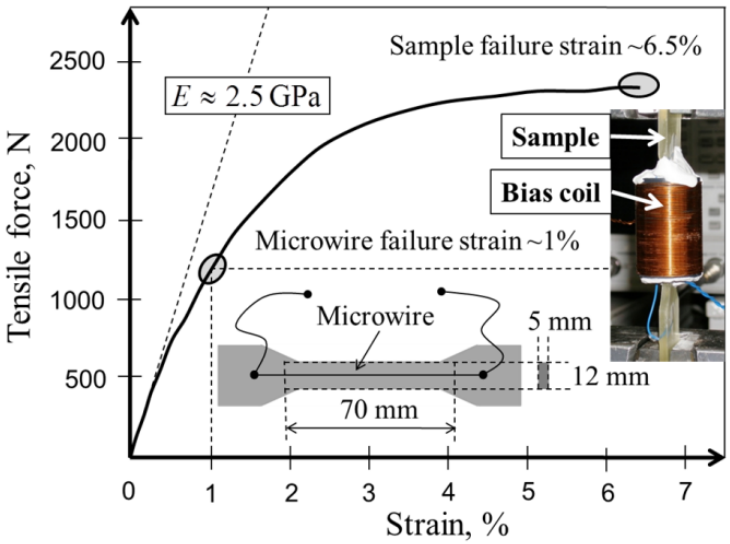

Fig. 2.7. The force-strain characteristic of the epoxy sample and its physical dimensions. Young's modulus E of the sample measured at the origin was ~ 2.5 GPa. The sample failure stress was ~ 38 MPa.

The plots of the microwire impedance Z versus applied tensile force F are shown in Fig. 2.8 for three current excitation frequencies 1, 5 and 40 MHz, and at the different axial bias magnetic fields H_{ex} induced by the short solenoid. If no bias field is applied, for 1 MHz the impedance demonstrates irregular stress sensitivity with relatively small deflections from the mean. The field of 1.1 Oe does not make any difference. The radical change in $Z(F)$ occurs at $H_{ex} = 2.1$ Oe. For this field, the maximum stress sensitivity is observed. It is already known that 2.1 Oe is the microwire anisotropy field $H_K(0)$ (see Fig. 2.3). For fields higher than $H_K(0)$, the slope of $Z(F)$ will shift toward greater stresses. A similar behaviour of the stress impedance characteristics is observed for 5 and 40 MHz, but the curves are more regular.

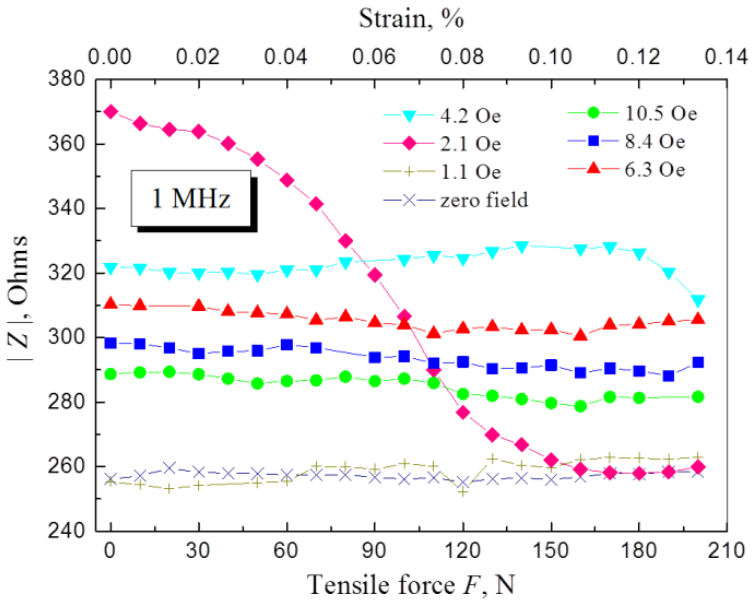
Strain, %
0.00
0.02
0.04
0.06
0.08
0.10
0.12
0.14
380
360
340
320
300
280
260
240
| Z |, Ohms
1 MHz
4.2 Oe
2.1 Oe
1.1 Oe
zero field
10.5 Oe
8.4 Oe
6.3 Oe
0
30
60
90
120
150
180
210
Tensile force F, N

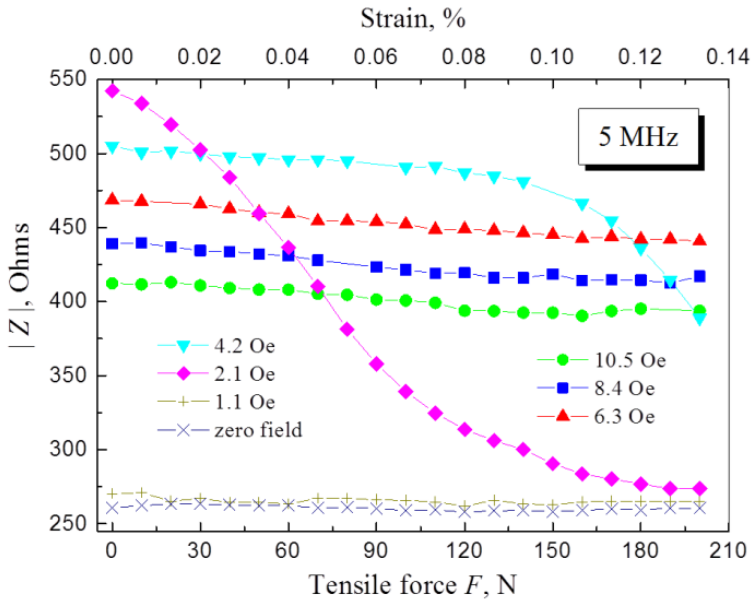
Strain, %
0.00
0.02
0.04
0.06
0.08
0.10
0.12
0.14
550
500
450
400
350
300
250
| Z |, Ohms
5 MHz
4.2 Oe
2.1 Oe
1.1 Oe
zero field
10.5 Oe
8.4 Oe
6.3 Oe
0
30
60
90
120
150
180
210
Tensile force F, N

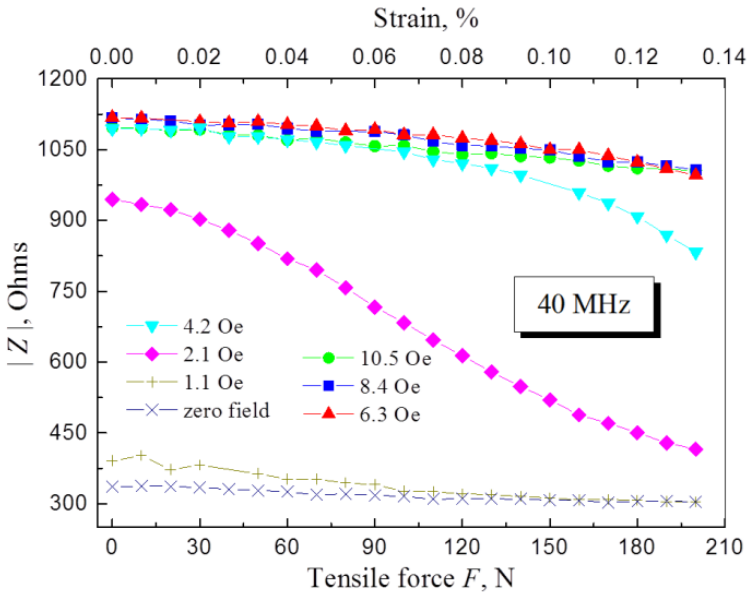

Fig. 2.8. The impedance vs. applied tensile stress measured at different axial bias fields for three excitation frequencies.

The regularity of stress impedance curves measured for 1 MHz can be improved by passing a small DC bias current (tens of mA) through the microwire to eliminate the circular domain structure in the metal core [2.34]. Measurements in this study suggest that the current excitation frequency should be between 1 and 40 MHz. Within this range, it is advisable to choose the minimum frequency that provides a good impedance characteristic with/without a DC bias current. Further increase of the excitation frequency would be problematic for a contact sensor because the buffer impedance of the external connectors will contribute significantly to the total impedance, and thus reduce the stress sensitivity.

For the microwire used in these experiments, the strain ε_S saturating the impedance (see Eq. (2.11)) was about $0.08-0.14\%$. Such a small strain might be produced, for instance, by moderate heating of the sample without any external stress. Indeed, the coefficient of linear thermal expansion of commercial epoxy resins lies in the range $(45-65)\times10^{-6}/°C$ [2.35], and hence an increase of temperature will result in $\geq 45\mu\varepsilon/°C$. Thus, a deliberate desensitisation of the stress impedance is absolutely essential for the practical use of this method. According to Eq. (2.11), this can be done by increasing the anisotropy field. For the upper limit ~ 20 Oe, ε_S may be higher than 1%, thus approaching the sample failure strain.

Therefore, the microwire can be designed so that its magnetic properties will fit a certain range of external tensile stresses.

For stress monitoring applications, there is a need for infallible bonding between the microwires and the matrix. To ensure this, the cure must be fully completed and the temperature gradually relaxed before the sample is exposed to environmental conditions. However, in service, temperature fluctuations may contribute to progressive debonding due to the difference in the thermal expansion of the microwire and the matrix. Also, there may be problems of the thermal stability of the magneto-impedance itself which will be affected by (i) the thermal drift of magnetic properties of the alloy and (ii) the change of magneto-elastic anisotropy due to the difference CTE between the metal core and the glass shell. The second effect may manifest itself at relatively low temperatures. Adenot-Engelvin et al [2.36] have shown that nanocrystalline Finemet glass-coated microwires may demonstrate perfect thermal stability up to 300 °C. In principle, for certain microwires having a proper combination of the geometrical and structural properties, very stable impedance characteristics can be obtained. The development of such alloys and microwires should be continued with close collaboration between academic institutes and wire manufacturers.

For the excitation frequency 40 MHz, the model approach has been proven to qualitatively reproduce the experimental field impedance $|Z(H_{ex})|$ and its transformational properties under the effect of external tensile stress as shown in Figs. 2.3 and 2.4. This agreement remains at higher MHz frequencies. Therefore, at least for the frequencies higher than 40 MHz, the model should also reproduce the experimental stress impedance $|Z(F)|$ shown in Fig. 2.8. However, for a bias field larger than the anisotropy field ~ 2.1 Oe, the theoretical stress impedance $|\zeta_{zz}(\sigma_{ex})|$ will have a non-monotonic behaviour with the characteristic maximum similar to that shown in Fig. 2.9 for $H_{ex} = 4$ Oe. Such maxima are not observed in the experiment (see Fig. 2.8). In the theoretical dependence of the stress impedance, the maximum at a fixed bias field is unavoidable because it is reproduced from one of the impedance maxima in $|\zeta_{zz}(H_{ex})|$ (see Fig. 2.3) when it is shifted by the stress across the vertical line defined by a fixed field $|H_{ex}| > H_K(0)$. This is a purely geometrical effect. Certainly, the experimental field impedance $|Z(H_{ex})|$ in Fig. 2.4 and its transformations under the effect of tensile stress will reproduce exactly the same stress dependence of $|Z|$ at a fixed H_{ex}.

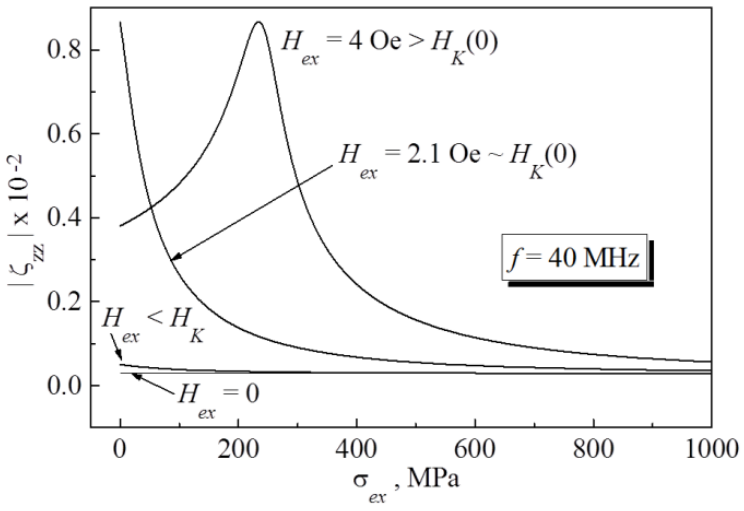

Fig. 2.9. The microwire impedance vs. applied tensile stress at different bias fields calculated using Eq. (2.8) and the magnetostatic model (2.1)-(2.5). The model parameters are the same as in Fig. 2.3. The excitation frequency is 40 MHz.

To explain the absence of the maxima in Fig. 2.8, it should be recalled that $|Z(F)|$ was measured inside an epoxy matrix, while $|Z(H_{ex})|$ in Fig. 2.4 and its transformations by stress were measured for unembedded microwire on the top of a PCB microstrip cell. This discrepancy is probably caused by residual stresses which are transferred to the microwire during embedding into the epoxy matrix and the ensuing curing processes. The stresses are input to the model through the magnetostatics (2.1)-(2.5) which has only four free parameters: a magnetisation M_0, a magnetostriction λ, a residual axial tensile stress σ_1, and a residual surface torsion stress σ_2. Varying both stresses was used in an attempt to reproduce the experimental curves in Fig. 2.8. The residual stresses in the microwire from embedding and cure cannot currently be completely described by the current model. Nevertheless, for $|H_{ex}| < H_K(0)$, the model predicts a similar monotonous decrease of the stress impedance as in the experiment. A limitation of this approach might be the simplicity of the magnetostatic model used. However, the real cause of the discrepancy with the experimental data in Fig. 2.8 for $|H_{ex}| > H_K(0)$ lies in the electrodynamic model (2.7), (2.8), which completely neglects the radial distribution of magnetic properties inside the microwire. In the MHz range, the current skin-depth may not be sufficiently small for such an assumption. In the GHz range, the model should work better because the excitation current will be strongly localised within a very

thin layer near the surface, where the magnetic properties can be considered to be homogeneous. Furthermore, the functional behaviour of $|Z(H_{ex})|$ becomes much simpler at the GHz frequencies [2.37] as the module of impedance reaches its maximum values at $H_{ex} = \pm H_K(0)$ and then remains constant for any $|H_{ex}| \rhd H_K(0)$. Consequently, the stress dependence of $|Z|$ at any fixed H_{ex} will be represented by a monotonically decreasing curve. Thus, the agreement between the theory and the experiment should be restored again.

Dependence of the magneto-impedance on the temperature $T << T_C$, where T_C is the Curie temperature (temperature at which certain materials lose their permanent magnetic properties [2.38]), is conditioned mostly by the residual axial tension σ_1 which has to be modified as $\tilde{\sigma}_1 = \sigma_1 - \Delta\sigma_{core}$ in order to take into account its temperature dependence, where $\Delta\sigma_{core}$ is defined by Eq. (1.9) (see Section 1.6.7). Since $\sigma_1 >> \sigma_2$, for the anisotropy field can be obtained as:

$$H_K(\sigma_{ex}) \approx 3|\lambda| \frac{\{\sigma_1 - \Delta\sigma_{core} + \sigma_{ex}\}}{M_0} \tag{2.12}$$

where $\Delta\sigma_{core} = \dfrac{E_{core}E_{glass}(\alpha_{core} - \alpha_{glass})\left(\left(\dfrac{D}{d}\right)^2 - 1\right)\Delta t}{E_{core} + \left(\left(\dfrac{D}{d}\right)^2 - 1\right)E_{glass}}$ and $\Delta t = T - T_{\text{Room}}$

Eq. (2.12) predicts that H_K is a linear function of T. There is a hint of such a linear dependence in Fig. (5) in the paper published by Adenot-Engelvin et al. [2.36], but this question must be investigated further. Should magnetically thermostable alloys be found, they would be of crucial importance for sensor applications.

In Fig. 2.8, the impedance characteristics measure a tensile stress averaged along the microwire because it was magnetically biased as a whole. Using such long sensing elements, local stress monitoring is also possible as explained in Fig. 2.10. A bias field induced by a weak permanent magnet can be applied locally to activate a small part of the microwire, while the rest (unbiased) remains stress insensitive. Moving the magnet along the microwire, the stress profile can be reproduced. To realise this method in practice, some bridge circuit will be needed to compensate the microwire impedance in zero field. In this case, the

voltage response caused by the change of the impedance of the activated part will be measured against zero ground level.

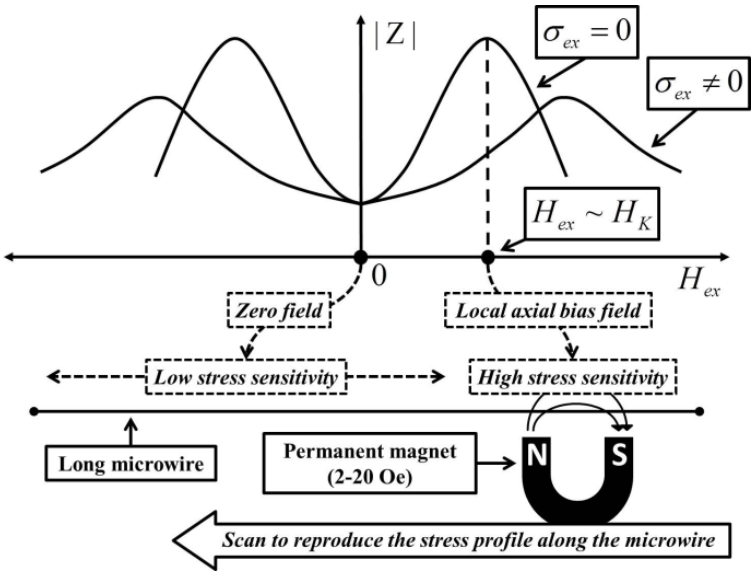

Fig. 2.10. The principle of local stress monitoring.

2.6. Summary and conclusions

The necessary physical conditions to study the tensile stress sensitivity of the high frequency impedance of ferromagnetic glass-coated microwires have been established on the basis of the simple magnetostatic and impedance models. For a glass-coated Co-based microwire having a small negative magnetostriction, the high frequency impedance becomes stress-sensitive in the presence of a weak axial DC bias magnetic field. Regular and monotonous stress impedance characteristics can be obtained for excitation frequencies within $1-40$ MHz. The impedance stress sensitivity (Ω/Pa) can be tuned by applying different axial DC bias magnetic fields. The highest stress sensitivity is achieved with a bias field of the order of the initial anisotropy field (corresponding to zero stress). It has been shown that the external tensile stress saturating the microwire impedance is defined by the residual axial tensile stress formed on the metal core/glass shell interface of the microwire during its fabrication. This property can be used to design microwires whose magnetic properties fit their mechanical properties. The principle of non-local stress monitoring using a long embedded microwire has been proposed. Measuring the total microwire impedance when a DC bias field is applied locally, it becomes possible to reproduce the actual stress profile along the microwire. The comparison of experimental stress impedance characteristics and their models

reveals a principal discrepancy indicating that post-cure stresses accumulated in the matrix (which cannot be easily taken into account in the model) may strongly affect the sensor performance.

The ability to measure internal micro-stresses using the proposed method has fairly obvious application as a laboratory test sensor. Complete practical recommendations for this method may be developed in future research works. The prospect of field applications will depend on the solution of numerous technological and technical problems, including the thermal stability of impedance and the reliability of electrical contacts between the microwire and the external electronics.

Chapter III

Design of fixtures for high frequency impedance measurements

After the first publications on tuneable microwave scattering in composites with ferromagnetic microwires, several research groups have shown interest in this subject. However, difficulties with the laboratory integration of microwave and stress/temperature measurements continue to hamper the development of practical methods of non-destructive testing by means of the scattering of microwires.

Design of measurement fixtures remains the main obstacle to study of high frequency impedance properties of microwires subjected to external stimuli such as tensile stress and temperature. This chapter partly addresses this issue for contact measurements. Development of fixtures for free space measurements is an agenda for the future research.

3.1. Microstrip cells

Special PCB (Printed Circuit Board) microstrip cells in the shape of a dog-bone were fabricated for stress-impedance experiments. In total, six such PCB cells were made from FR4 (composite material composed of woven fiberglass cloth with an epoxy resin binder) sheets of two different thicknesses (see Fig. 3.1). Three samples had a thickness of 0.8 mm and the other three had a thickness of 1.6 mm. The overall dimensions of these dog-bone samples are presented in Fig. 3.2. Microstrips were etched onto one side of FR4 sheets, while the reverse side consisted of a continuous ground plane. Then, the required cells were cut out, shaped and smoothened from these laminates using a PCB shearing machine, a Dremel rotary cutter (see Fig. 3.3), and sandpaper. A “dog-bone” shaped specimen was used, which are common in tensile stress experiments. As stresses in the narrow central gauge section are higher than in the flared regions of the specimen, effects of stress can be investigated in this region. Also, the change of widths is in the form of smooth curves that minimise stress concentrations that may otherwise fracture the sample. Several additional rectangular microstrip cells (see Fig. 3.4) were also fabricated for the purpose of calibration and temperature-impedance experiments. The 3.5 mm SMA connectors (semi-precision coaxial RF connectors with 50Ω impedance) were soldered to the cells (see Fig. 3.4 and Fig. 3.5), enabling coaxial cable connections to the VNA ports.

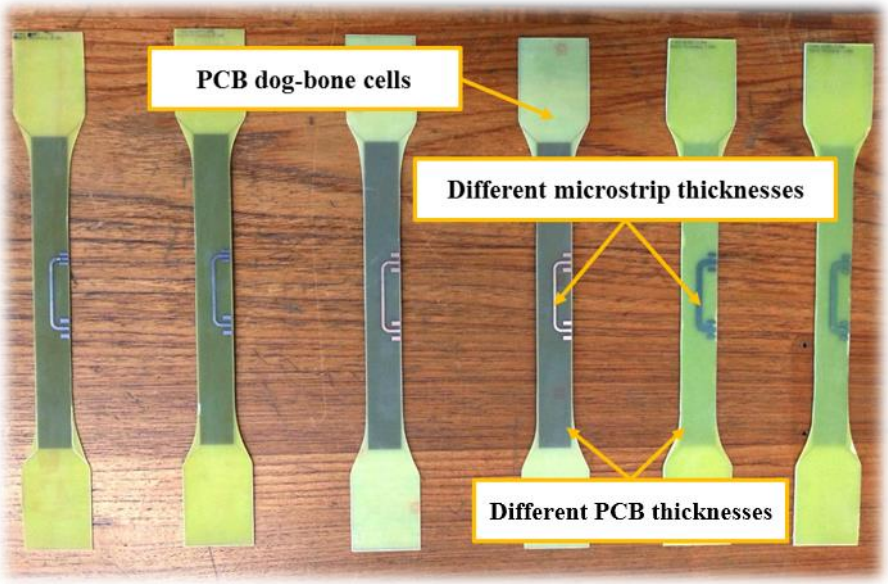

Fig. 3.1 Dog-bone microstrip cells used for the stress-impedance measurements: before soldering the SMA connectors and cutting the gap in the microstrip for a microwire sample. Different microstrip thicknesses provide ~50Ω wave impedance (50Ω is a standard used in RF engineering and RF measurements [4.3]) for FR4 PCBs of 0.8 mm and 1.6 mm thicknesses.

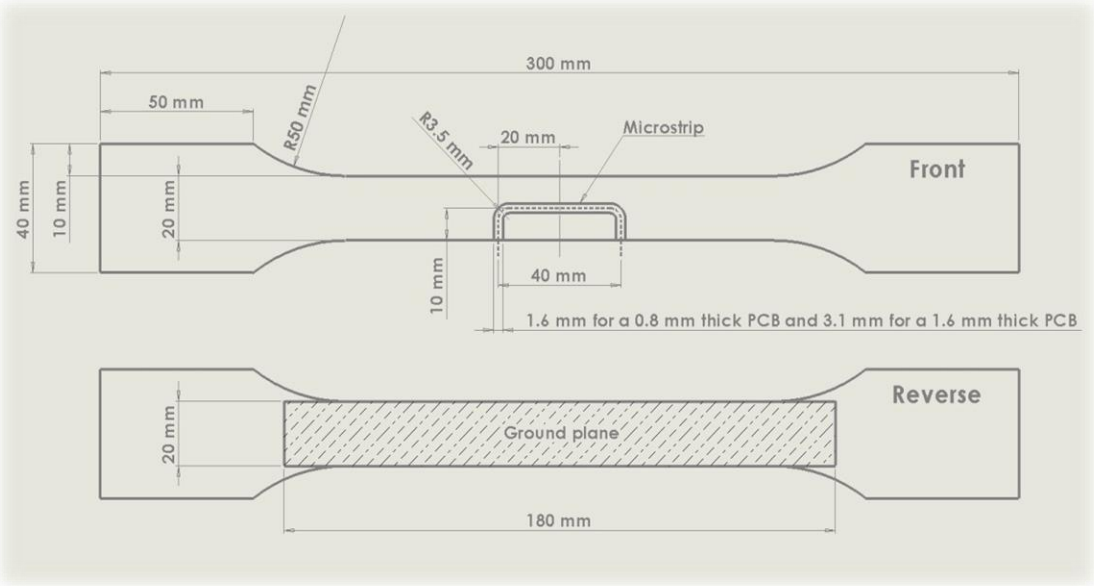

Fig. 3.2. Dimensions of the PCB dog-bone microstrip cells

Fig. 3.3. Dog-bone cells being cut from FR4 PCBs with the help of a Dremel rotary cutter.

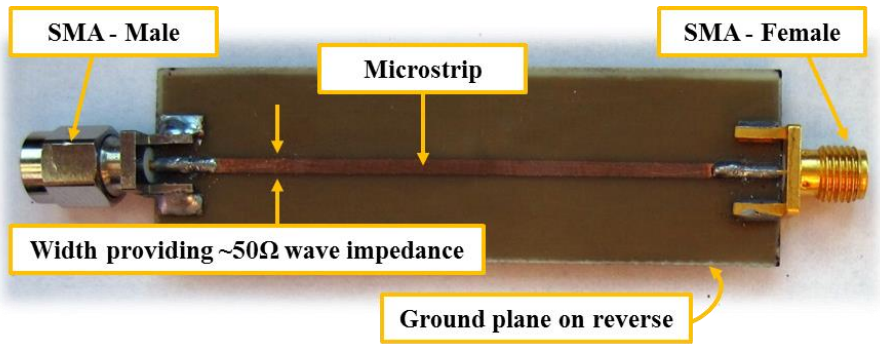

Fig. 3.4. The straight microstrip cells used for the temperature-impedance experiments: before cutting the gap in the microstrip for a microwire sample. The 3.5 mm SMA connectors are soldered to the cell to provide coaxial cable connections.

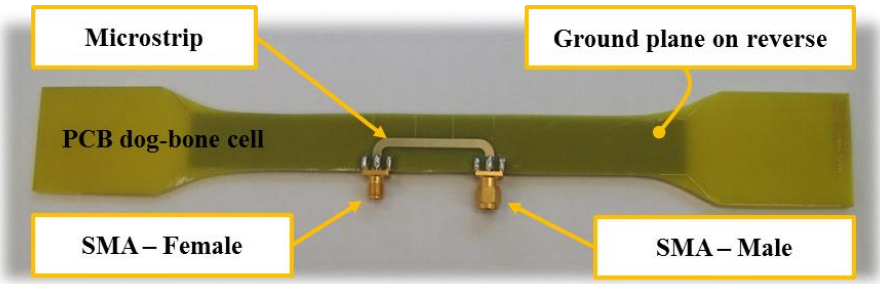

Fig. 3.5. A PCB dog-bone microstrip cell equipped with SMA-Male and SMA-Female connectors. A gap in the microstrip will later be cut out to allow a microwire sample to be attached between the microstrip ends.

3.2. Strain vs. stress dependence in the measurement cells

PCB dog-bone cells of 0.8 mm and 1.6 mm thicknesses were stretched in order to determine their mechanical properties such as their yield and ultimate tensile strengths. The stress-strain curve obtained gave an overview of the forces required to obtain a certain strain in the central part of the cell (where a microwire sample is placed) and also helped to establish a test sequence for the stress-monitoring experiments. The PCB dog-bone cell was clamped between the two jaws of a stress machine. Tensile forces in increments of 100 N or 200 N were applied until failure. After each increment, there was a small pause of a few minutes while the Analyser performed a frequency scan and measured the S_{21}-parameter (transmission coefficient, described in detail in Section 4.2) through a microwire sample in discrete frequency points. To accurately measure the strain, an extensometer was attached to the central part of the cell as explained later. The obtained strain-to-stress characteristic then was compared with the strain measured by a strain-gauge fixed centrally on the reverse of sample as shown in Fig. 3.6.

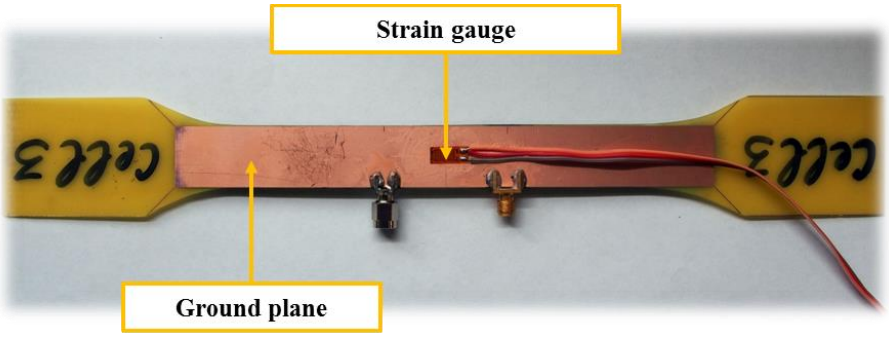

Fig. 3.6. A strain-gauge fixed centrally on the reverse of sample was used to verify the strain-to-stress characteristic obtained by means of the extensometer.

Strain-gauge used was Vishay EA-06-120LZ-120/E together with a P3 Strain Indicator and Recorder. Strain values obtained from the strain-gauge and the extensometer were recorded for the dog-bone cells. The strain vs. stress dependencies obtained from the extensometer and the strain-gauge for a dog-bone cell of 1.6 mm thickness are shown in Fig. 3.7. The proportionality coefficients for these almost linear dependencies with zero offsets differ by the factor ~ 1.07. A similar result was observed for the dog-bone cells of 0.8 mm thickness. As these coefficients are very close, strain values obtained from the extensometer will be used for the recalculation of stress into strain.

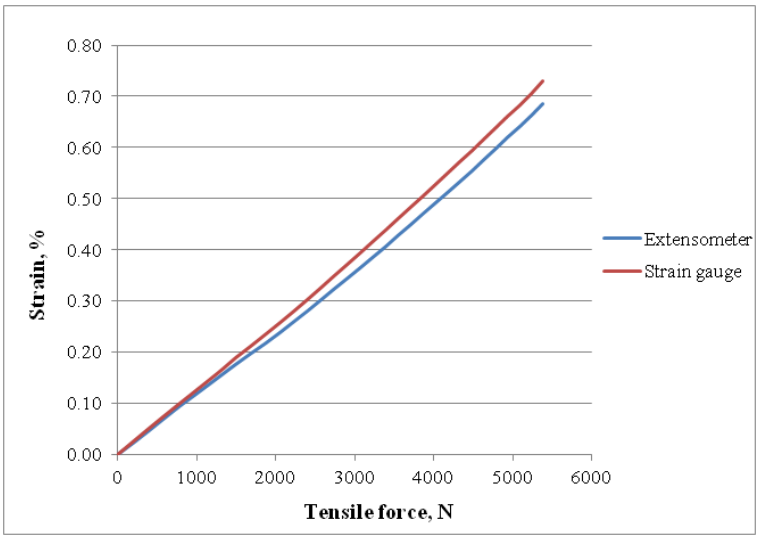

Fig. 3.7. Graphical representation of values of strain obtained from extensometer and strain-gauge against tensile force for a dog-bone cell of 1.6 mm thickness.

3.3. Stress-impedance measurements at RF frequencies

The experimental setup used for stress-impedance measurements at the RF frequencies is shown in Fig. 3.8. It includes an Agilent VNA, long coaxial SMA 3.5 mm cables connecting the cell with the Analyser, a Helmholtz coil (described overleaf) encompassing the central test section of dog-bone cells, an Agilent programmable function generator providing ± DC offset voltages for a power amplifier that feeds the coil, and an Instron 5582 screw-driven universal test machine. For the field-impedance, the operation of the function generator and VNA must be synchronised: the DC voltage supplied for the power amplifier is changed by an incremental value after each frequency sweep in a number of discrete points. For the stress-impedance measurements, the DC voltage will have a fixed value (fixed bias field). All control programs were written in Agilent VEE 6.0 graphical programming language. To insert a microwire, a short gap is cut in the central part of continuous microstrip. The method for connecting microwires to the gap ends will be described later in this section (see Fig. 3.15).

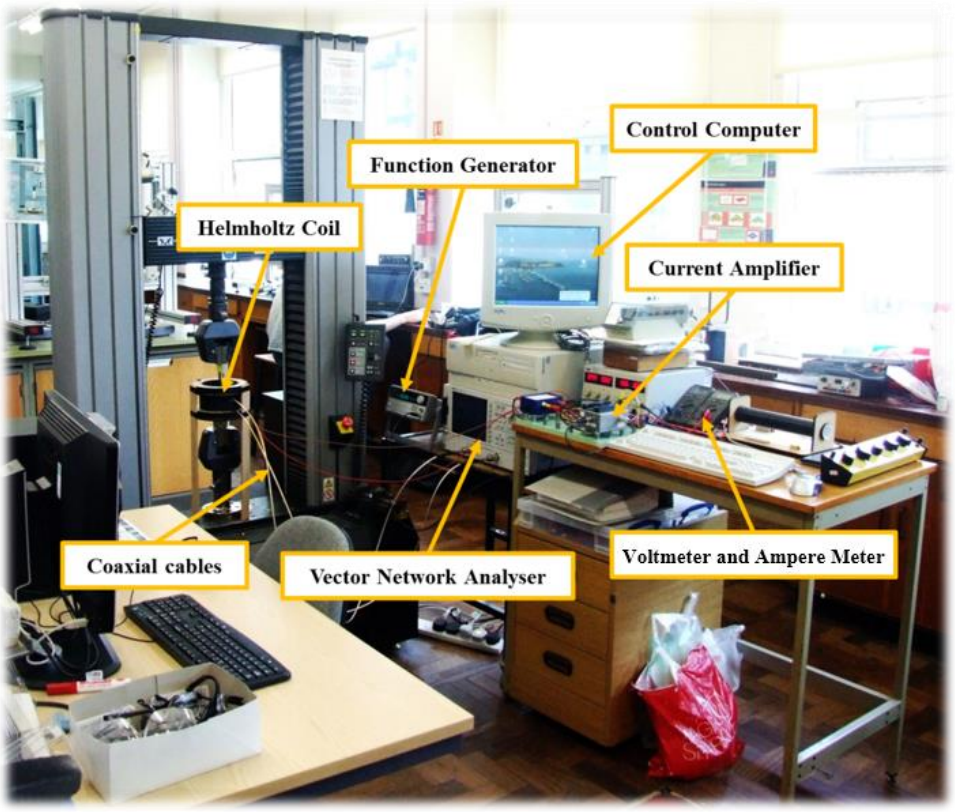

Fig. 3.8. Experimental setup used for RF stress-impedance measurements.

For the purpose of generating a uniform magnetic field around the central part of dog-bone microstrip cells containing microwires as well as providing access to the cell for the cables and extensometer, a special Helmholtz coil with holes and "windows" was fabricated as shown in Fig. 3.9. Circular discs were cut out of 10 mm sheets of Medium Density Fibreboard (MDF) using a laser cutter which were then glued together to form the shape of the Helmholtz coil. On this structure, KG 1.00mm D/C Polyester Grade 2 Enamelled Copper Wire was wound and the coil was completed. The Helmholtz coil needed to be positioned centrally between a dog-bone microstrip cell that was held between jaws of the stress machine as shown in Fig 3.10. To accomplish this, the distance between the centre of the PCB dog-bone sample held in the fixed jaw of the stress machine was measured and three "supports" were cut out from MDF accordingly and fixed to the Helmholtz coil. Two holes were drilled through the central coil cylinder to insert coaxial cables. Then, a rectangular window was cut out facing the reverse surface (ground plane) of the dog-bone microstrip cell, through which an extensometer could be attached on the central part of the cell.

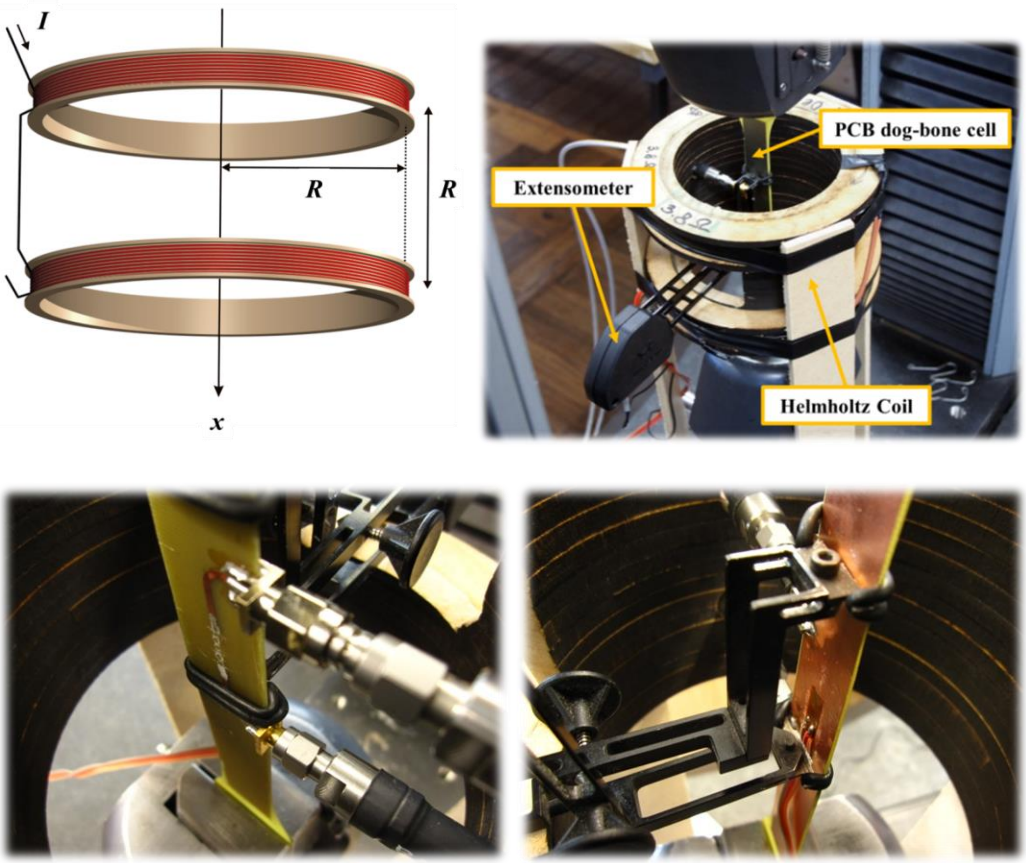

Fig. 3.9. Helmholtz coil with holes and windows providing access to the cell for the cables and the extensometer.

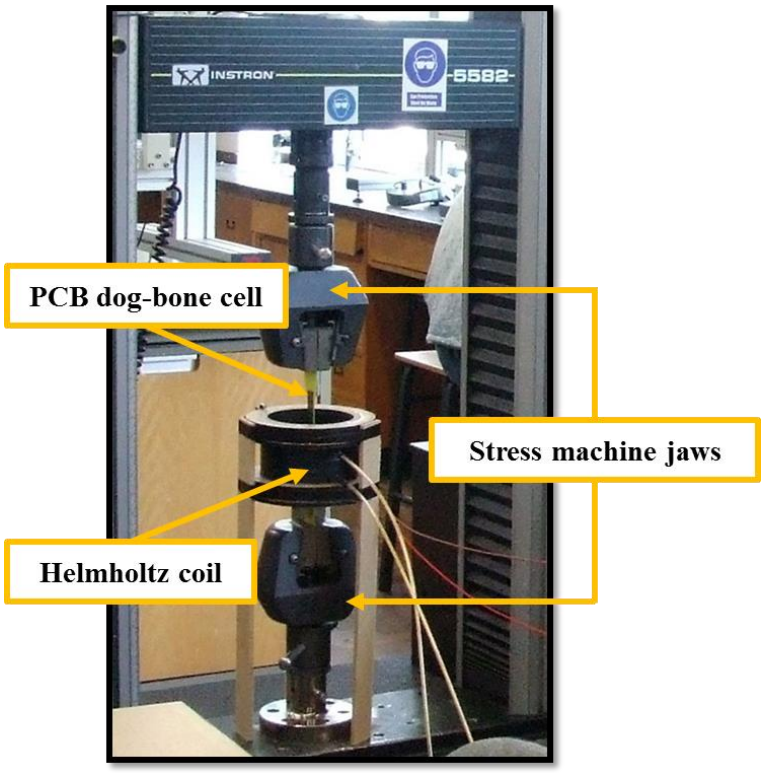

Fig. 3.10. Position of Helmholtz coil with respect to the cell.

3.4. Preparation of the microwire samples and their mounting onto the measurement cells

One of the common difficulties when preparing the microwire samples is the removal of the glass shell at the ends of a microwire piece. Good electrical connection between the microwire ends and microstrips is only possible if the outer glass shell is sufficiently removed exposing the metal core. The sample preparation involves stripping the microwire ends of its glass shell and connecting them to microstrips by solder, clamps, conductive epoxy or paint. In the experiments of Chapter II, the ends of the microwires were connected to external wires by placing the exposed ends into miniature metal tubes (clamps) from opposite sides and then strongly compressing. Compression destroyed the glass coating on the microwire end resulting in an electrical connection between the microwire and the external wire. In the experiments that follow, the ends of a microwire need to be connected to the surface of microstrips and as a result the previously described method cannot be used. The method of removal of the glass shell for the following experiments is with the help of a scalpel. A microwire segment is placed on a sheet of paper and held in place with a finger. A scalpel is then used to carefully strip the microwire end of its glass shell. This procedure is then repeated on the other end of the microwire. This method gave consistent results. Other methods such as, tapping the end of microwire segment with a blunt instrument in order to fracture and remove the glass shell gave poor results and often deformed the core material. The structure of microwire before and after glass removal was observed in a digital microscope (Fig. 3.11).

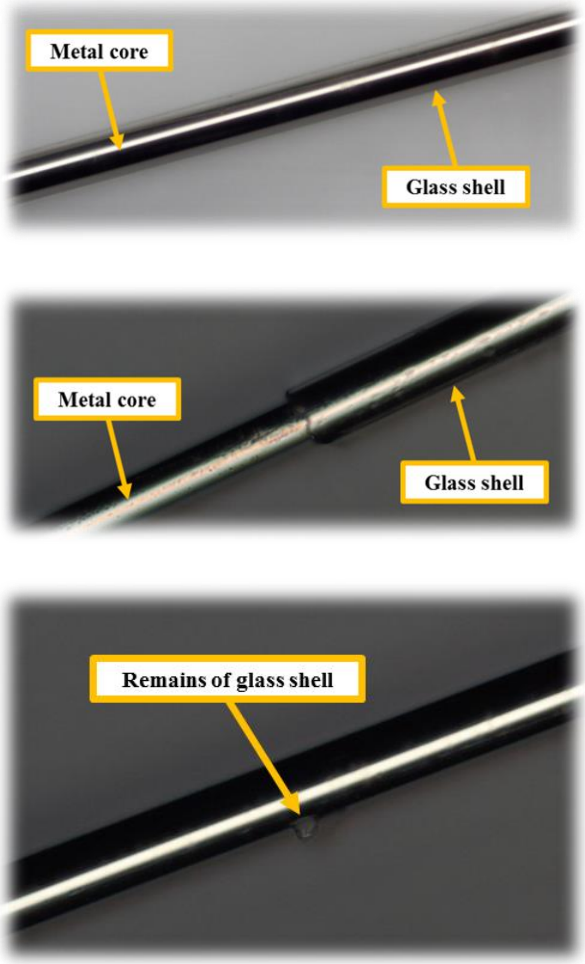

Fig. 3.11. A piece of microwire before and after the removal of glass insulation observed in a digital microscope.

There were six PCB dog-bone cells (three of 0.8 mm thicknesses and three of 1.6 mm thicknesses) used in experiments. Two of them (0.8 mm and 1.6 mm thickness) were used for calibrating the stress-to-strain dependence. The cell was clamped between the jaws of the stress machine and the tensile stress was applied in load steps of 100 or 200 N (depending on the board thickness) with ~ 8 min time intervals. During each pause, the S_{21} -parameter was automatically measured at 1601 frequency points within a wide frequency range covering several Gigahertz. The frequency scan was repeated several times during the pause for different bias magnetic fields ranging from 0 to 10 Oe. The stress applied was well within the elastic limit of the dog-bone PCB cell as determined earlier during stress-strain analysis. Most stress-impedance experiments consisted of 30 and 40 steps, which resulted in the total experiment times of approximately 5 hours (excluding the time required for preparation).

The microstrips were prepared to accommodate a microwire sample: a gap of 10 or 14 mm was cut off by the scalpel as shown in Fig. 3.12. The length of microwires was slightly larger to allow their connection to the microstrips. After the removal of glass, the microwire ends might take the shape of "pig tails". Then, the microwire was glued between the microstrip ends using a conductive paint as shown in Fig. 3.13.

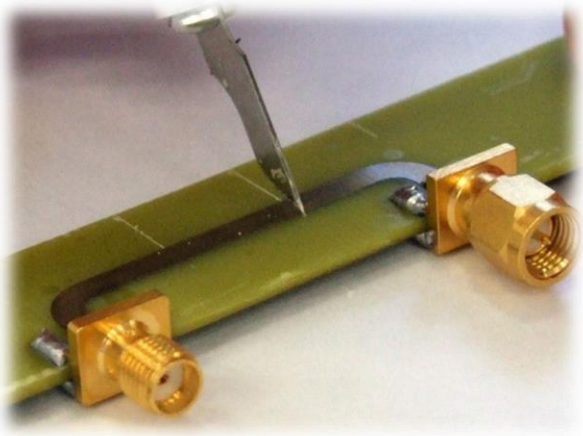

Fig. 3.12. Cutting a gap in the microstrip to allow connection of a microwire sample.

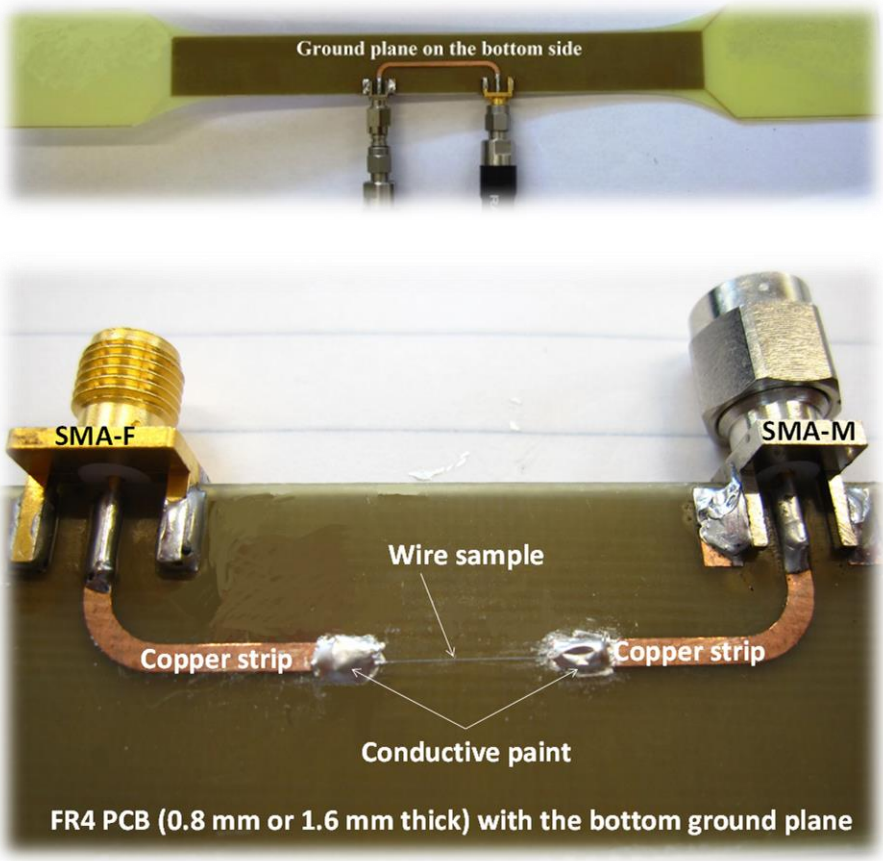

Fig. 3.13. A microwire sample is connected to the microstrip ends using a conductive paint.

3.5. Fixtures for the temperature-impedance measurements

Experiments with low Curie temperature (T_C) microwires were carried out to observe and measure any significant temperature-dependent effects on the magneto-impedance of the microwire. These experiments did not involve application of external stresses. The microwire magneto-impedance was measured for room temperature (~21 °C) and then at a higher temperature above T_C. Microstrip cells such as those shown in Fig. 3.4 were used. Some measurement fixtures would need to be created that would hold the microstrip cell and allow a small central area of the cell to be heated, without heating other components, such as the SMA connectors and the coaxial cables. Such fixtures were designed using CAD software and then manufactured from a 10 mm thick MDF board. They comprise a Helmholtz coil with a small heat chamber holding the cell shown in Fig. 3.14. The Helmholtz includes a window on the top allowing external airflow heating and two windows at the bottom, through which hot air could escape. A simple hairdryer was used as an airflow heater, but in the future a more sophisticated heating control system should be

designed. The microstrip cell is slid into the heat chamber through thin slots and can be then connected to coaxial cables as shown in Fig. 3.15.

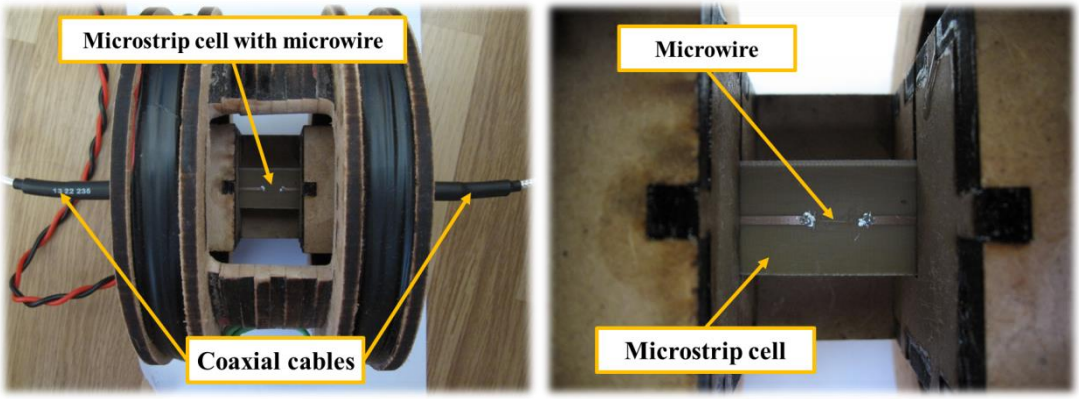

Fig. 3.14. The Helmholtz coil with a small heat chamber holding the cell. Only the central area of the cell is exposed to the heating, while the cables and connectors are out of the hot air flow and protected.

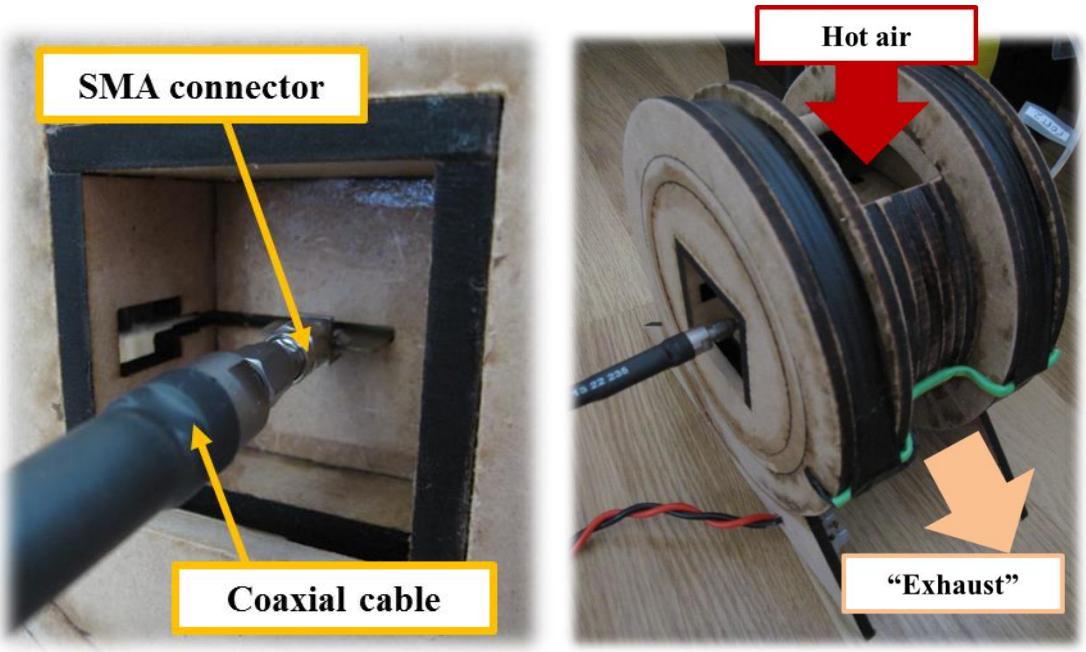

Fig. 3.15. Side view of the Helmholtz coil and the heat chamber showing the slot, the SMA connectors, and the coaxial cable. The cables and connectors are out of the hot air flow and protected.

Chapter IV

Calibration of measurement cells and measurement of the high frequency surface magneto-impedance at GHz frequencies

When increasing the excitation frequency, a microwire passes into a regime of strong skin-effect where the current distribution becomes more sensitive to inhomogeneities of magnetic properties near the surface of ferromagnetic core. In this case, enhanced impedance stress sensitivity should be expected. Thus, the very high frequencies up to the GHz range may appear to be useful for the stress monitoring applications. However, at such high frequencies the contact methods become practically unsuitable due to the parasitic parameters in connectors and cables as well as the microwire external inductance that significantly reduce the useful change of impedance absolute value. To overcome these distortions, in practice microwires should be interrogated remotely, for example, using near field antenna or waveguide measurements.

In this chapter, experimental methods allowing accurate measurements of the surface magneto-impedance of microwires at the GHz frequencies in the presence of tensile stress or heat will be developed. The surface magneto-impedance of a microwire delivered from such measurements can be used for modelling microwave response remotely in free space both from an individual inclusion or their conglomerates.

4.1. Surface impedance and antenna equation

The surface impedance parameter ζ_{zz} (one of the four components of the surface impedance tensor) introduced in Eq. (2.6) is the only wire material parameter, including its conductive and magnetic properties, in the integro-differential equation that describes the current distribution in a microwire irradiated by an electromagnetic wave [4.1]:

$$\frac{d^2}{dz^2}(G*i)+k^2(G*i)=\frac{j\omega\varepsilon}{4\pi}\bar{e}_{0z}-\frac{j\omega\varepsilon\zeta_{zz}}{2\pi ac}(G_{\varphi}*i) \qquad (4.1)$$

The main goal in this chapter will be to develop the experimental techniques for measurement of the high frequency dispersion of ζ_{zz} that can be used for modelling together with Eq. (4.1). Equation (4.1) is written in Gaussian-cgs with slightly different designations than those in Ref. [4.1]:

- $i(z)$ is the linear current density (the time dependence $\sim\exp(-j\omega t)$) along a thin conductor related to the volume current density as $i(z)\delta_S(x,y)$, where $\delta_S(x,y)$ is two dimensional Dirac's function. The current density $i(z)$ is enough to describe the radiation essential polarisation

(e_z, h_φ) required to satisfy the impedance boundary conditions for the longitudinal electric (e_z) and circular magnetic (h_φ) fields (further discussions on the linear current can be found in Ref. [4.1]).

- $(G*i) = \int_{-l/2}^{l/2} i(s)G(r)ds$ is the convolution of $i(z)$ and the Green function $G(r) = \frac{\exp(jkr)}{4\pi r}$ of the Helmholtz equation, where $r = \sqrt{(z-s)^2 + a^2}$, $k = (\omega/c)\sqrt{\varepsilon\mu}$ is the wave number, and l is the microwire length.
- $(G_\varphi * i) = \int_{-l/2}^{l/2} i(s)G_\varphi(r)ds$ is the convolution of $i(z)$ with $G_\varphi = \frac{a^2(1-jkr)\exp(jkr)}{2r^3}$.
- $\bar{e}_{0z}$ is the projection of the surface electric field in the electromagnetic wave onto the microwire axis. Note that $\bar{e}_{0z}$ may be a periodical function of z if the wave vector in the incident wave is not perpendicular to the microwire axis.
- ε is the relative permittivity of the medium, to which the microwire is embedded.
- $c \approx 3\times10^{10}$ cm/s is the speed of light.

Formally, ζ_{zz} can be expressed through the impedance Z: $\zeta_{zz}^{\mathrm{SI}} = 2\pi aZ/l$ or $\zeta_{zz}^{\mathrm{cgs}} = 10^9 aZ/(2cl)$. These simple relations could be used for obtaining ζ_{zz} experimentally from a contact measured Z. However, they are true only if Z was measured as a lumped parameter. This condition is satisfied if the wavelength of a mode propagating along the microwire is much larger than its length. Otherwise, we have to propose a waveguide method for measuring the linear impedance Z/l. But, even when the microwire is sufficiently small, the measurement fixtures delivering the excitation signal to the sample may introduce a very strong distortion. In this chapter, a simple microwave calibration technique able to virtually eliminate the effect of fixtures for the specific measurement RF used cells will be developed. The microwire sample will be assumed sufficiently small to allow interpretation of Z as a lumped parameter.

4.2. Microwave calibration of the measurement cells

The theory of linear networks deals with signals that can be represented as a whole wave shape or decomposed into a set of harmonics having a discrete or continuous spectrum. These two representations are called the time and frequency domains respectively. Since a linear network does not change the frequency, each harmonic propagating through it will acquire some phase shift and new amplitude. A convenient way to describe this transformation is to represent the harmonic as a complex exponent $A(\omega)\exp(\pm j\omega t)$ multiplied by a complex number $\hat{F}(\omega) = |\hat{F}(\omega)|\exp(j\arg(\hat{F}(\omega)))$, where $A(\omega)$ is the harmonic amplitude (a real number depending on the frequency). The complex function $\hat{F}(\omega)$, which contains an amplitude and phase, is called the transfer function of a linear network in the frequency domain. The most general form for representing a linear transformation in the time domain is the convolution [4.2]:

$$b(t) = \int_{-\infty}^{t} F(t-s)a(s)ds \qquad (4.2)$$

where $a(t)$ and $b(t)$ are the input and output signals respectively, and $F(t>0)$ is some real kernel. The integration in Eq. (4.2) is carried out in the range $[-\infty, t]$ due to the causality principle. From the mathematical point of view, the time and frequency domains are equivalent because $\hat{F}(\omega)$ and $F(t>0)$ can be transferred into each other by means of the direct and inverse Fourier transforms. However, practical implementation of these methods requires very different hardware tools resulting in specific limitations for each method.

For the intended applications in the frequency domain, all operators are simple multiplicators. A two-port network, schematically shown in Fig. 4.1, takes in the input signals $a_{1,2}$ (from both sides) and then transforms them to the output signals $b_{1,2}$. The operation of a two-port linear network can be described by the following linear relations written in the matrix form:

$$\begin{cases} b_1 = S_{11}a_1 + S_{12}a_2 \\ b_2 = S_{21}a_1 + S_{22}a_2 \end{cases} \Rightarrow \begin{pmatrix} b_1 \\ b_2 \end{pmatrix} = \begin{pmatrix} S_{11} & S_{12} \\ S_{21} & S_{22} \end{pmatrix} \begin{pmatrix} a_1 \\ a_2 \end{pmatrix} \qquad (4.3)$$

where

$$\begin{pmatrix} S_{11} & S_{12} \\ S_{21} & S_{22} \end{pmatrix} = \hat{\mathbf{S}} \qquad (4.4)$$

is called the scattering matrix or S-matrix. Its components S_{ij}, complex coefficients which usually depend on the frequency, are called the *S*-parameters. They are defined as the following ratios: $S_{11} = (b_1/a_1)_{a_2=0}$ and $S_{22} = (b_2/a_2)_{a_1=0}$ (reflection coefficients), $S_{12} = (b_1/a_2)_{a_1=0}$ and $S_{21} = (b_2/a_1)_{a_2=0}$ (transmission coefficients). For a linear network, all these ratios can be measured using a VNA. Before measurements of the S -parameters, VNA together with the coaxial cables connected to its ports must be calibrated using the full 2-port calibration with the SHORT, OPEN, LOAD, and THRU (SOLT) coaxial standards [4.3].

Fig. 4.1. A 2-port network with the input and output signals.

For the stress-impedance measurements, the microstrip cells shown in Fig. 3.13 were used. They comprise the standard FR4 PCB with thickness 0.8 mm or 1.6 mm cut to the shape of a dog bone. A continuous curved stripe is etched on one side of PCB. The strip ends are soldered to the SMA-Female and SMA-Male coaxial connectors. The other side of PCB is left with continuous copper that forms a common ground plane for both the SMA connectors. The width of stripes should ensure the 50 Ω characteristic (wave) impedance that can be matched using a microstrip calculator available on the web. For these calculations, the main parameter is the dielectric constant $\varepsilon_{\mathrm{FR4}}$ of FR4 composite which is defined by the proportion of epoxy matrix and glass fibre filler. The value of $\varepsilon_{\mathrm{FR4}}$ lies between 3.4 (epoxy) and 6.11 (glass). For the epoxy content by weight 40-65%, $\varepsilon_{\mathrm{FR4}} \sim 4.2 - 4.9$. The exact value of $\varepsilon_{\mathrm{FR4}}$ in a finished copper laminated PCB is rarely provided by vendors. Moreover, it demonstrates frequency dispersion. These and other tolerance factors make impossible a very accurate impedance matching in a wide frequency range. Fortunately, these uncertainties are no longer critical when using a calibration. 1.6 mm wide strip for a 0.8 mm thick PCB and the 3.1 mm wide strip for a 1.6 mm thick PCB were etched that provided the characteristic impedance close to 50 Ω.

The universal model applied to the coaxial or microstrip line is shown in Fig. 4.2. It consists of a signal line (strip or wire) and a continuous ground (plane or shell) which are separated by a dielectric. The

line is characterised by the distributed parameters (SI units are used): the resistance per unit length of signal line R (Ω/m), the inductance per unit length of signal line L (H/m), the conductance per unit length G (S/m) between the signal line and the ground, and the capacitance per unit length C (F/m) between the signal line and the ground. For a harmonic excitation, the voltage $V(x)$ between a point x on the signal line and the ground as well as the current $I(x)$ along the signal line will satisfy the following system of linear differential equations (traditionally, the time dependence $\sim \exp(+j\omega t)$ is used in these equations) [4.4],[4.5]:

$$\begin{cases} \dfrac{dV(x)}{dx} = -(R + j\omega L)I(x) \\ \dfrac{dI(x)}{dx} = -(G + j\omega C)V(x) \end{cases} \tag{4.5}$$

Solving these equations, the voltage and current waves running along the line is obtained:

$$\begin{cases} V(x) = A\exp(-\gamma x) + B\exp(\gamma x) \\ I(x) = \dfrac{A}{Z_0}\exp(-\gamma x) - \dfrac{B}{Z_0}\exp(\gamma x) \end{cases} \tag{4.6}$$

where

$$\gamma = \sqrt{(R + jL\omega)(G + jC\omega)} \tag{4.7}$$

$$Z_0 = \sqrt{\frac{R + jL\omega}{G + jC\omega}} \tag{4.8}$$

In Eq. (4.6), $\sim \exp(-\gamma x)$ and $\sim \exp(\gamma x)$ are the transmitted and reflected waves, respectively. Together, they form a standing wave.

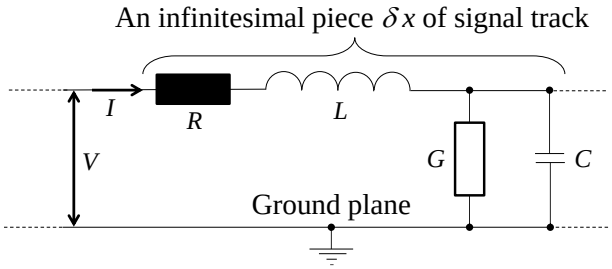

Fig. 4.2. The universal model of a transmission line with distributed parameters.

Consider an infinite line or a line terminated with the matched impedance Z_0 which is interrupted by a serially connected DUT as shown in Fig. 4.3. The distance between the harmonic voltage source (also matched) and DUT is l. According to Eq. (4.6), before DUT we will have both the transmitted and reflected waves, while after DUT only the transmitted wave (no-reflection condition at the right):

$$\begin{cases} V_{\bullet\mathrm{DUT}}(x) = A\exp(-\gamma x) + B\exp(\gamma x) \\ I_{\bullet\mathrm{DUT}}(x) = \dfrac{A}{Z_0}\exp(-\gamma x) - \dfrac{B}{Z_0}\exp(\gamma x) \\ V_{\mathrm{DUT}\bullet}(x) = C\exp(-\gamma x) \\ I_{\mathrm{DUT}\bullet}(x) = \dfrac{C}{Z_0}\exp(-\gamma x) \end{cases} \tag{4.9}$$

where "$\bullet$DUT" and "DUT$\bullet$" mean the functions of x before and after DUT, respectively. If the length of electromagnetic wave along DUT is much larger than its length, DUT can be characterised by a lumped impedance Z_{D}. In this case, the length of DUT can be neglected and the following boundary conditions can be written (the voltage drop and the current continuity):

$$\begin{cases} V_{\bullet\mathrm{DUT}}(l) - V_{\mathrm{DUT}\bullet}(l) = Z_{\mathrm{D}} \times I_{\bullet\mathrm{DUT}}(l) \\ I_{\bullet\mathrm{DUT}}(l) = I_{\mathrm{DUT}\bullet}(l) \end{cases} \tag{4.10}$$

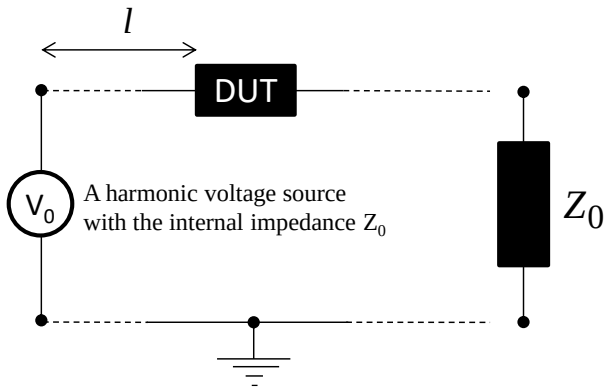

Fig. 4.3. An infinite line or a line terminated with the matched impedance Z_0 which is interrupted by a DUT connected in series.

Putting Eq. (4.9) into Eq. (4.10), we obtain:

$$\begin{cases} A\exp(-\gamma l)\left(1-\frac{Z_{\mathrm{D}}}{Z_0}\right)+B\exp(\gamma l)\left(1+\frac{Z_{\mathrm{D}}}{Z_0}\right)-C\exp(-\gamma l)=0 \\ A\exp(-\gamma l)-B\exp(\gamma l)=C\exp(-\gamma l) \end{cases} \tag{4.11}$$

Dividing both the equations in the system (4.11) by $A\exp(-\gamma l)$, we obtain:

$$\begin{cases} \left(1-\frac{Z_{\mathrm{D}}}{Z_0}\right)+S_{\mathrm{D11}}\exp(2\gamma l)\left(1+\frac{Z_{\mathrm{D}}}{Z_0}\right)-S_{\mathrm{D21}}=0 \\ 1-S_{\mathrm{D11}}\exp(2\gamma l)=S_{\mathrm{D21}} \end{cases} \tag{4.12}$$

where $S_{\mathrm{D11}}=B/A$ (reflection from DUT) and $S_{\mathrm{D21}}=C/A$ (transmission through DUT). Excluding $S_{\mathrm{D11}}\exp(2\gamma l)$ in Eq. 4.12, we finally obtain:

$$Z_{\mathrm{D}}=Z_0\times\frac{2(1-S_{\mathrm{D21}})}{S_{\mathrm{D21}}} \tag{4.13}$$

The equality in Eq. (4.13) as well as $Z_0=50$ for a 50 Ω transmission line must be understood only as approximate. For a wire on the top of PCB, the effective permittivity for the wave propagation will be $\varepsilon_{eff}<\varepsilon_r$, where ε_r is the relative permittivity of the PCB dielectric. For the wave length, we have:

$$\lambda(\mathrm{cm})=\frac{30}{f(\mathrm{GHz})\sqrt{\varepsilon_{eff}}} \tag{4.14}$$

Following the strong criterion $l < \lambda/10$, where l is the length of wire sample, the maximum frequency that can be admitted to allow the characterisation of this sample by a lumped impedance can be estimated as:

$$f_{\max}(\text{GHz}) \sim \frac{3}{l(\text{cm})\sqrt{\varepsilon_{eff}}} \tag{4.15}$$

Putting in Eq. (4.15) $l \sim 1$ cm and $\varepsilon_{eff} \sim 1.36$ (calculated from Eq. (4.25) with $h = 1.6$ mm, $a = 12$ μm, and $\varepsilon = 4.5$), we obtain: $f_{\max} \sim 2.6$ GHz. Therefore, for $l \sim 1$ cm, Eq. (4.13) will be most accurate for frequencies below ~ 2.6 GHz. For higher frequencies, the effects of wave propagation along the wire should be taken into account.

To reveal the main features of the wave propagation in the microstrips used in the experiments, the S_{21} parameter will be measured for a continuous microstrip (without a gap) in a wide frequency range. The sinusoidal frequency dependence of the real and imaginary parts of $S_{21}(f)$ together with the synchronous decay of their amplitudes shown in Fig. 4.4 suggests the following fitting function:

$$S_{21}(f) = A(f) \times \exp(j \arg[S(f)]) = A(f) \times \exp(-j 2\pi f \Delta t) \tag{4.16}$$

where Δt is the time delay (group time delay) and $A(f) = \sqrt{\text{Re}^2[S_{21}(f)] + \text{Im}^2[S_{21}(f)]}$ is the amplitude factor which depends both on the frequency and the microstrip length, and $\arg(S_{21}(f)) = \tan^{-1}(\text{Im}[S_{21}(f)]/\text{Re}[S_{21}(f)])$ is the argument of the exponent.

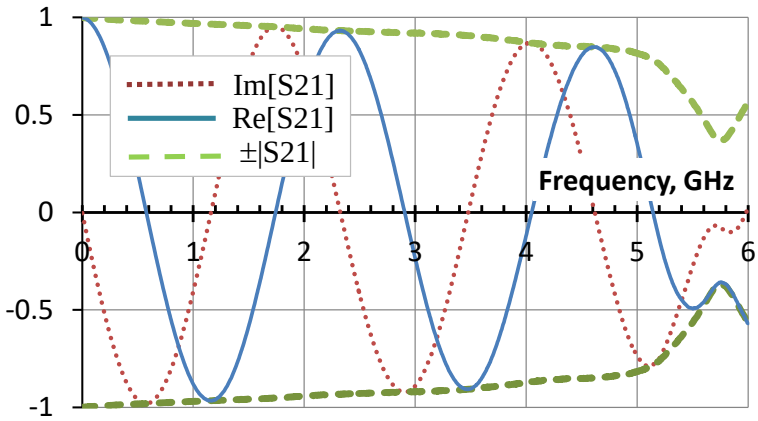

Fig. 4.4. Frequency dependencies of the real and imaginary parts of S_{21} (or S_{12}) of a continuous microstrip measured by a VNA, plotted in Microsoft Excel. Below 5 GHz, typical dispersion curves are observed, while above 5 GHz the microstrip has a resonance.

The time delay Δt and $A(f)$ in Eq. (4.16) can be found as:

$$\Delta t = -\frac{1}{2\pi f}\tan^{-1}\left(\frac{\mathrm{Im}[S_{21}(f)]}{\mathrm{Re}[S_{21}(f)]}\right) \tag{4.17}$$

$$A(f) = |S_{21}(f)| \tag{4.18}$$

Ideally, in Eq. (4.17) we should obtain a constant value for any frequency point. However, in practice Δt may vary, and hence an averaged value $\overline{\Delta t}$ has to be proposed. In the program code written in Fortran (Appendix B, see page 127-128), $\tan^{-1}(y/x) \in]-\pi, \pi[$ is calculated using the quadrant position of the point (x, y). The function $\tan^{-1}(y/x)$ has the jump (uncertainty) in the points (x, y) where $\tan^{-1}(y/x) = \pm\pi$. To obtain $\tan^{-1}(\mathrm{Im}[S_{22}(f)]/\mathrm{Re}[S_{22}(f)])$ as a monotonic function of f ("unwrapped argument"), the pieces of this function between the jumps is assembled into a continuous line by means of their vertical shifts by $2\pi n$, where n is the ordinal number of jump. To find the best approximation for Δt, first $\tan^{-1}(\mathrm{Im}[S_{22}(f)]/\mathrm{Re}[S_{22}(f)])$ is drawn as a monotonic function of f. Then, this function is fitted with a straight line $y(f) = af + b$ using the least-squares method, where b will be a very small number. Using this approximation, we find $\Delta t = |a|/2\pi$. The monotonous argument $\arg(f) = \arg[S(f)]$ as a function of the frequency shown in Fig. 4.5 was calculated for $S_{21}(f)$ from Fig. 4.4. Outside of the resonance region $5-6$ GHz, $\arg(f)$ is a perfect linear function of the frequency.

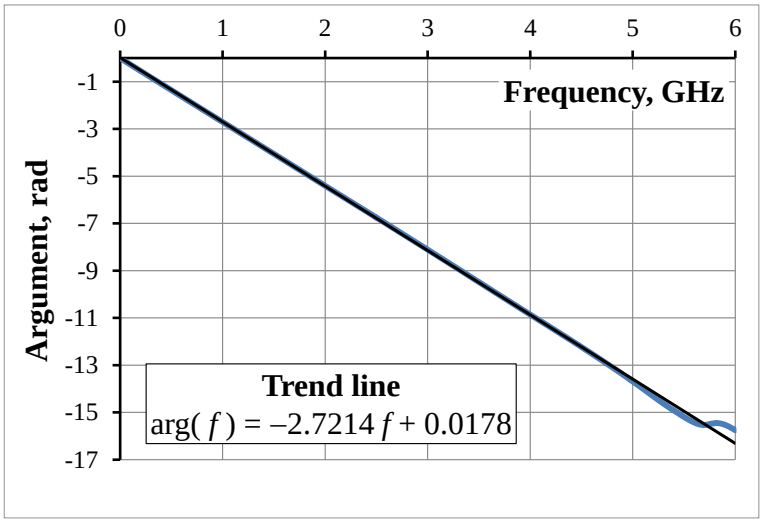

Fig. 4.5. Frequency dependence of the argument of $S_{21}(f)$. The linear dependence (black trend line) with a small vertical offset accurately describes $\arg(f)$ before 5 GHz.

In experiments of this chapter, the microstrips are used as the adapters that deliver signals from the coaxial SMA connectors to/from the microwire samples. Also, microstrips provide a technical space required to attach an extensometer or a strain gauge, or allow hot airflow to the wire sample. When measuring the S_{21}-parameter of a microwire through the supplier microstrips, the latter will introduce some phase and amplitude distortions as suggested by Fig. 4.4. If Δt and $A(f)$ of a particular microstrip are known, the distortions introduced by it can be effectively removed by the following normalisation (at least before the resonance):

$$S_{21}^{C}(f) = \frac{S_{21}^{M}(f)}{A(f) \times \exp(-j2\pi f \Delta t)} \tag{4.19}$$

where $S_{21}^{M}(f)$ is the dispersion of transmission coefficient measured through the microstrip and DUT, and $S_{21}^{C}(f)$ is the corrected dispersion as though the microstrip was virtually removed. Eq. (4.19) is the essence of the proposed calibration procedure. Using Eq. (4.19), we can factually neglect multiple reflections in the system, but the main impact (phase and amplitude distortions) will be taken into account. There is a much more accurate calibration procedure, called TRL (Thru-Reflection-Line) [4.3], [4.6], which could be in principle used for the cells. However, TRL requires measurement of all four S-parameters and transfer of a massive data to the computer that may be too long if we need to keep the same strain or temperature.

Keeping the same strain during a long time interval is especially problematic in the case of elastic materials such as a composite matrix. Examination of several bias magnetic fields will add even more time. Nevertheless, in the future the possibility of use of TRL with modern VNAs that provide much faster frequency sweep and data transfer should be investigated.

The resultant time delay of a microstrip (its two parts before and after the gap) used to measure $S_{21}(f)$ of a microwire was found by the destructive method explained in Fig. 4.6. The piece of PCB (without microstrip) constituting the gap was cut off, and then the obtained two parts were soldered together to measure the pure $S_{21}^{ms}(f)$ of the microstrip. It was checked that the joint in a microstrip does not introduce any significant distortions in the frequency range at least up to 6 GHz as shown in Fig. 4.7. Alternatively, the shortened microstrip made of the same PCB material could be used. After measuring $S_{21}^{ms}(f)$ of a particular microstrip, its time delay can be found using the algorithm based on Eq. (4.17) and the linearisation of the unwrapped argument of $S_{21}^{ms}(f)$ (see the program code attached in Appendix B).

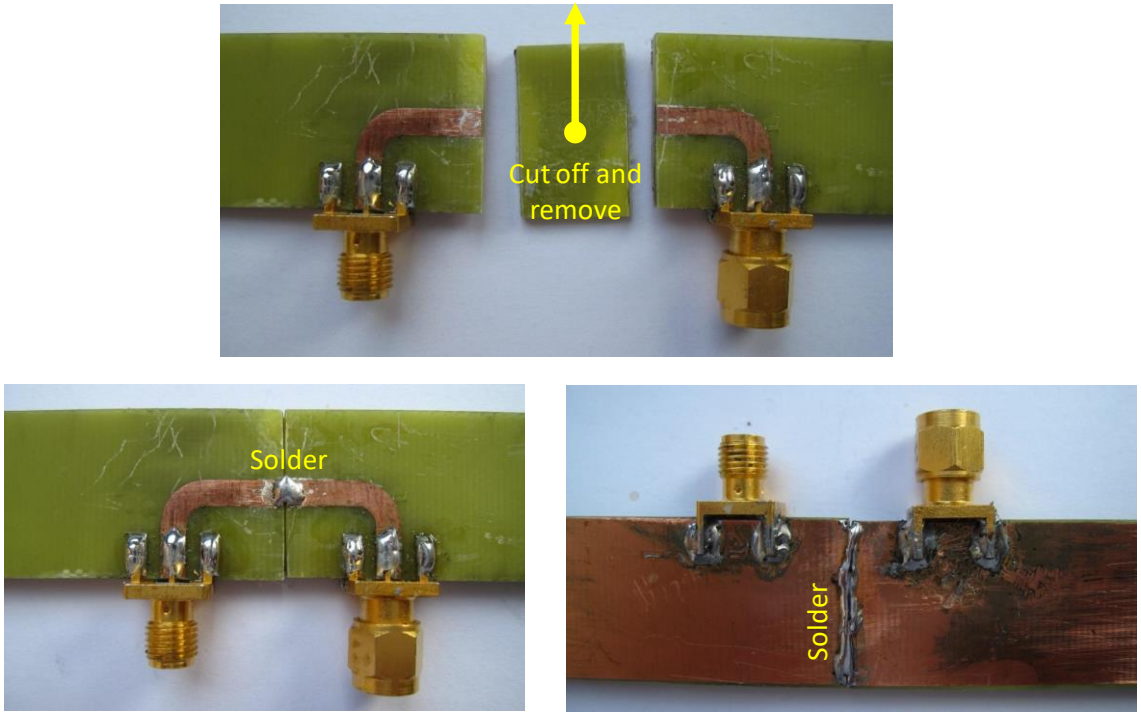

Fig. 4.6. The destructive method used for measuring the pure $S_{21}^{ms}(f)$ of the microstrip.

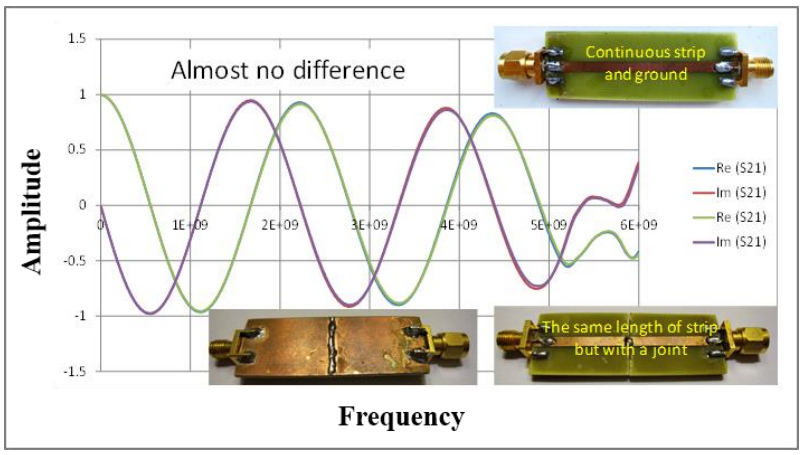

Fig. 4.7. A joint in the microstrip does not induce any significant distortions in the frequency range at least up to 6 GHz.

The accuracy of the obtained Δt of a microstrip can be checked by calculating $S_{21}^{ms}(f)/(A(f)\times\exp(-j2\pi f\Delta t))$: ideally, we should obtain the real unit and no imaginary part for the whole frequency range where $S_{21}^{ms}(f)$ was measured. However, in practice, a small imaginary part will present in the normalised $S_{21}^{ms}(f)$. To further optimise the value of Δt, a global optimisation based on the minimisation of the following functional $I(\Delta t)$ is proposed:

$$\min_{\Delta t} I(\Delta t) = \frac{1}{f_{stop} - f_{start}} \int_{f_{start}}^{f_{stop}} \left| \left| S_{21}^{ms}(f) \right| - \left| \mathrm{Re}\left[\frac{S_{21}^{ms}(f)}{\exp(-j2\pi f\Delta t)} \right] \right| \right| df \qquad (4.20)$$

where Δt is varied in a small vicinity of the initial approximation Δt_0 found from Eq. (4.17) and the linearisation of the unwrapped argument, $|\cdot|$ means the modulus and $[f_{start}, f_{stop}]$ is the full frequency range before the resonance frequency (< 5 GHz). In the algorithm written in Fortran (Appendix C, see page 129), the integration in Eq. (4.20) was carried out using a simple trapezium method. The global minimum of the functional was found by the enumeration of $I(\Delta t_a)$ in discrete points within $\Delta t \in [\Delta t_0 - \text{error}, \Delta t_0 + \text{error}]$. Error $= 5 - 10$ ps and 10000 time points is used.

Using the destructive method in Fig. 4.6 and the algorithms for Eqs. (4.17),(4.20), the delay times for the three dog bone cells used in the stress-impedance measurements were found (see Fig. 4.8). Note that

while the cells 2 and 3 are made of the same thickness, they have somewhat different time delays. The time uncertainty of ~ 9 ps corresponds to the spatial uncertainty of ~ 1.4 mm on a FR4 PCB (calculated for the velocity factor 0.53). Such difference might be produced by the collective inaccuracy in the cut and the soldering of the SMA connectors. In any case, 9 ps will produce just ~ 0.34 rad of the phase uncertainty at 6 GHz. The straight cell used for the temperature-impedance measurements and its time delay are shown in Fig. 4.9.

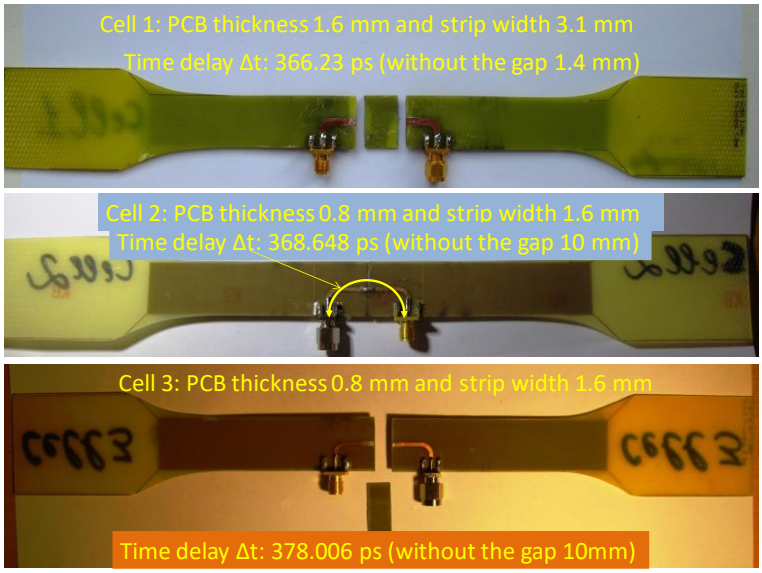

Fig. 4.8. The time delays found for the three dog bone cells used in the stress-impedance measurements. The destructive method and the algorithms for Eqs. (4.17),(4.20) were used to find the microstrip time delay.

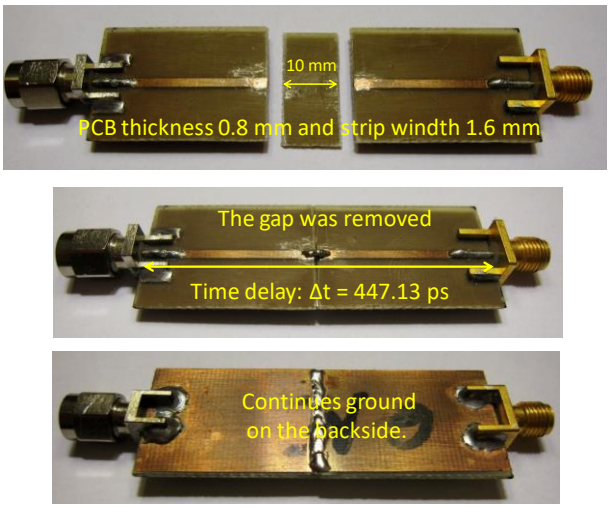

Fig. 4.9. The straight cell used for the temperature-impedance measurements inside of the heat chamber shown in Fig. 3.14. The destructive method and the algorithms for Eqs. (4.17),(4.20) were used to find the microstrip time delay.

The stress-impedance measurements were organised into the database shown in Fig. 4.10. The database contains files with the dispersion of $S_{21}(f)$ measured in a wide frequency range for a particular strain and bias field. Then, each $S_{21}(f)$ was corrected (calibrated) using normalisation in Eq. (4.19) with $A(f)$ and Δt for a particular cell (see Fig. 4.8).

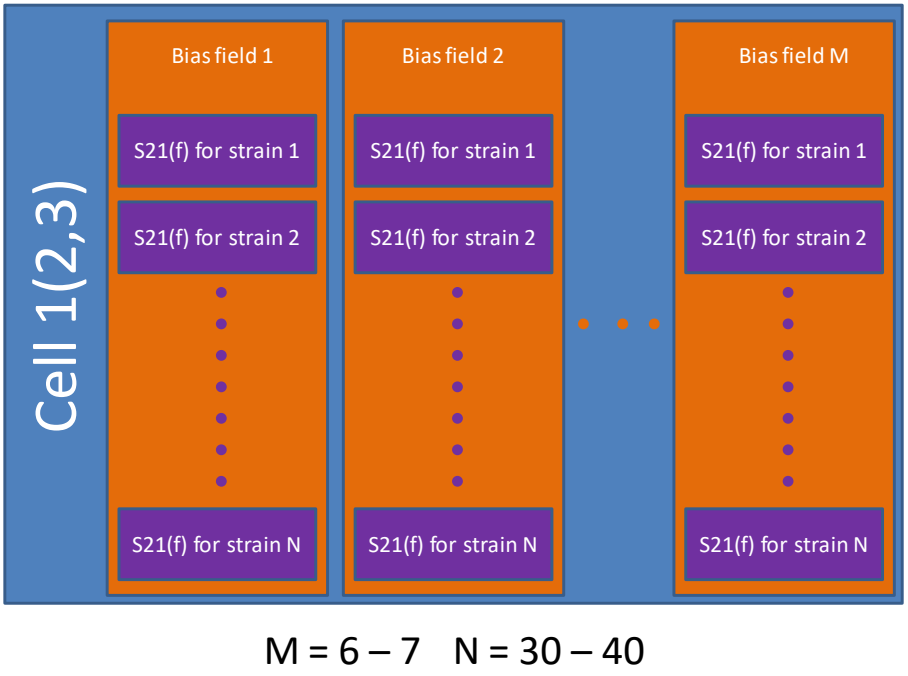

Fig. 4.10. The structure of database for the stress-impedance measurements.

Fig. 4.11 shows a non-corrected dispersion of $S_{21}^{M}(f)$, measured through a microwire for zero stress and bias field, and the corrected dispersion $S_{21}^{C}(f)$ obtained from $S_{21}^{M}(f)$ by applying the normalisation in Eq. (4.19). The effect of normalisation is remarkable. Comparison of the non-corrected and corrected curves also indicates that the wave propagation effects will manifest themselves starting from ~ 60 MHz. The latter explains the importance of cell calibration even for the higher MHz frequencies.

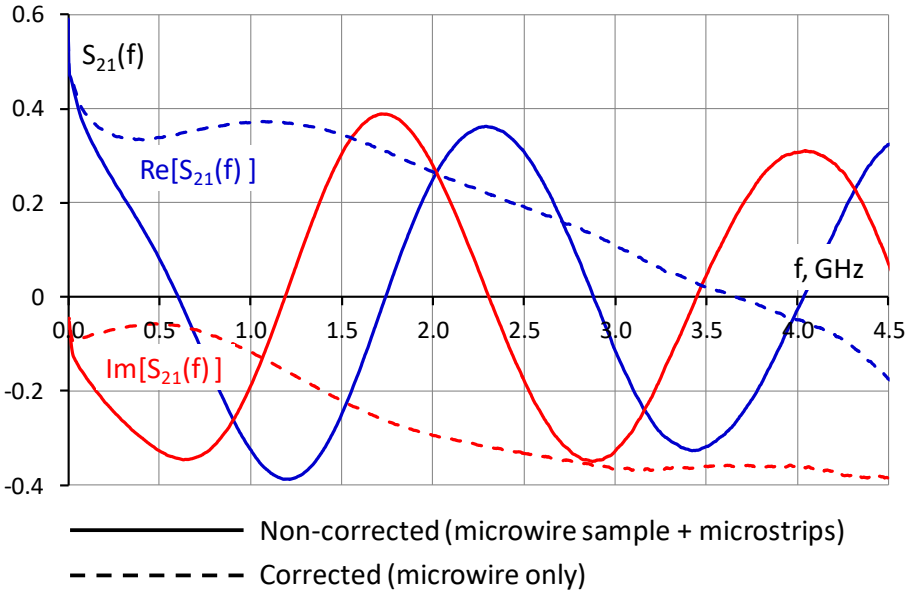

Fig. 4.11. A non-corrected dispersion of $S_{21}^{M}(f)$ (solid curves), measured through a microwire for zero stress and bias field, and the corrected dispersion $S_{21}^{C}(f)$ (dashed curves), obtained from $S_{21}^{M}(f)$ by applying the normalisation in Eq. (4.19).

4.3. Calculation of the impedance and the surface impedance from the transmission coefficient

The microwire impedance $Z(f)$ will be calculated from $S_{21}^{C}(f)$ using Eq. (4.13). In turn, $Z(f)$ is the sum of the internal impedance $Z_{int}(f)$ and the external impedance $Z_{ext}(f) = j\omega L_{ext} l$, which is determined by the external inductance per unit length L_{ext} (H/m) of a wire placed above the ground [4.7]:

$$L_{ext} = \frac{\mu_0}{2\pi} \ln\left(\frac{h}{a} + \sqrt{\left(\frac{h}{a}\right)^2 - 1} \right) \approx \frac{\mu_0}{2\pi} \ln\left(\frac{2h}{a}\right) \qquad (4.21)$$

where h is the PCB thickness above the ground, $a << h$ is the wire radius, $\mu_0 = 4\pi \times 10^{-7}$ H/m is magnetic constant. Then, the surface impedance can be calculated from $Z_{int}(f)/l$:

$$\begin{cases} \zeta_{zz}^{\mathrm{SI}}(f) = 2\pi a \times \dfrac{Z_{int}(f)}{l} \\ \zeta_{zz}^{\mathrm{cgs}}(f) = \dfrac{10^9 a}{2c} \times \dfrac{Z_{int}(f)}{l} \\ \dfrac{Z_{int}(f)}{l} = \dfrac{Z(f)}{l} - j\omega L_{ext} \\ Z(f) = Z_0 \times \dfrac{2(1 - S_{21}^C(f))}{S_{21}^C(f)} \end{cases} \tag{4.22}$$

As it has been mentioned earlier in this chapter, for a microwire of length 1 cm, Eq. (4.13) will be most accurate for the frequencies below 2.5 GHz. For higher frequencies, it will give an increasingly deteriorating approximation to $Z(f)$. To expand Eq. (4.13) well beyond 2.5 GHz, the length of microwire must be reduced. It is definitely not easy, but still possible to prepare a glass-coated microwire sample of a few millimetres length with the trimmed ends.

As an alternative approach, we could try to derive the linear impedance $Z(f)/l$ from the parameter γ in Eq. (4.7):

$$\gamma(f) = \sqrt{\left(\frac{Z_{int}(f)}{l} + j2\pi f L_{ext}\right)(G(f) + j2\pi f C)} \tag{4.23}$$

Here, C is the wire linear capacitance above the ground [4.7],[4.8]:

$$C_w = \frac{2\pi\varepsilon_0\varepsilon_{eff}}{\ln\left(\dfrac{h}{a} + \sqrt{\left(\dfrac{h}{a}\right)^2 - 1}\right)} \approx \frac{2\pi\varepsilon_0\varepsilon_{eff}}{\ln\left(\dfrac{2h}{a}\right)} \tag{4.24}$$

$$\varepsilon_{eff} = \frac{\ln(2) + \ln\left(1 + \dfrac{h}{a}\right)}{\ln(2) + \ln\left(1 + \dfrac{h}{a\varepsilon}\right)} \tag{4.25}$$

where ε is the dielectric constant of PCB and $\varepsilon_0 = 8.85 \times 10^{-12}$ F/m is the vacuum permittivity. The parameter γ can be calculated from the corrected $S_{21}^C(f)$ that coincides with the microwire propagation coefficient:

$$\begin{cases} S_{21}^{C}(f) = \exp(-\gamma(f)l) = \exp(-\mathrm{Re}[\gamma(f)]l) \times \exp(-j\,\mathrm{Im}[\gamma(f)]l) \\ \mathrm{Re}[\gamma(f)] = -\dfrac{\ln|S_{21}^{C}(f)|}{l} \\ \mathrm{Im}[\gamma(f)] = -\dfrac{\arg(S_{21}^{C}(f))}{l} \end{cases} \tag{4.26}$$

The argument of $S_{21}^{C}(f)$ in Eq. (4.26) must be unwrapped as it has been explained for Eq. (4.17). Using Eq. (4.23) and assuming $G(f) << 2\pi f C$, we obtain:

$$\frac{Z_{int}(f)}{l} = -\frac{j\gamma^2(f)}{2\pi f C} - j2\pi f L_{ext} \tag{4.27}$$

Unfortunately, Eq. (4.27) gives unrealistic results, especially for lower frequencies. So, some type of modification is required in the wave propagation analysis. Most probably, the dissipation factor in FR4 dielectric cannot be neglected anymore, and hence the condition $G(f) << 2\pi f C$ is violated.

For calculation of the surface impedance, Eq. (4.22) will be used which remains quite accurate even for higher frequencies if the length of microwire will be reduced. Fig. 4.12 shows a typical dispersion of the surface impedance $\zeta_{zz}^{\mathrm{cgs}}(f)$ calculated from the corrected $S_{21}^{C}(f)$ in Fig. 4.11. The length of microwire and its metal core radius were $l \sim 14$ mm and $a \sim 12.7$ μm respectively. The maximum frequency at which Eq. (4.22) remains most accurate for this particular microwire can be estimated from Eqs. (4.15) and (4.25): $f_{\max} \sim 1.8$ GHz for a 1.6 mm PCB. Since $\mathrm{Re}[\zeta_{zz}^{\mathrm{cgs}}(f)]$ must be positive [4.2], the dispersion curves beyond ~ 2.75 GHz are definitely incorrect. Between these two limits (1.8 and 2.75 GHz) there is an uncertain transition area. According to Eq. (4.15), $f_{\max}$ can be increased by removing the dielectric substrate under the microwire (within the gap between the microstrips), while retaining the ground. A possible cell design is shown in Fig. 4.13, where a narrow movable substrate in the air gap is used only for fixing the microwire and then removed. Such design with the air gap of 0.5 cm will guarantee $f_{\max} \sim 6$ GHz that entirely covers the frequency range used for tuneable composites with ferromagnetic microwire inclusions. Also, the absence of dielectric under the microwire disposes of the difficulty of taking into account its dielectric losses, and hence $G(f) \equiv 0$ in Eq. (4.23). That might reanimate the wave approach (4.27).

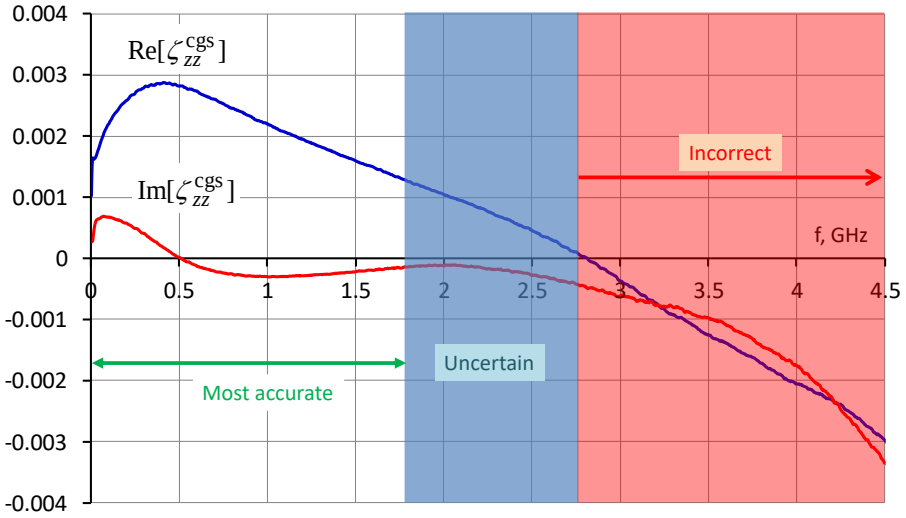

Fig. 4.12. A typical dispersion of the surface impedance $\zeta_{zz}^{cgs}(f)$ calculated from the corrected $S_{21}^{C}(f)$ in Fig. 4.11 by means of the method (4.22). The length of microwire and its metal core radius were $l \sim 14$ mm and $a \sim 12.7$ μm respectively. The two shadowed areas indicate the frequency intervals where the reconstruction of $\zeta_{zz}^{cgs}(f)$ is less certain or even incorrect.

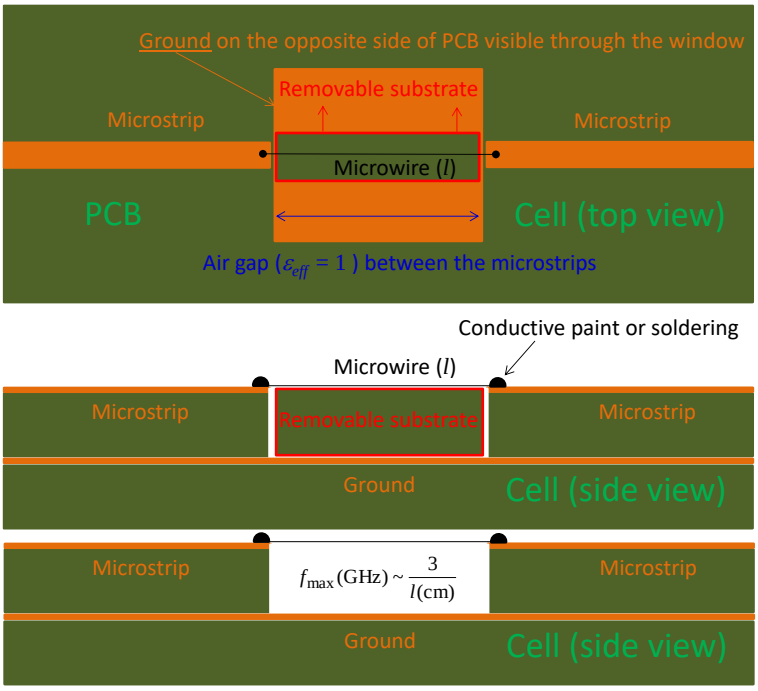

Fig. 4.13. A cell design which, according to Eq. (4.15), allows a higher maximum frequency.

The high frequency dispersion $\zeta_{zz}(f)$ obtained in the frame of the impedance model (2.7)-(2.8) provides a qualitative agreement with the experimental dispersion curves recovered by means of the method (4.22) for microwires with circumferential anisotropy. Note that when comparing with experiments, the sign of the theoretical $\mathrm{Im}[\zeta_{zz}(f)]$ must be changed because $\zeta_{zz}(f)$ in Eqs. (2.7)-(2.8) was derived for the time dependence $\sim \exp(-j\omega t)$. In Fig. 4.14, the model dispersion was calculated in the approximation of strong skin-effect (2.8) for a microwire that emulates the parameters of the real microwire already used in Chapter II and Figs. 4.11 and 4.12 (see also Fig. 4.15): the radius of metal core $a = 12.65 \times 10^{-4}$ cm, the resistivity $\rho = 2.56 \times 10^{-16}$ s (Gaussian-cgs), and the anisotropy field $H_K \sim 2$ Oe. The other parameters used for the modelling were the gyromagnetic ratio $\gamma = 1.8 \cdot 10^7$ rad×s^{-1}×Oe^{-1} (Gaussian-cgs) and the spin-relaxation parameter $\tau = 0.1$. Both the model and experimental dispersion curves were obtained for zero strain and in the presence of a bias magnetic field $H_{ex} = 3$ Oe. In the model, the maximum of $\mathrm{Re}[\zeta_{zz}(f)]$ and zero of $\mathrm{Im}[\zeta_{zz}(f)]$ are shifted towards lower frequencies as compared with the experimental dispersion. The frequency interval before 1 GHz, which is most sensitive to the features of magnetic structure, will be always less predictive for a model relying on simplifications. On the contrary, for higher GHz frequencies, where AC magnetic properties quickly decay and a microwire becomes simply a conductive cylinder, the impedance model regains its reliability, while the method (4.22) suffers from the non-locality of impedance due to the wave effects in the sample. In other respects, the model and experimental dispersions are very similar. That gives hope that with improved cell design, more accurate calibration (see Chapter V) and shorter samples, reliable experimental dispersions up to several Gigahertz can be obtained.

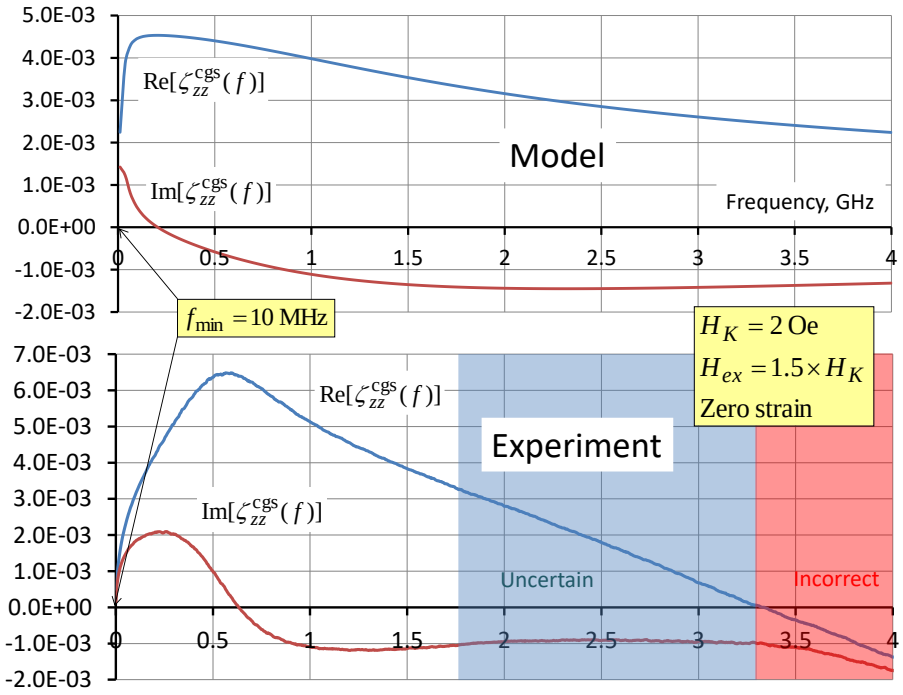

Fig. 4.14. Comparison of the model and experimental dispersion curves obtained in the presence of a bias magnetic field $H_{ex}=3$ Oe. In the experiment, the microwire had the length of ~ 14 mm.

4.4. The effect of strain on the surface impedance

Figs. 4.15 and 4.16 demonstrate the effect of stain on $|\zeta_{zz}^{cgs}|$ which was recovered by means of the method (4.22) from the database of $S_{21}(f)$ explained in Fig. 4.10. The strain dependencies of $|\zeta_{zz}^{cgs}|$ were obtained for two Co-based microwires ("thick" and "thin") at fixed frequencies and in the presence of different bias magnetic fields. As compared with the strain-impedance curves in Fig. 2.8, for higher frequencies (especially for ≥2 GHz) we will have a more pronounced tunability. By applying a stronger bias magnetic field $H_{ex} > H_K$, the stress sensitive region is shifted towards a higher strain. The thinner microwire in Fig. 4.15 had a larger anisotropy field $H_K \sim 4$ Oe.

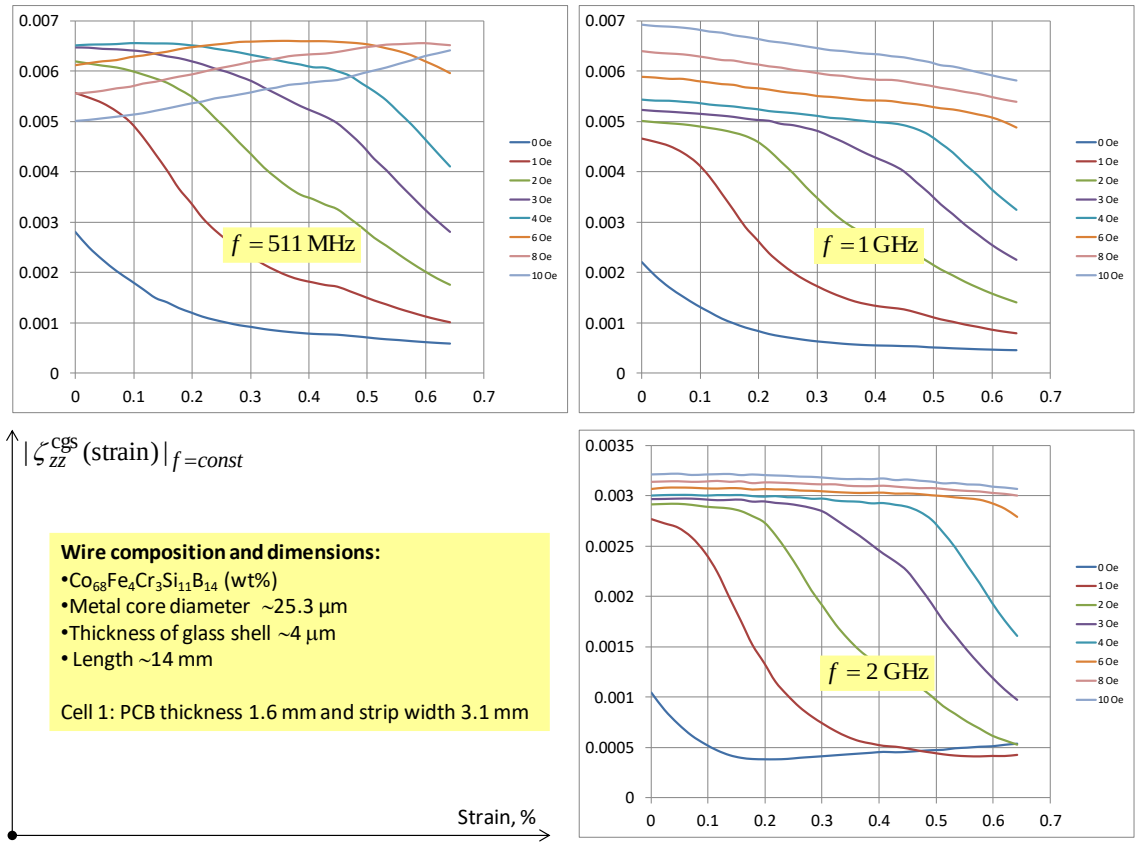

Fig. 4.15. The strain dependencies of $|\zeta_{zz}^{cgs}|$ at fixed frequencies and in the presence of different bias magnetic fields ($0-10$ Oe) recovered by means of the method (4.22) from the $S_{21}(f)$ measured through the microwire already used in Chapter II and Figs. 4.11, 4.12.

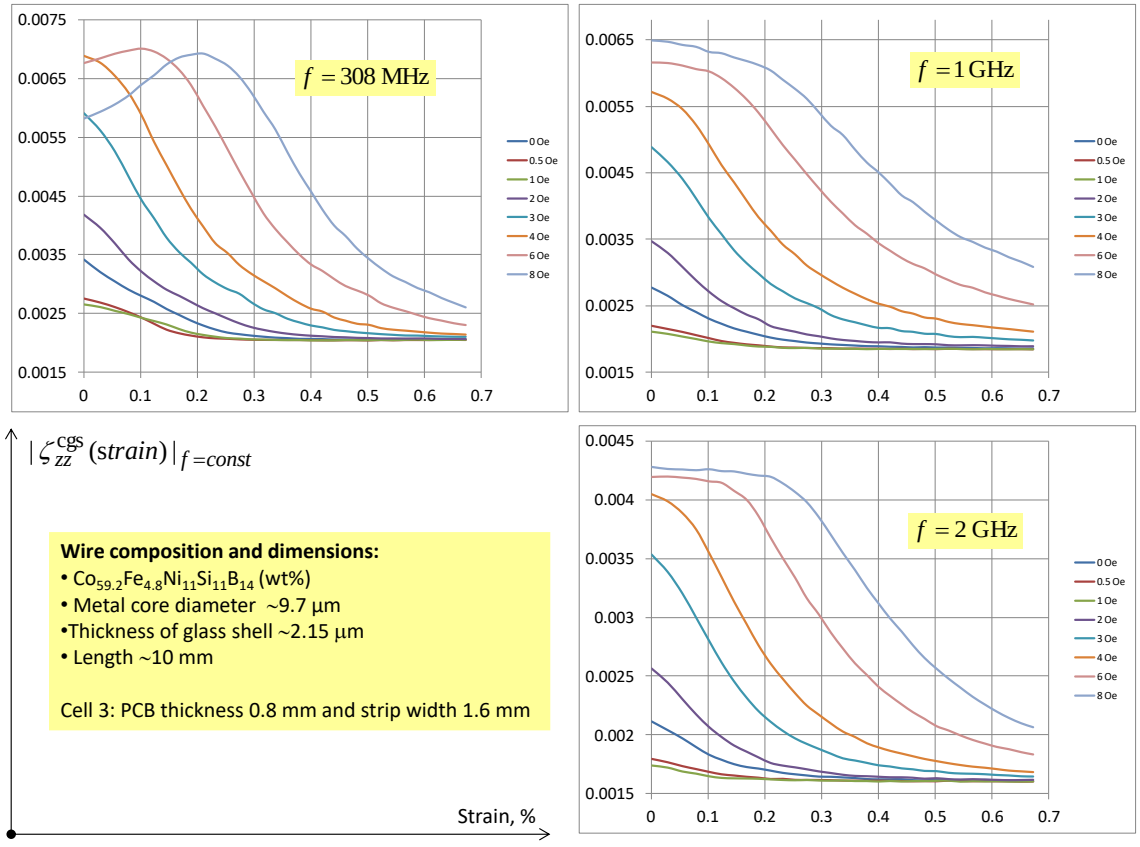

Fig. 4.16. The strain dependencies of $|\zeta_{zz}^{cgs}|$ at fixed frequencies and in the presence of different bias magnetic fields ($0-8$ Oe) recovered by means of the method (4.22) from the $S_{21}(f)$ measured through a very thin microwire having a higher anisotropy field ~ 4 Oe.

In the first theoretical work [4.1] on tuneable microwave composites, it has been shown that the magneto-impedance at the Gigahertz frequencies will demonstrate the so-called "valve-like" behaviour when $|\zeta_{zz}(H_{ex})|$ monotonically increases with $|H_{ex}| < H_K$ and then remains almost constant for $|H_{ex}| > H_K$ as shown in Fig. 4.17 (model). Since H_K is proportional to the external tensile stress (see Eqs. (2.3) and (2.5)), $|\zeta_{zz}(H_{ex})|$ will become wider when applying strain. The "valve-like" impedance explains the strain dependencies of $|\zeta_{zz}|$ observed in Gigahertz experiments. For $|H_{ex}| \sim H_K$ at zero strain, $|\zeta_{zz}|$ monotonically decreases when applying strain. Such behaviour corresponds to $H_{ex} = 1$ Oe in Fig. 4.17, where the model H_K reduced to 1 Oe to fit the start of monotonous decrease. For higher $H_{ex} > 1$ Oe, when applying strain, $|\zeta_{zz}|$ will demonstrate just a small decrease until H_K as a function of strain reaches H_{ex}. After that, a monotonous decrease occurs again.

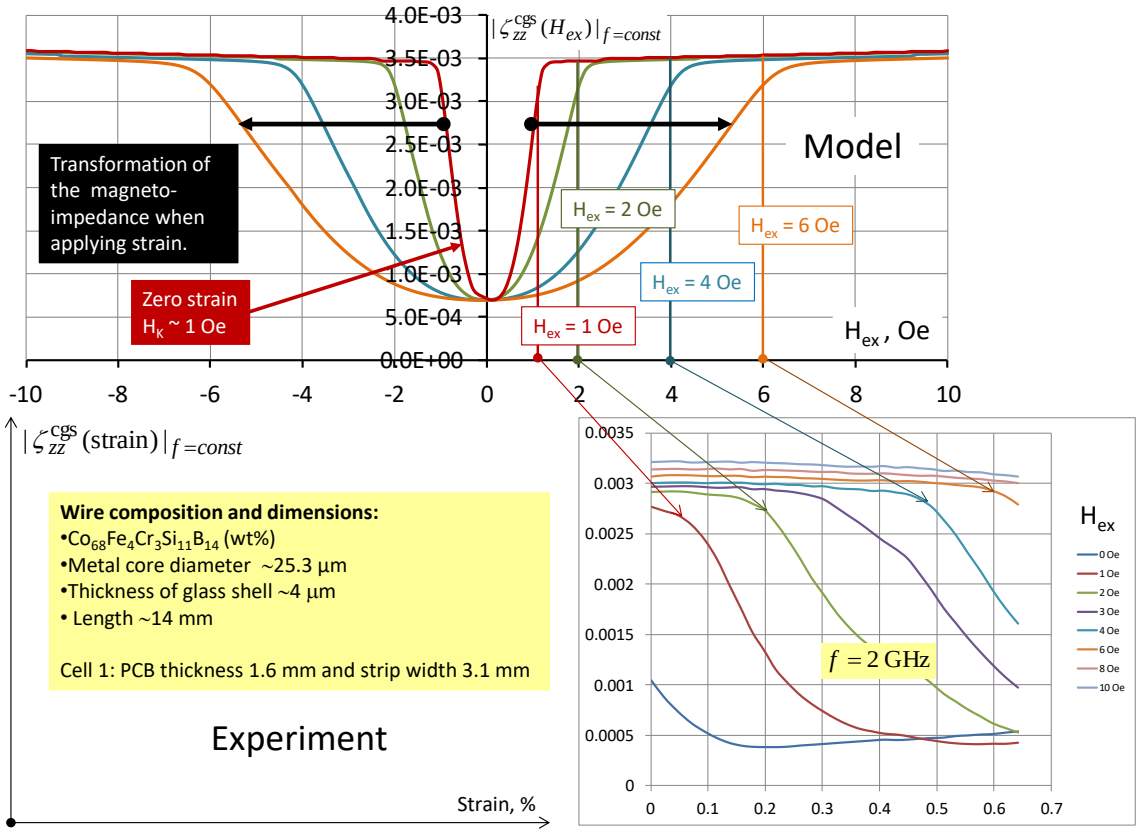

Fig. 4.17. The "valve-like" magneto-impedance explaining the strain dependencies of $|\zeta_{zz}|$ in GHz frequencies.

4.5. The effect of temperature on the surface impedance

Investigations of the effect of temperature on the surface impedance are in their infancy. Currently, temperature control that might allow for drawing smooth temperature dependencies of the surface impedance does not exist. However, the experimental setup for temperature measurements developed in Chapter III (see Figs. 3.14 and 3.15) is an important step forward. In the future, it will be modified to precisely control the temperature and intensity of the air flow blowing over a microwire sample placed onto the PCB cell.

For experiments, microwires made of alloys having a low Curie temperature (low-T_C microwires) that can be varied in a wide range starting from room temperature depending on the alloy composition [4.9-4.10] were chosen. For example, the microwire sample with the composition $Fe_{3.9}Co_{64.52}B_{10.2}Si_{12}Cr_{9.3}Mo_{0.08}$ (wt%), provided by MFTI Ltd (Alloy №1969 in the company catalogue), had $T_C \sim 72.8$ °C. With such microwires, it becomes possible to demonstrate a strong Temperature Trigger Effect (TTE) when magnetic

properties are “switched off” by heating much earlier than it would affect the magneto-elastic anisotropy. That disposes of the difficulty of developing precise temperature control.

Fig. 4.18 demonstrates the effect of temperature on the magneto-impedance $|\zeta_{zz}^{cgs}(H_{ex})|$ at four frequencies revealing its transformation through the spectrum. For experiments, a low-T_C microwire already mentioned above (Alloy №1969) with the diameter of magnetic core ~ 18 μm are used. Only TTE was checked when the magnetism is switched off by blowing the microwire with a hot air jet (a hairdryer would be enough). The magneto-impedance was recovered by means of the method (4.22) from $S_{21}(H_{ex})$ measured using the fixtures in Figs. 3.14 and 3.15 and the cell in Fig. 4.9. The characteristic bell shape of $|\zeta_{zz}^{cgs}(H_{ex})|$ at 100 MHz and room temperature indicates that the microwire has a longitudinal anisotropy. The hysteresis is almost negligible. A heat above T_C completely flattens $|\zeta_{zz}^{cgs}(H_{ex})|$. The maximum TTE is observed in zero field. For higher frequencies, the minimum in zero field and the two maxima for non-zero ($\pm$) fields are gradually forming. For such frequencies, the maximum TTE will always be observed for non-zero fields, i.e. a bias field enhancement takes place. In the vicinity of 730 MHz, the curves will rise to their maximum level for any fields. With further increase of the frequency, the positions of maxima of $|\zeta_{zz}^{cgs}(H_{ex})|$ shift towards larger fields, while the curves as a whole sink down and TTE decreases. Using dispersion curves (see Fig. 4.19), the frequencies at which the maximum TTE is observed can be found. The curves by themselves are similar to those in Fig. 4.14 obtained for a microwire with a circumferential anisotropy.

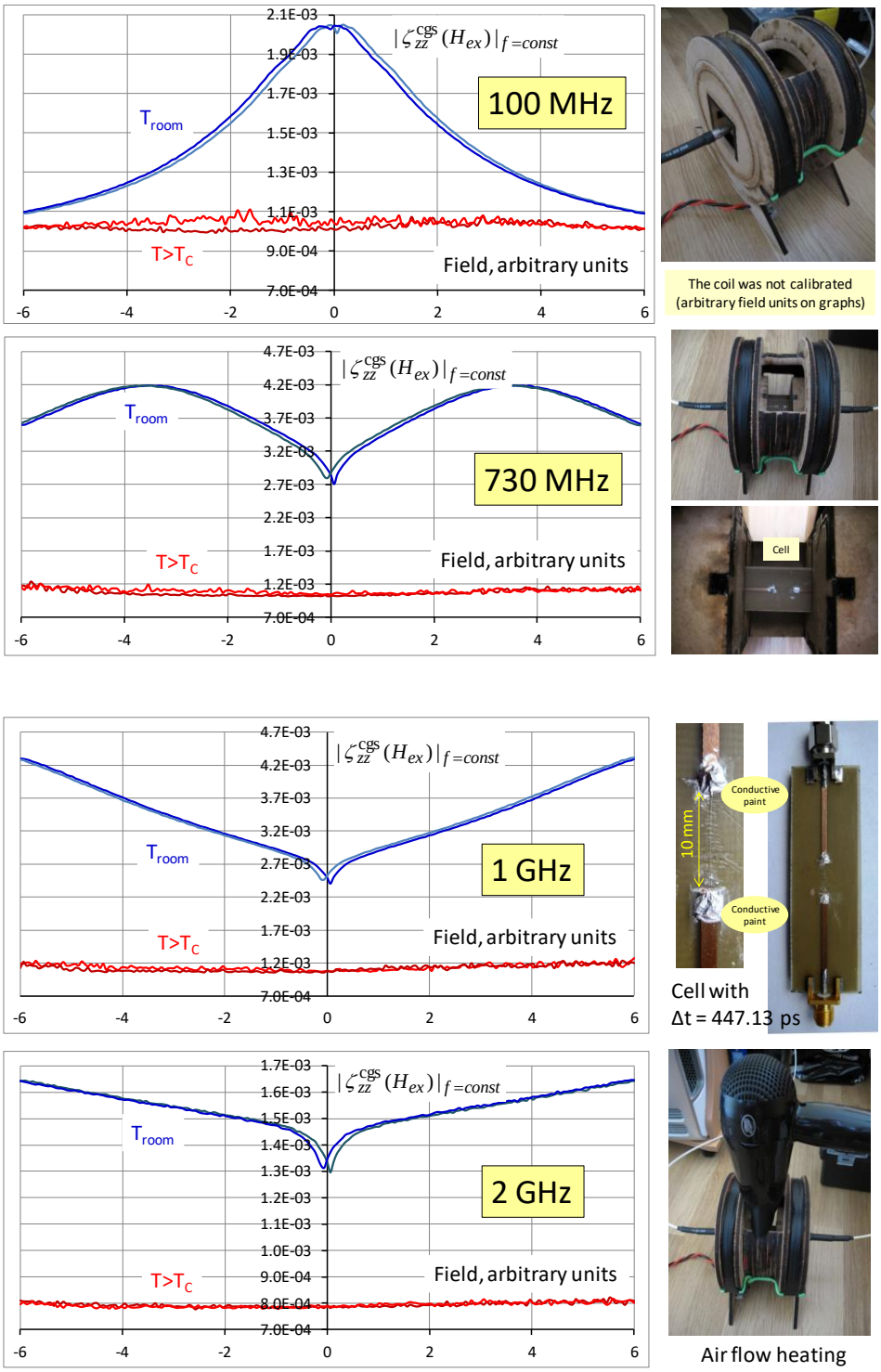

Fig. 4.18. The experimental magneto-impedance $|\zeta_{zz}^{cgs}(H_{ex})|$ obtained for a low-T_C microwire at four frequencies and two temperatures: room temperature and above T_C. The hysteresis is shown (very weak). The Helmholtz coil was not calibrated.

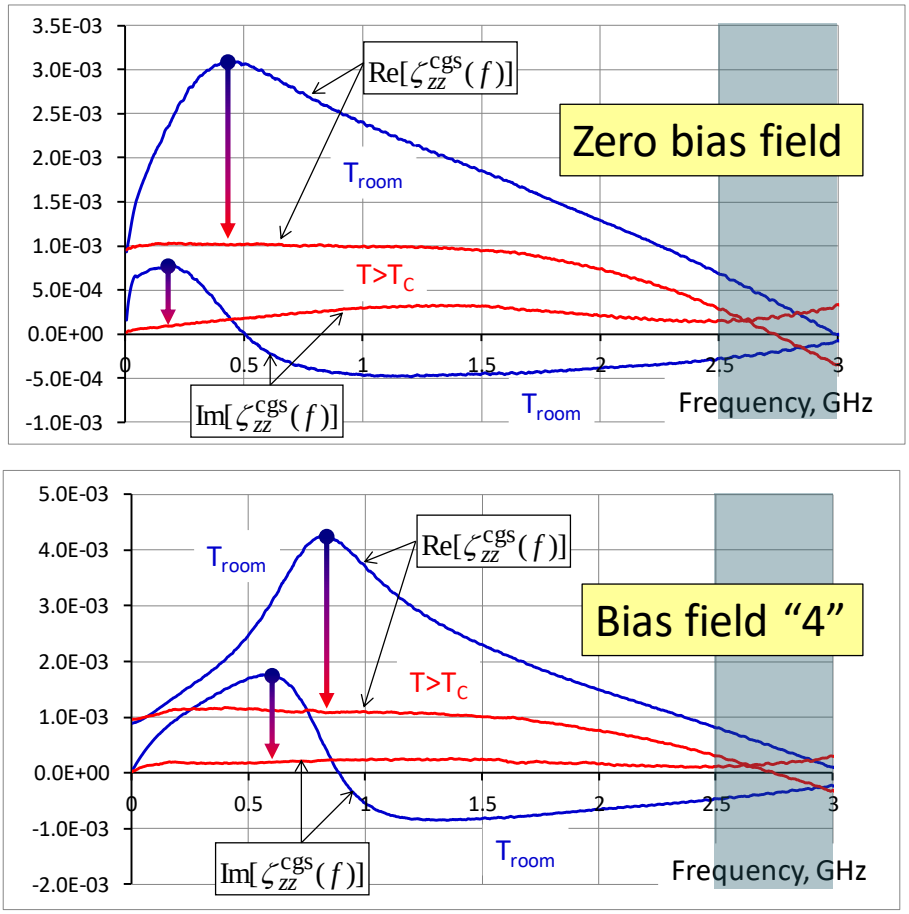

Fig. 4.19. The experimental dispersions of $\zeta_{zz}^{cgs}(H_{ex})$ obtained for a low-T_C microwire at two bias fields and two temperatures: room and above T_C. The Helmholtz coil was not calibrated. Bias field "4" corresponds to Field 4 in Fig. 4.18.

4.6. Next step forward: enabling free space measurements

The methods developed in this chapter for measurements of high frequency impedance properties in the presence of external stimuli allow to fully characterise the surface impedance of microwires. This parameter can be used for modelling microwave scattering properties of composite materials filled with microwire inclusions [4.11]. For experimental study of such properties, a free space measurement setup has to be designed and built – an even more challenging task than development of the contact test fixtures in Chapter III. In this project, it is not intended to elaborate all technical aspects of such a complex system. Nevertheless, a number of ideas that could inspire further experimental research in this area could be stated.

To study microwave properties of composite materials in the presence of a high temperature, a large heat chamber will be required. It must be equipped with the microwave transparent windows made of

a heat resistant dielectric, a cooling system for the internal walls, and an automatic temperature control. Also, the chamber should enable two additional stimuli to be applied to a plane composite sample: external tensile stress and DC magnetic field. A possible design of such chamber is shown in Fig. 4.20. The interior of the chamber must be coated with a heat resistant microwave absorber that must be able to withstand the service temperature 200 °C and a short temperature rise up to 260 °C (both without cooling). The wall can be cooled by oil cooling with the forced circulation. The chamber will occupy the whole width of a test machine (between its posts) to allow larger microwave windows, say 800 mm × 800 mm. With increase of the frequency, the radiation spot produced on the window surface by the main lobe of a horn antenna will become smaller and smaller, thereby reducing diffraction effects from the window edges. For example, the broadband horn antenna П6-23М ($0.85-17.44$ GHz) [4.12] shown in Fig. 4.21 has the diameter of radiation spot $\sim 0.96\times L$ for 0.85 GHz (35 cm wavelength) and $\sim 0.09\times L$ for 17.44 GHz (1.72 cm wavelength), where L is the distance from the antenna. To guarantee a nearly plane wave front in the radiation near-field region, several wavelengths must be allowed between the antenna and the composite sheet, say 1 m for the whole frequency range $0.85-17.44$ GHz.

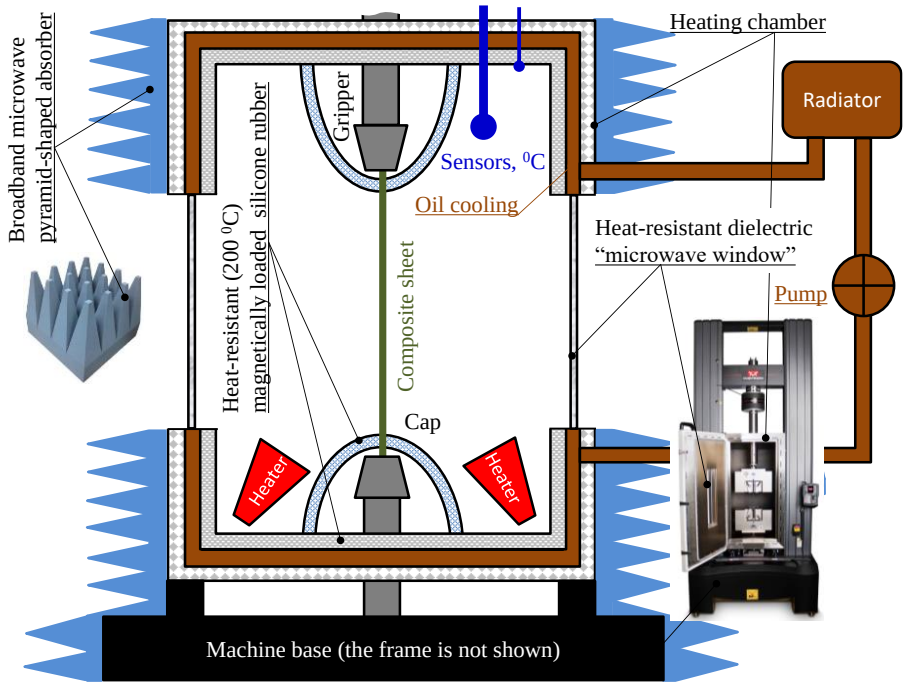

Fig. 4.20. A possible design of the heat chamber enabling free space microwave measurements from flat composite samples subjected to different stimuli: heat, strain, and magnetic field.

Fig. 4.21. The broadband horn antenna П6-23М ($0.85-17.44$ GHz).

A uniform DC magnetic field along the sample surface can be induced by the special planar coil proposed in Ref. [4.11] and shown in Fig. 4.22. Such a coil will not disturb an incident electromagnetic wave if its electric vector is directed perpendicular to the turns. Since the horn antennae have a linear polarisation, this condition is easily provided. Slightly changing the coil design, a uniform magnetic field can be obtained at the exterior sides of the coil. To do this, the current in all turns must flow in the same direction (the field inside the coil will be reduced). Such coil can be made flexible and applied to a curved surface. In this case, a composite sample needs not to be placed inside of the coil what is very important for NDT applications.

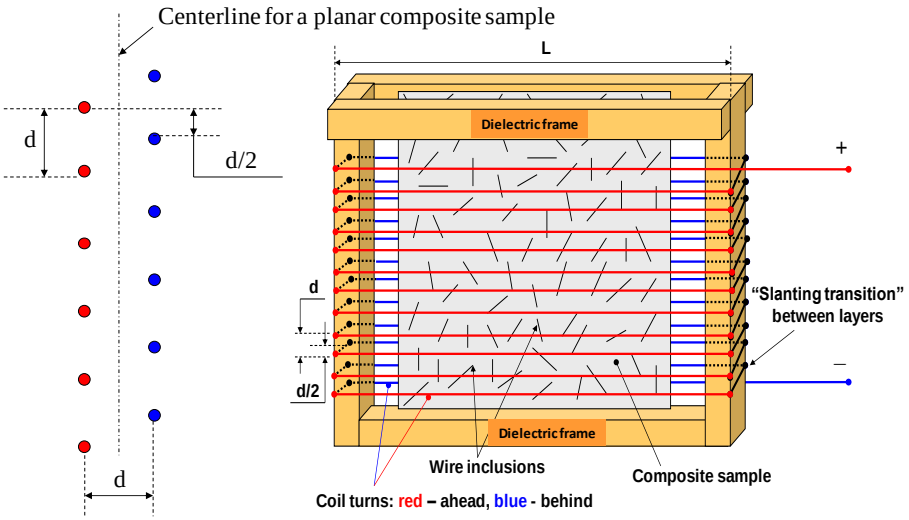

Fig. 4.22. The planar magnetic coil providing a highly uniform magnetic field along a large flat composite sample.

4.7. Final thoughts

Although NDT methods have long been used to examine structures made from traditional materials such as metals and plastics, NDT of composites have lagged far behind in comparison to the advancements in composite materials. Newer materials used in composites, together with complex purpose-specific geometries consisting of radical shapes, contours, curves and sharp radii, along with complexity of potential faults, present new challenges during their examination. Complex structures are being manufactured on an industrial-scale such as wind turbines, aircrafts, boats, cars and even bicycle frames that are no longer a simple "flat" or a "cylindrical" shape. As a result, it is becoming more and more challenging to examine composite structures. Even though new technologies are being developed, the NDT community is relatively small in comparison to designers and manufacturers of composite material products. During the visit to the 10th European Trade Fair & Forum for Composites, Stuttgart, Germany (22-24 September 2015), there were hundreds of companies presenting very unique composite products and technologies. However, there were only a handful of companies involved with NDT. One of the companies involved in NDT of composites at this exhibition were iNDTact GmbH (www.indtact.de) demonstrating real-time structural-health monitoring acoustic-emission and dynamic-load sensors (see Fig. 4.23) Another company present at this expo was SONOTEC Ultraschallsensorik Halle GmbH (www.sonotec.eu) which demonstrated many of their ultrasonic testing products for use in testing and analysis of plastics and composites (see Fig. 4.24). As the use of composites in the future increases, more efforts would be needed in the field of NDT together with the creation and use of newer technologies and methods to keep up with the demand to examine composites structures. Ultrasonic testing (UT) and infrared thermography (IRT) are currently the leaders in NDT of composites if sensor inclusions are not embedded into the composite matrix. However, in the future, embedded micro/nano sensors may solve some specific NDT problems described previously and provide an enhanced way to monitor and test the structural health of composites.

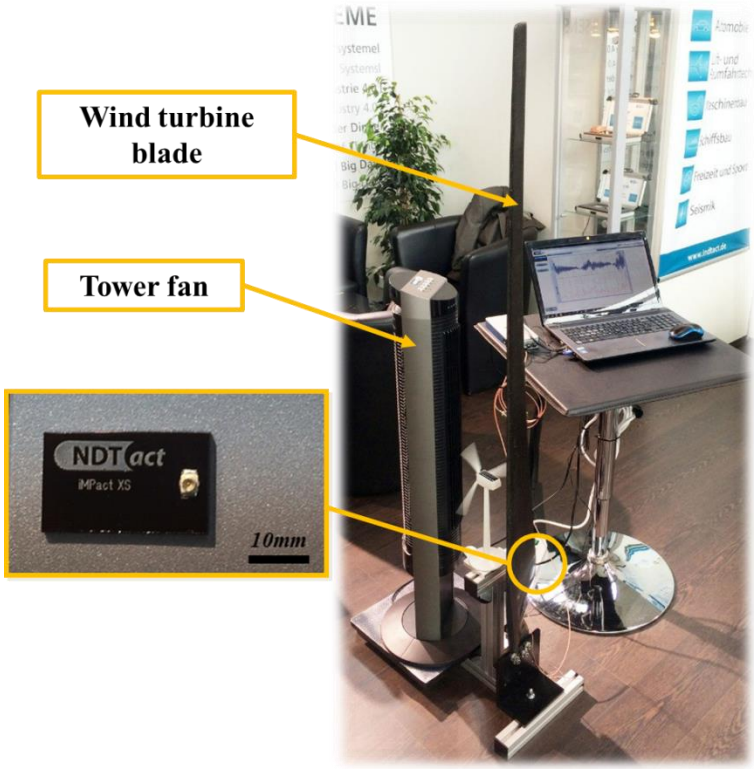

Fig. 4.23. iNDTact "iMPactXS" high-performance acoustic-emission and dynamic-load sensor glued on the surface of a wind turbine blade to demonstrate real-time structural-health monitoring, with effects of change in wind speed and wind direction (created by a tower fan) displayed on the laptop screen.

Fig. 4.24. SONOTEC SONOSCREEN ST10, a compact ultrasonic flaw detector, together with several transducers for use in NDT of plastics and composites, demonstrating structural defect on the surface of a plastic structure.

Recently, BAE Systems UK has launched an ambitious research project on Smart Skin [4.13], the key aspects of which are summarised in Fig. 4.25. Numerous announcements in the press unfortunately provide no opportunity to assess the degree of advancement of the project and what are its main technical solutions. Anyway, a much respected company has voiced the trend which was in the air, and now probably will be the priority research subject for many laboratories involved in the study of smart materials. It would be great for the team involved in this current research project to participate in this fascinating research topic with original ideas and unique measurement techniques.

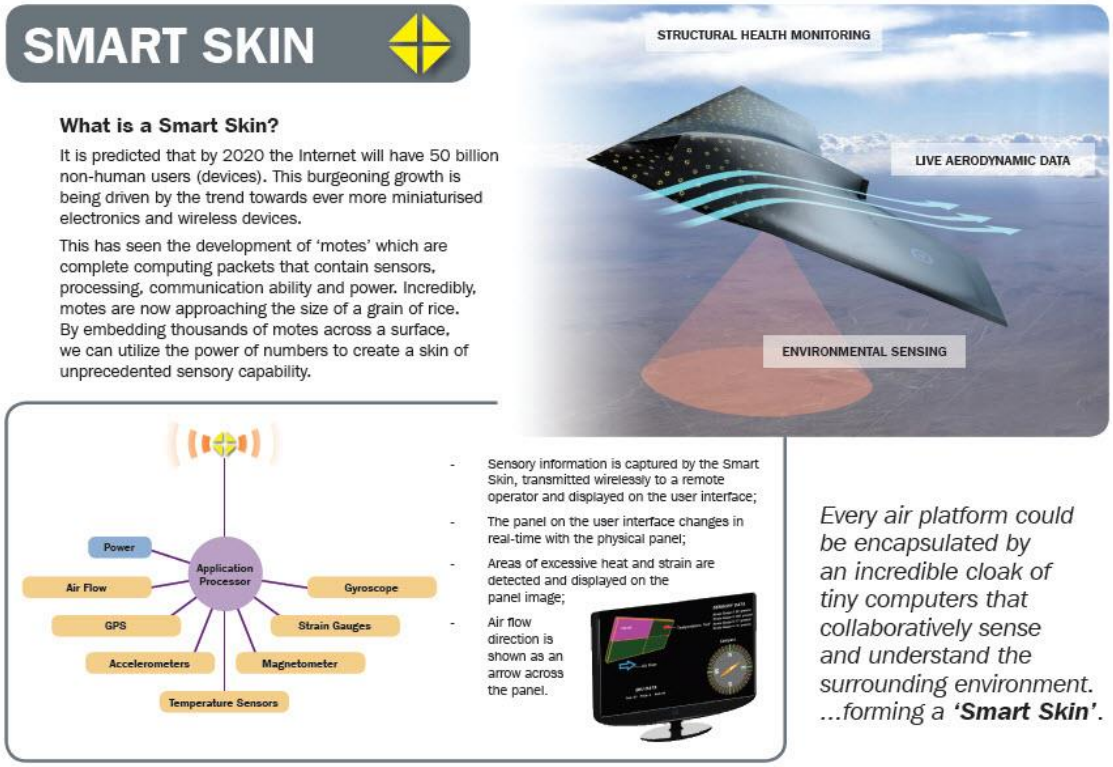

Fig. 4.25. Smart Skin project launched at BAE Systems UK.

Further progress in miniaturising and speeding up electronic devices opens up new perspectives for the use of sensor fusion systems to monitor complex composite structures. A massive amount of information collected from a large network of submerged or surface sensors can be processed in real time by using a high performance computing system. The sensors can be fed and interrogated wirelessly by means of a mutual inductance coupling or a near-field radiation. With this approach, the sensors will collect local information about the material and send it through the designated wireless channels.

Chapter V

TRL calibration of the cells – a prospective approach for improving impedance measurements at microwave frequencies

In this chapter, the TRL (Thru-Reflect-Line) calibration procedure will be explained. Deriving the TRL equations follows Ref. [5.1] but using different designations and algebra. Due to a great variety of experimental requirements, TRL cannot be considered as a routine procedure and requires a careful revision for each particular case. The need for TRL arises when the Device Under Test (DUT) cannot be attached directly to the coaxial cables. A typical practical situation is when intermediate microstrip lines on a PCB are used to deliver signals to/from DUT. The length of these strips and also the strip-to-coaxial transition will introduce a frequency dispersion of the measured parameter that can be virtually removed by means of TRL. In the previous chapter, a much simpler calibration procedure was proposed that takes into account the phase and amplitude distortions for the transmission coefficient. Though these distortions give the major contribution, multiple reflections may become significant at higher frequencies.

TRL was not covered by experiments in this project. The main issue that prevented the use of TRL was a quite long measurement chain during which the strain and temperature must be kept constant. However, with access to a modern VNA with fast frequency sweep and data transfer this technical problem should be resolved. TRL is considered to be the most accurate calibration procedure for the impedance measurements at microwave frequencies.

5.1. Concept of the TRL calibration

For TRL, we will work in the frequency domain, and hence all operators are simple multiplicators. The operation of a two-port linear network can be described by the scattering matrix S_{ij} introduced in Eqs. (4.3) and (4.4). The system of equations (4.3) can be also interpreted as a coupling of two ports through the network:

$$\begin{pmatrix} b_2 \\ a_2 \end{pmatrix} = \frac{1}{S_{12}} \begin{pmatrix} \left(S_{12}S_{21} - S_{22}S_{11}\right) & S_{22} \\ -S_{11} & 1 \end{pmatrix} \begin{pmatrix} a_1 \\ b_1 \end{pmatrix} \tag{5.1}$$

where

$$\frac{1}{S_{12}} \begin{pmatrix} \left(S_{12}S_{21} - S_{22}S_{11}\right) & S_{22} \\ -S_{11} & 1 \end{pmatrix} = \begin{pmatrix} P_{11} & P_{12} \\ P_{21} & P_{22} \end{pmatrix} = \hat{\mathbf{P}} \tag{5.2}$$

is called the propagation matrix that acts on the left port vector $\begin{pmatrix} a_1 \\ b_1 \end{pmatrix}$ and produces the right port vector $\begin{pmatrix} b_2 \\ a_2 \end{pmatrix}$. In some papers and books, $\hat{\mathbf{P}}$ is defined as acting on the right port vector and producing the left port vector, but here the preferred form is (5.1). Unlike the scattering matrices, the propagation matrices can be cascaded when networks are connected in series. The propagation matrix of a cascaded network will be the ordered product of the propagation matrices of the constituent networks.

The TRL calibration is used to extract the pure network properties of DUT (also linear) when it is placed between two fixtures that transfer signals from the external feeding lines (standard coaxial cables or waveguides), as shown schematically in Fig. 5.1. The cascaded network will have the propagation matrix $\hat{\mathbf{P}}_{\mathrm{N}}$ defined as:

$$\hat{\mathbf{P}}_{\mathrm{N}} = \hat{\mathbf{P}}_{\mathrm{B}}\hat{\mathbf{P}}_{\mathrm{D}}\hat{\mathbf{P}}_{\mathrm{A}} = \frac{1}{S_{\mathrm{N12}}}\begin{pmatrix} \left(S_{\mathrm{N12}}S_{\mathrm{N21}} - S_{\mathrm{N22}}S_{\mathrm{N11}}\right) & S_{\mathrm{N22}} \\ -S_{\mathrm{N11}} & 1 \end{pmatrix} \tag{5.3}$$

where the indexes A and B indicate the left and right fixtures respectively, and D – DUT. Each matrix in Eq. (5.3) has a structure similar to that of Eq. (5.2). By normal agreement, the Ports I and II will be at the left and right sides, respectively.

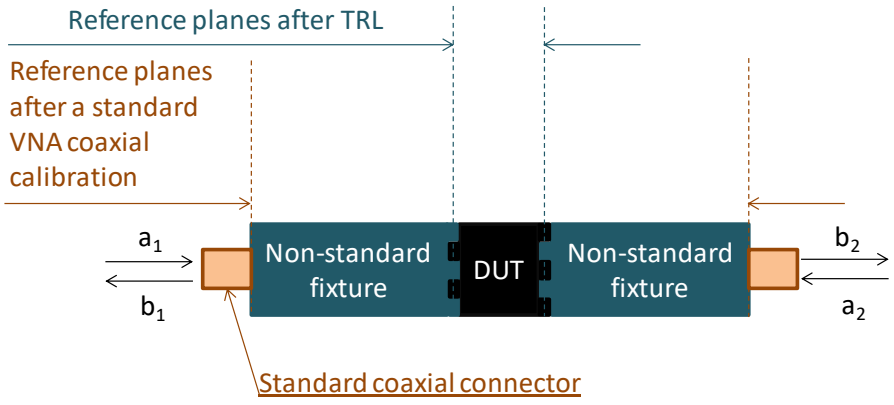

Fig. 5.1. A typical measurement arrangement when the TRL calibration is required: DUT cannot be connected directly to the feeding coaxial lines with the standard connectors. Some special fixtures are required to transfer signals from the coaxial connectors to DUT and back.

If a DUT is not compatible with the standard connectors of the external feeding lines, its network properties cannot be measured directly. TRL allows the extraction of $\hat{\mathbf{P}}_D$ from three types of measurements (see Fig. 5.2):

- **T**HRU, when two fixtures are connected together.
- **R**EFLECT, when the fixtures are left unconnected or some good OPEN or SHORT terminations can be attached to improve the reflectivity from the ends of fixtures.
- **L**INE, when DUT is replaced with a well-defined transmission line with negligible reflection coefficients with respect to the fixtures. It is recommended that for a chosen frequency range, the line should introduce a phase shift within $[20°,160°]$ with respect to the THRU. Thus, several lines may be needed to cover the whole frequency range.

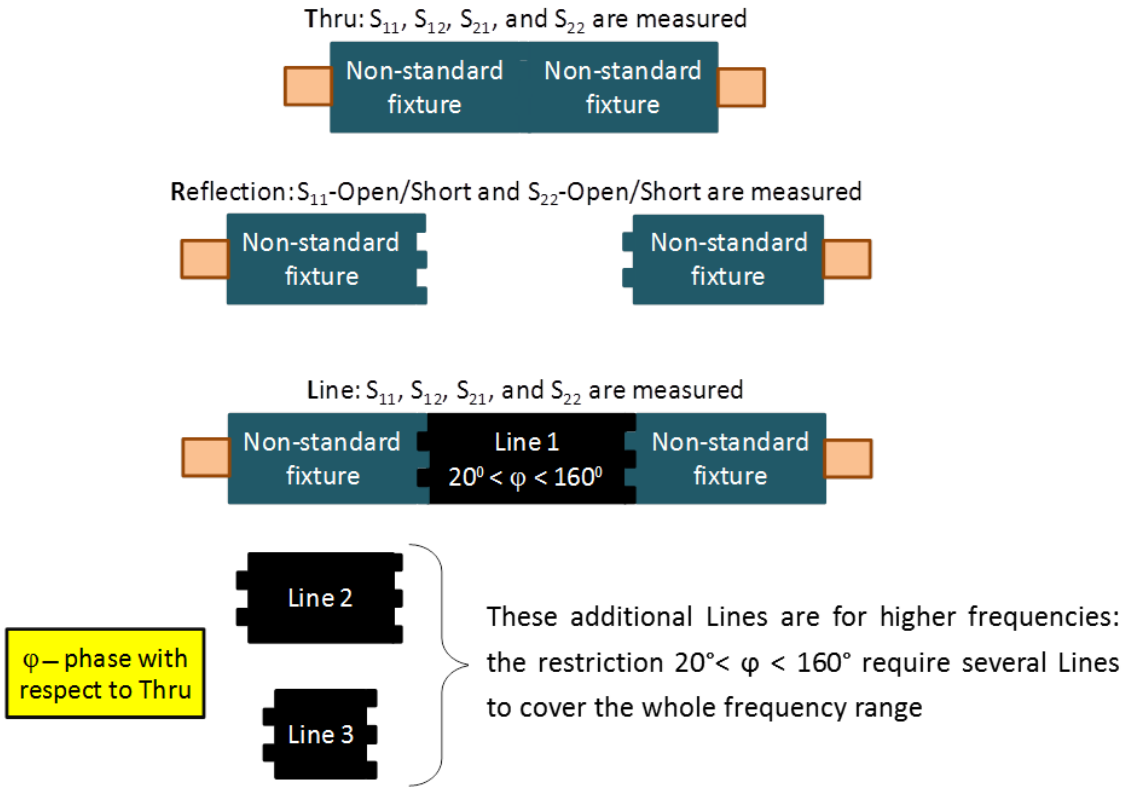

Fig. 5.2. Three types of measurements used in the TRL calibration.

Fig. 5.3 explains how TRL can be used for the applications here. The measurement cell includes SMA connectors, microstrips, and a wire sample connected to the microstrips by means of conductive paint. A standard 2-port VNA coaxial calibration cannot establish the reference plane beyond the coaxial connectors. After TRL, the reference planes will be shifted much closer to DUT. The TRL calibration

measurements for this cell are shown in Fig. 5.4. The method in Fig. 5.4 is destructive because the cell has to be damaged (after the measurements) to prepare THRU and also to insert additional LINES. Usually, all TRL calibration standards are made on a separate PCB, but it must have the same isotropic dielectric properties as the PCB used for the fixtures. FR4 composite matrix is not very good in this respect. Specialised RF boards, for example from Rogers Corporation, would be preferable.

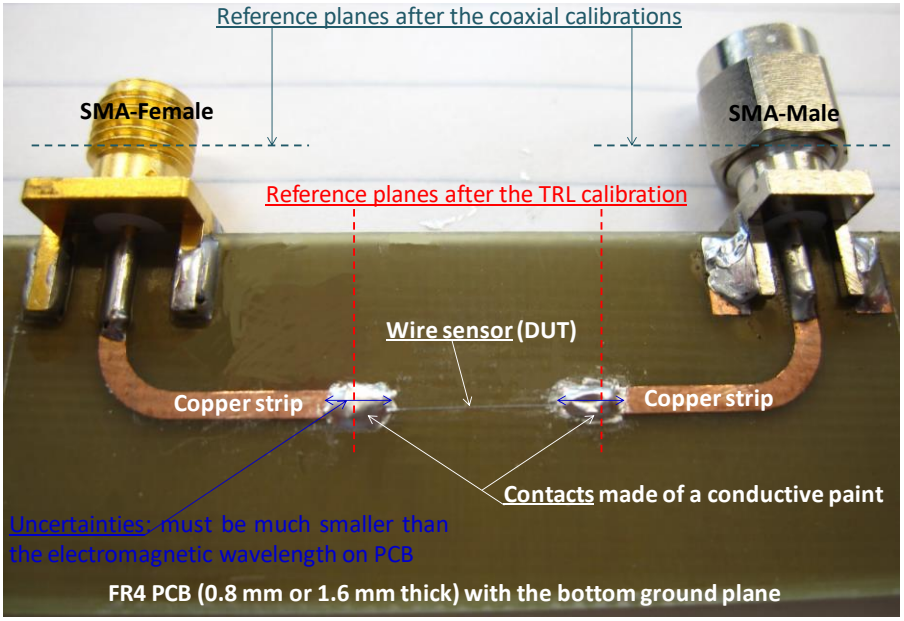

Fig. 5.3. A practical measurement cell where the TRL calibration can be used to shift the reference planes. Here, the fixtures include SMA connectors, PCB microstrips, and the sample contacts (conductive paint). DUT is a wire sample, the impedance of which is being measured. In the frequency domain, the largest distortion will be due to a phase shift introduced by the microstrips.

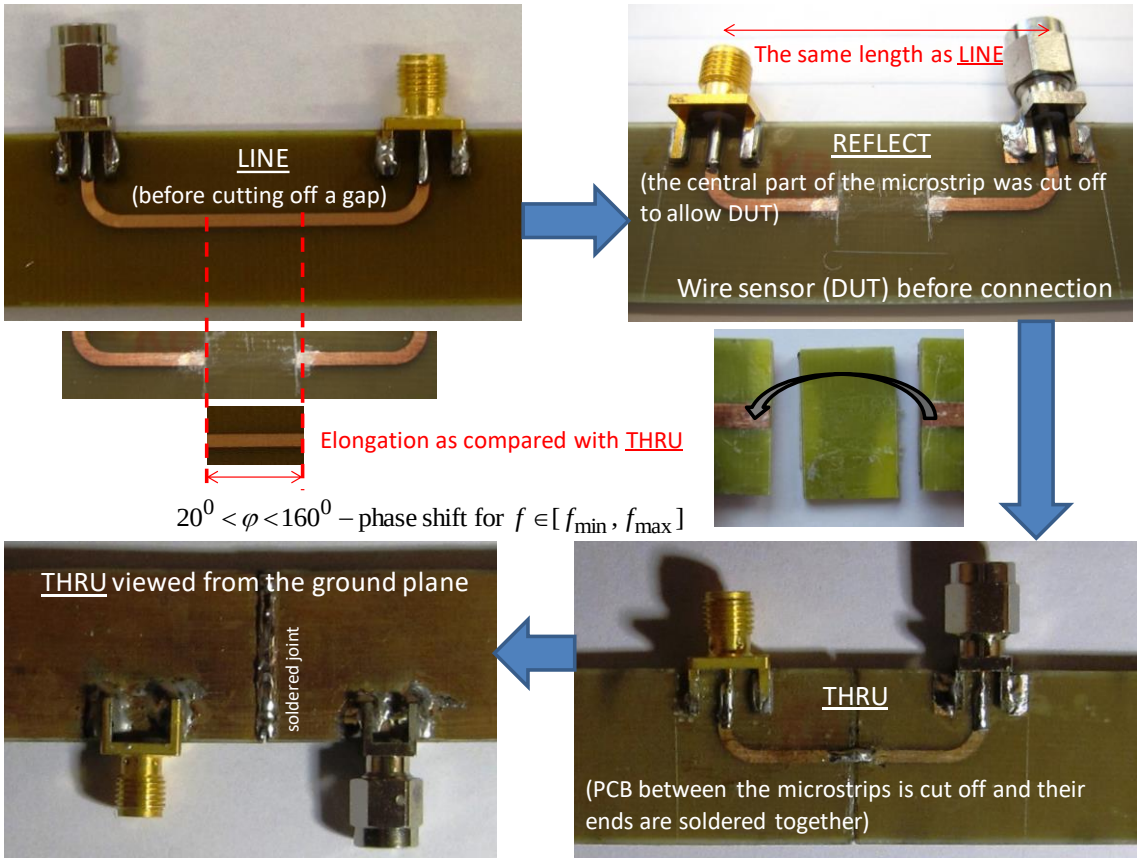

Fig. 5.4. A destructive method used for preparation of the TRL calibration standards on PCB.

It will be always assumed that the propagation matrix of a line (without fixtures) neglects reflection and has the following form:

$$\hat{\mathbf{P}}_{\mathrm{L}} = \begin{pmatrix} S_{\mathrm{L21}} & 0 \\ 0 & \dfrac{1}{S_{\mathrm{L12}}} \end{pmatrix} \tag{5.4}$$

For a line with no losses or dispersion, a very simple model would be $S_{\mathrm{L21}} = \exp(-i f l / v)$, where l is the length of line, f is the frequency, and v is the propagation speed of electromagnetic waves in the line. However, in practice some losses and dispersion are usually present, and hence the model will be more complicated: $S_{\mathrm{L21}} = A(f,l)\exp(-i\gamma(f)l)$, where the amplitude factor $A(f,l) \le 1$ now depends on the length and frequency.

With $\hat{\mathbf{P}}_{\mathrm{A,B}}$ reconstructed from TRL and the $\hat{\mathbf{P}}_{\mathrm{N}}$ measured by a VNA, the matrix $\hat{\mathbf{P}}_{\mathrm{D}}$ can be found as:

$$\hat{\mathbf{P}}_{\mathrm{D}} = \hat{\mathbf{P}}_{\mathrm{B}}^{-1}\hat{\mathbf{P}}_{\mathrm{N}}\hat{\mathbf{P}}_{\mathrm{A}}^{-1} \tag{5.5}$$

where $\hat{\mathbf{P}}_{\mathrm{A}}^{-1}$ and $\hat{\mathbf{P}}_{\mathrm{B}}^{-1}$ are the inverse matrices. Using the form (5.2), *S*-parameters of the DUT and fixtures can be expressed through the components of the corresponding $\hat{\mathbf{P}}$:

$$\begin{cases} S_{11} = -\dfrac{P_{21}}{P_{22}} \\ S_{12} = \dfrac{1}{P_{22}} \\ S_{21} = P_{11} - \dfrac{P_{12}P_{21}}{P_{22}} \\ S_{22} = \dfrac{P_{12}}{P_{22}} \end{cases} \tag{5.6}$$

The models for the TRL measurements are now introduced:

<u>Preliminary measurement</u>: DUT is connected to the fixtures, and all S-parameters are measured. The matrix $\hat{\mathbf{P}}_{\mathrm{N}}$ will be created (see Eq. (5.3)).

<u>THRU</u>: DUT is removed and two fixtures are connected together. All S-parameters are measured. The propagation matrix $\hat{\mathbf{P}}_{\mathrm{TH}}$ of this network has the form:

$$\hat{\mathbf{P}}_{\mathrm{TH}} = \hat{\mathbf{P}}_{\mathrm{B}}\hat{\mathbf{P}}_{\mathrm{A}} \tag{5.7}$$

where

$$\hat{\mathbf{P}}_{\mathrm{TH}} = \begin{pmatrix} \dfrac{S_{\mathrm{TH12}}S_{\mathrm{TH21}} - S_{\mathrm{TH22}}S_{\mathrm{TH11}}}{S_{\mathrm{TH12}}} & \dfrac{S_{\mathrm{TH22}}}{S_{\mathrm{TH12}}} \\ -\dfrac{S_{\mathrm{TH11}}}{S_{\mathrm{TH12}}} & \dfrac{1}{S_{\mathrm{TH12}}} \end{pmatrix} = \begin{pmatrix} t_{11} & t_{12} \\ t_{21} & t_{22} \end{pmatrix} \tag{5.8}$$

<u>LINE</u>: A line is connected instead of DUT. All S-parameters are measured. The propagation matrix $\hat{\mathbf{P}}_{\mathrm{LINE}}$ of this network ("furred" line) has the form:

$$\hat{\mathbf{P}}_{\mathrm{LINE}} = \hat{\mathbf{P}}_{\mathrm{B}}\hat{\mathbf{P}}_{\mathrm{L}}\hat{\mathbf{P}}_{\mathrm{A}} \tag{5.9}$$

where

$$\hat{\mathbf{P}}_{\text{LINE}} = \begin{pmatrix} \dfrac{S_{\text{LINE12}}S_{\text{LINE21}} - S_{\text{LINE22}}S_{\text{LINE11}}}{S_{\text{LINE12}}} & \dfrac{S_{\text{LINE22}}}{S_{\text{LINE12}}} \\ -\dfrac{S_{\text{LINE11}}}{S_{\text{LINE12}}} & \dfrac{1}{S_{\text{LINE12}}} \end{pmatrix} \tag{5.10}$$

and $\hat{\mathbf{P}}_{\text{L}}$ ("pure" line) is given in Eq. (5.4).

REFLECT: DUT is removed and the fixtures are left unconnected or some good OPEN/SHORT terminations can be attached. For this arrangement, the only parameters which can be measured are the reflection coefficients S_{RE11} (left fixture) and S_{RE22} (right fixture). Using the signal flow graphs in Fig. 5.5, gives:

$$S_{\text{RE11}} = \frac{b_1}{a_1} = S_{\text{A11}} + \frac{S_{\text{A21}}S_{\text{A12}}\Gamma_{\text{A}}}{1-\Gamma_{\text{A}}S_{\text{A22}}} = \frac{S_{\text{A11}} + \left(S_{\text{A21}}S_{\text{A12}} - S_{\text{A11}}S_{\text{A22}}\right)\Gamma_{\text{A}}}{1-\Gamma_{\text{A}}S_{\text{A22}}} \tag{5.11}$$

$$S_{\text{RE22}} = \frac{b_2}{a_2} = S_{\text{B22}} + \frac{S_{\text{B21}}S_{\text{B12}}\Gamma_{\text{B}}}{1-\Gamma_{\text{B}}S_{\text{B11}}} = \frac{S_{\text{B22}} + \left(S_{\text{B21}}S_{\text{B12}} - S_{\text{B11}}S_{\text{B22}}\right)\Gamma_{\text{B}}}{1-\Gamma_{\text{B}}S_{\text{B11}}} \tag{5.12}$$

where $\Gamma_{\text{A,B}}$ are the reflection coefficients from the fixture ends (open or terminated with a good OPEN/SHORT). For the measurement cell in Fig. 5.3, $\Gamma_{\text{A}} \equiv \Gamma_{\text{B}} = \Gamma$.

If the fixture ends are left open or terminated with an OPEN, then $\Gamma \approx 1$, although the radiation losses may reduce this value. If they are shorted or terminated with a SHORT, then $\Gamma \approx -1$.

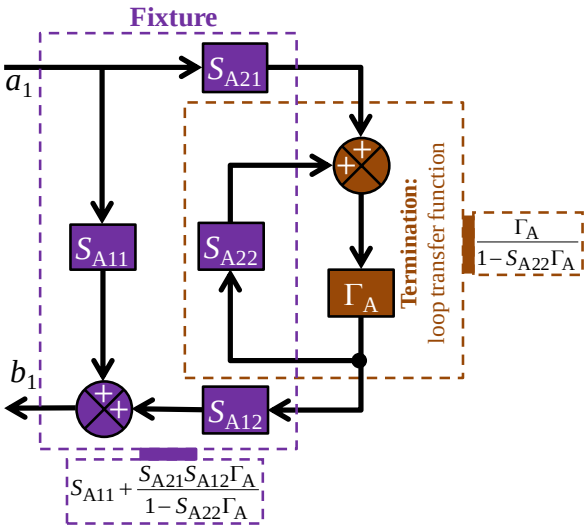

Fig. 5.5. Signal flow graph for the reflection from the left fixture (A) when it is disconnected from the right fixture (B). Γ_A is the reflection coefficient from the fixture termination: usually it is a "good" OPEN, but a "good" SHORT can be also used. The right fixture will have a similar signal flow graph, where A must be replaced with B, and the indices 1 and 2 must be interchanged.

Substituting $\hat{\mathbf{P}}_B = \hat{\mathbf{P}}_{TH}\hat{\mathbf{P}}_A^{-1}$ from Eq. (5.7) into (5.9), we obtain:

$$\hat{\mathbf{P}}_A\hat{\mathbf{P}}_{LTH} = \hat{\mathbf{P}}_L\hat{\mathbf{P}}_A \tag{5.13}$$

where

$$\hat{\mathbf{P}}_{LTH} = \hat{\mathbf{P}}_{TH}^{-1}\hat{\mathbf{P}}_{LINE} = \begin{pmatrix} h_{11} & h_{12} \\ h_{21} & h_{22} \end{pmatrix} \tag{5.14}$$

$$\hat{\mathbf{P}}_{TH}^{-1} = \frac{1}{S_{TH21}}\begin{pmatrix} 1 & -S_{TH22} \\ S_{TH11} & (S_{TH12}S_{TH21} - S_{TH22}S_{TH11}) \end{pmatrix} \tag{5.15}$$

where Eq. (5.15) is the inverse of $\hat{\mathbf{P}}$.

$\hat{\mathbf{P}}_A$ and $\hat{\mathbf{P}}_B$ can be represented in the following form, which will be used for the calculations:

$$\hat{\mathbf{P}}_A = \frac{1}{S_{A12}}\begin{pmatrix} (S_{A12}S_{A21} - S_{A22}S_{A11}) & S_{A22} \\ -S_{A11} & 1 \end{pmatrix} = \rho\begin{pmatrix} \chi & \beta \\ -\alpha & 1 \end{pmatrix} \tag{5.16}$$

$$\hat{\mathbf{P}}_{\mathrm{B}}=\frac{1}{S_{\mathrm{B12}}}\begin{pmatrix}\left(S_{\mathrm{B12}}S_{\mathrm{B21}}-S_{\mathrm{B22}}S_{\mathrm{B11}}\right) & S_{\mathrm{B22}}\\ -S_{\mathrm{B11}} & 1\end{pmatrix}=r\begin{pmatrix}c & b\\ -a & 1\end{pmatrix} \tag{5.17}$$

$$\hat{\mathbf{P}}_{\mathrm{A}}^{-1}=\frac{1}{\rho\left(\chi+\alpha\beta\right)}\begin{pmatrix}1 & -\beta\\ \alpha & \chi\end{pmatrix} \tag{5.18}$$

$$\hat{\mathbf{P}}_{\mathrm{B}}^{-1}=\frac{1}{r\left(c+ab\right)}\begin{pmatrix}1 & -b\\ a & c\end{pmatrix} \tag{5.19}$$

Substituting Eqs. (5.18),(5.19) into Eq. (5.5), and Eqs. (5.16),(5.17) into Eqs. (5.7),(5.13), we obtain:

$$\hat{\mathbf{P}}_{\mathrm{D}}=\frac{1}{S_{\mathrm{N12}}r\rho\left(\chi+\alpha\beta\right)\left(c+ab\right)}\begin{pmatrix}1 & -b\\ a & c\end{pmatrix}\begin{pmatrix}\left(S_{\mathrm{N12}}S_{\mathrm{N21}}-S_{\mathrm{N22}}S_{\mathrm{N11}}\right) & S_{\mathrm{N22}}\\ -S_{\mathrm{N11}} & 1\end{pmatrix}\begin{pmatrix}1 & -\beta\\ \alpha & \chi\end{pmatrix} \tag{5.20}$$

$$\begin{pmatrix}\chi & \beta\\ -\alpha & 1\end{pmatrix}\begin{pmatrix}h_{11} & h_{12}\\ h_{21} & h_{22}\end{pmatrix}=\begin{pmatrix}S_{\mathrm{L21}} & 0\\ 0 & \dfrac{1}{S_{\mathrm{L12}}}\end{pmatrix}\begin{pmatrix}\chi & \beta\\ -\alpha & 1\end{pmatrix} \tag{5.21}$$

$$\begin{pmatrix}t_{11} & t_{12}\\ t_{21} & t_{22}\end{pmatrix}=\rho r\begin{pmatrix}c & b\\ -a & 1\end{pmatrix}\begin{pmatrix}\chi & \beta\\ -\alpha & 1\end{pmatrix} \tag{5.22}$$

In Eq. (5.20), there are seven unknowns $\left\{r\rho,a,b,c,\alpha,\beta,\chi\right\}$. To find them, two matrix equations (5.21),(5.22) and two scalar equations (5.11),(5.12) can be used. Presenting Eq. (5.21) and (5.22) componentwise, we obtain:

$$\begin{cases}\dfrac{\chi h_{11}+\beta h_{21}}{\chi}=S_{\mathrm{L21}}\\ \dfrac{\chi h_{12}+\beta h_{22}}{\beta}=S_{\mathrm{L21}}\\ \dfrac{-\alpha h_{11}+h_{21}}{-\alpha}=\dfrac{1}{S_{\mathrm{L12}}}\\ -\alpha h_{12}+h_{22}=\dfrac{1}{S_{\mathrm{L12}}}\end{cases} \tag{5.23}$$

$$\begin{cases}t_{11}=\rho r\left(c\chi-b\alpha\right)\\ t_{12}=\rho r\left(c\beta+b\right)\\ t_{21}=\rho r\left(-a\chi-\alpha\right)\\ t_{22}=\rho r\left(-a\beta+1\right)\end{cases} \tag{5.24}$$

Excluding $\left\{S_{\mathrm{L12}},S_{\mathrm{L}21}\right\}$ and ρr in Eqs. (5.23),(5.24), and $\Gamma=\Gamma_{\mathrm{A}}\equiv\Gamma_{\mathrm{B}}$ in Eqs. (5.11),(5.12), the following systems of non-linear equations is obtained:

$$\begin{cases} \alpha^2 h_{12} + \alpha(h_{11} - h_{22}) - h_{21} = 0 \\ \left(\dfrac{\chi}{\beta}\right)^2 h_{12} + \dfrac{\chi}{\beta}(h_{22} - h_{11}) - h_{21} = 0 \end{cases} \tag{5.25}$$

$$\begin{cases} \dfrac{t_{11}}{c\chi - b\alpha} = \dfrac{t_{12}}{c\beta + b} = \dfrac{t_{21}}{-a\chi - \alpha} = \dfrac{t_{22}}{-a\beta + 1} \\ \dfrac{S_{\mathrm{RE}11} - \alpha}{\chi + \beta S_{\mathrm{RE}11}} = \dfrac{S_{\mathrm{RE}22} - b}{c + aS_{\mathrm{RE}22}} \end{cases} \tag{5.26}$$

Note that $-\alpha$ and χ/β in Eq. (5.25) satisfy the same square equation. The rule for choosing the roots will be proposed later. From the first expression in Eq. (5.26), the three equations are:

$$\begin{cases} \dfrac{t_{11}}{c\dfrac{\chi}{\beta} - \dfrac{b}{\beta}\alpha} = \dfrac{t_{12}}{c + \dfrac{b}{\beta}} \\ \dfrac{t_{21}}{-a\dfrac{\chi}{\beta} - \alpha\dfrac{1}{\beta}} = \dfrac{t_{22}}{-a + \dfrac{1}{\beta}} \\ \dfrac{t_{12}}{c + \dfrac{b}{\beta}} = \dfrac{t_{21}}{-a\dfrac{\chi}{\beta} - \alpha\dfrac{1}{\beta}} \end{cases} \tag{5.27}$$

Solving these equations with respect to c, gives:

$$\begin{cases} b = \dfrac{\dfrac{\chi}{\beta}t_{12} - t_{11}}{\dfrac{\chi}{\beta}t_{22} - t_{21}} \\ a = -c \times \dfrac{t_{21} + \alpha t_{22}}{t_{11} + \alpha t_{12}} = -c \times R_a \\ \beta = \dfrac{1}{c} \times \dfrac{t_{11} + \alpha t_{12}}{\dfrac{\chi}{\beta}t_{22} - t_{21}} = \dfrac{1}{c} \times R_\beta \end{cases} \tag{5.28}$$

where

$$\begin{cases} R_a = \dfrac{t_{21} + \alpha t_{22}}{t_{11} + \alpha t_{12}} \\ R_\beta = \dfrac{t_{11} + \alpha t_{12}}{\dfrac{\chi}{\beta}t_{22} - t_{21}} \end{cases} \tag{5.29}$$

Substituting $1/\beta$, b, and a into the second equation in Eq. (5.26), to find c:

$$c = \pm\sqrt{\frac{R_\beta\left(S_{\mathrm{RE22}} - b\right)\times\left(\dfrac{\chi}{\beta} + S_{\mathrm{RE11}}\right)}{\left(1 - R_a S_{\mathrm{RE22}}\right)\times\left(S_{\mathrm{RE11}} - \alpha\right)}} \tag{5.30}$$

In Ref. [5.1], the following criterion was proposed for choosing the roots in Eq. (5.25):

$$|\alpha| < \left|\frac{\chi}{\beta}\right| \tag{5.31}$$

For short fixtures, which are usually designed to minimise distortions (for example, 50 Ω microstrips), $|S_{\mathrm{A12}}S_{\mathrm{A21}}| \approx 1$, $|S_{\mathrm{A11}}| << 1$ and $|S_{\mathrm{A22}}| << 1$ that Eq. (5.31) obvious. For longer fixtures, that inequality should be expected to remain. The correct sign in Eq. (5.30) can be chosen from the condition that $\Gamma \approx 1$ (OPEN) or $\Gamma \approx -1$ (SHORT):

$$\Gamma = \frac{S_{\mathrm{RE22}} - b}{c + aS_{\mathrm{RE22}}} = \frac{S_{\mathrm{RE22}} - b}{c(1 - R_a S_{\mathrm{RE22}})} \tag{5.32}$$

Using Eqs. (5.24),(5.25) and the constants calculated at the previous steps, $\chi = (\chi/\beta)\beta$ and ρr can be calculated:

$$\rho r = \frac{t_{12}}{c\beta + b} = \frac{t_{22}}{-a\beta + 1} = \frac{t_{21}}{-a\chi - \alpha} = \frac{t_{11}}{c\chi - b\alpha} \tag{5.33}$$

Due to unavoidable measurement errors, ρr may have four slightly different values obtained from the ratios in Eq. (5.33). In practical situations, we can take the average ρr.

The S-parameter models of the fixtures can be recovered from Eqs. (5.16) and (5.17), if ρ and r are known separately, while Eq. (5.33) gives only their product. However, for a reciprocal network, $S_{12} = S_{21}$. In this case, we obtain:

$$\rho = \pm\sqrt{\chi + \alpha\beta} \tag{5.34}$$

$$r = \pm\sqrt{c + ab} \tag{5.35}$$

The correct signs in Eqs. (5.34) and (5.35) can be found from the condition $\lim_{f \to 0} S_{21}(f) = 1$.

5.2. Program code in Fortran

For the TRL calibration, we need to measure all four S-parameters from/through the cell regardless which parameter (reflection or transmission) will be used for calculation of the impedance. The program code for TRL is attached in Appendix D (see page 130-133). It has not yet been tested.

Summary of Chapters

- Chapter I introduces glass-coated microwires and explores some fabrication technology processes relevant to understanding their properties. Microwire magneto-anisotropic (defined by alloy compositions and the residual stresses between the metal core and the glass shell induced during the casting process) and conductive properties are of particular interest. Taylor-Ulitovski method used for manufacturing glass-coated microwires is described in detail (see Section 1.3). A visit to the leading microwire manufacturing company (MFTI Ltd, Republic of Moldova) is also described (see Section 1.2).

- Chapter II presents a new method for monitoring internal stresses that can be classified as an embedded sensing technique, which uses a glass-coated ferromagnetic microwire with a specific magnetic anisotropy as a sensing element. Impedance of this sensing element (microwire) is monitored in the MHz range in presence of external stress. Magnetostatic and impedance models for glass-coated microwires required during analysis of experimental results are explained (see Section 2.2). Experiment monitoring internal tensile stress in polymer materials using microwire stress-impedance is described in Section 2.5. See Section 2.6 for detailed summary and conclusions.

- The next stage of this project aims to study the high frequency (GHz) impedance properties of microwires subjected to external stimuli such as tensile stress and temperature. Chapter III partially addresses a very significant issue typical for such experiments: design of measurement fixtures. Designs and fabrication of PCB microstrip measurement cells and the procedure to attach microwires on them are detailed in Section 3.1 and Section 3.4. One of the common difficulties when connecting microwires to microstrips is the removal of the glass shell at the ends of a microwire sample. Glass was removed with the help of a scalpel and the procedure is also described in Section 3.4. The experimental setup for RF stress-impedance measurements (which includes a VNA, coaxial SMA 3.5 mm cables connecting the cell with the VNA, a Helmholtz coil encompassing the central test section of dog-bone cells, a programmable function generator providing ± DC offset voltages for a power amplifier that feeds the coil, and a screw-driven universal test machine) are detailed in Section 3.3 (also see Fig. 3.8). Fixtures for the temperature-

impedance measurements are presented in Section 3.5. For more accurate temperature-impedance measurements, a more sophisticated heating control system should be designed in the future.

- Chapter IV explains in detail scattering parameters (S-parameters) and develops experimental methods that allow accurate measurements of surface magneto-impedance of microwires at the GHz frequencies in presence of tensile stress and heat. See Section 4.4 for the effect of strain and Section 4.5 for the effect of temperature on surface impedance. Suggestions for future work in this field in the form of free space measurements are presented in Section 4.6. See Section 4.7 for final thoughts relating to NDT of composites.

- Chapter V explains the TRL calibration procedure – the most accurate calibration procedure for non-coaxial impedance measurements at microwave frequencies. The need for TRL arises when a DUT (microwire) cannot be directly attached to the coaxial connectors (as in experiments of Chapter IV). Although TRL was not used in this project, in future research it might greatly expand the frequency range for the correct calibration of the measurement cells.

References

[1.1] E. Y. Badinter, N. R. Berman, E. F. Drabenko, V. I. Zaborovsky, Z. I. Zelikovsky, B. G. Cheban. **Cast microwire and its properties.** Chișinău: Shtiintsa. (1973).

[1.2] SEM image of a glass-coated amorphous microwire (courtesy A. Zhukov).

[1.3] G. F. Taylor. **A method of drawing metallic filaments and a discussion of their properties and uses.** Physical Review. 23, (1924), pp. 660-665

[1.4] A. V. Ulitovski., I.M. Maianski, A.I. Avramenco. **"Method of continuous casting of glass coated microwire"**. (USSR's Certificate of Authorship № 161325, class B21c, 701), Bulletin, 10 (1960), pp. 14

[1.5] R. Stone. **Banishing Moldova's Demons.** Science Magazine. 304, 5674, (2004), pp. 1098-1100

[1.6] G. F. Taylor. **Process and Apparatus for Making Filaments,** Patented Feb. 24, 1931. United States Patent Office. 1931, I, 793, 529

[1.7] MTS Sensors Group. **Magnetostriction.** Basic Physical Elements. (2001), pp. 1-4.

[1.8] E. Badinter, A. Ioisher, E. Monaico, V. Postolache, I.M. Tiginyanu. **Exceptional integration of metal or semimetal nanowires in human-hair-like glass fiber.** Materials Letters. 64 (2010), pp. 1902–1904

[1.9] A. A. Griffiths. **The Phenomena of Rupture and Flow in Solids.** Phil. Trans. R. Soc. §6 (1921), pp. 163-198

[1.10] B. V. Farmakovskiy. **Investigations of several physico-mechanical characteristics of cast microwires at elevated temperatures and humidity**. Details and components of apparatuses. 1 (10), (1969), pp. 124-138.

[1.11] W. Johnson, H. Kudo. **The Mechanics of Metal Extrusion.** Manchester University Press, 1962.

[1.12] Wikipedia contributors. **"Extrusion."** Wikipedia, The Free Encyclopaedia. 19 Mar. 2016.

[1.13] Wikipedia contributors. **"Recrystallization (metallurgy)."** Wikipedia, The Free Encyclopaedia. 20 Mar. 2006

[1.14] A-L. A. Engelvina, C. Dudeka, F. Bertina, O. Acher. **Thermal stability up to 400°C of the magnetic properties of Finemet-based nanocrystallized glass-coated microwires.** Journal of Magnetism and Magnetic Materials. 316, (2007), pp. 831-833

[2.1] H. Chiriac and T.-A. Ovari **Amorphous Glass-Covered Magnetic Wires: Preparation, Properties, Applications** Progr. Mater. Sci. 40 (1996), pp. 333-407

[2.2] A. Zhukov and V. Zhukova **Magnetic properties and applications of ferromagnetic microwires with amorphous and nanocrystalline structure** Nova Science Publishers, New York (2009)

[2.3] M. Vazquez, H. Chiriac, A. Zhukov, L. Panina, T. Uchiyama **On the state-of-the-art in magnetic microwires and expected trends for scientific and technological studies** Phys. Status Solidi A 208 (2011), pp. 493-501

[2.4] F. X. Qin, H.-X. Peng, N. Pankratov, M. H. Phan, L. V. Panina, M. Ipatov, V. Zhukova, A. Zhukov, J. Gonzalez **Exceptional electromagnetic interference shielding properties of ferromagnetic microwires enabled polymer composites** J. Appl. Phys. 108 (2010), pp. 044510-15

[2.5] G. Ababei, H. Chiriac, V. David, V. Dafinescu, I. Nica **Omni-directional selective shielding material based on amorphous glass coated microwires** Rev. Sci. Instrum. 83 (2012), pp. 014701-5

[2.6] F. X. Qin, H.-X. Peng, Z. Chen, G. Hilton **Microwave Absorption of Structural Polymer Composites Containing Glass-Coated Amorphous Microwires** IEEE Trans. Magn. 49 (2013), pp. 4245-4248

[2.7] L. Panina and K. Mohri **Magneto-impedance effect in amorphous wires** Appl. Phys. Lett. 65 (1994), pp. 1189-1191

[2.8] M. Knobel and K. R. Pirota **Giant magnetoimpedance: concepts and recent progress** J. Magn. Magn. Mater. 242/245 (2002), pp. 33-40

[2.9] K. Mohri, F. B. Humphrey, L. V. Panina, Y. Honkura, J. Yamasaki, T. Uchiyama, M. Hirami **Advances of amorphous wire magnetics over 27 years** Phys. Status Solidi A 206 (2009), pp. 601-607

[2.10] G. F. Fernando **Fibre optic sensor systems for monitoring composite structures** Reinf. Plast. 49 (2005), pp. 41-49

[2.11] K. Peters **Polymer optical fiber sensors - a review** Smart Mater. Struct. 20 (2011), pp. 013002-18

[2.12] J. M. Torrents, T. O. Mason, E. J. Garboczi **Impedance spectra of fiber-reinforced cement-based composites. A modeling approach** Cem. Concr. Research. 30 (2000), pp. 585-592

[2.13] A. D. Hixson, L. Y. Woo, M. A. Campo, T. O. Mason, E. J. Garboczi **Intrinsic conductivity of short conductive fibers in composites by impedance spectroscopy** J. Electroceramics 7 (2001), pp. 189-195

[2.14] A. Peled, J. M. Torrents, Th. O. Mason, S. P. Shah, E. J. Garboczi **Electrical impedance spectra to monitor damage during tensile loading of cement composites** ACI Maters. Journal 98 (2001), pp. 313-322

[2.15] J. M. Torrents, T. O. Mason, A. Peled, S. P. Shah, E. J. Garboczi **Analysis of the impedance spectra of short conductive fiber reinforced composites** J. Mater. Sci. 36 (2001), pp. 4003-12

[2.16] T. C. Hou and J. P. Lynch **Electrical impedance tomographic methods for sensing strain fields and crack damage in cementitious structures** J. Intel. Mater. Syst. Struct. 20 (2009), pp. 1363-1379

[2.17] M. Kubicka, T. Mahrholz, A. Kühn, P. Wierach, M. Sinapius **Magnetostrictive properties of epoxy resins modified with Terfenol-D particles for detection of internal stress in CFRP. Part 1: materials and process** J. Mater. Sci. 47 (2012), pp. 5752-5759

[2.18] M. Kubicka, T. Mahrholz, A. Kühn, P. Wierach, M. Sinapius **Magnetostrictive properties of epoxy resins modified with Terfenol-D particles for detection of internal stress in CFRP. Part 2: evaluation of stress detection** J. Mater. Sci. 48 (2013), pp. 6578-6584

[2.19] D. Makhnovskiy and L. Panina **Field dependent permittivity of composite materials containing ferromagnetic wires** J. Appl. Phys. 93 (2003), pp. 4120-4129

[2.20] O. Reynet, A.-L. Adenot, S. Deprot, O. Acher **Effect of the magnetic properties of the inclusions on the high-frequency dielectric response of diluted composites** Phys. Rev. B 66 (2002), pp. 094412-20

[2.21] F. X. Qin and H.-X. Peng **Ferromagnetic microwires enabled multifunctional composite materials** Progr. Mater. Sci. 58 (2013), pp. 183-259

[2.22] F. X. Qin, H.-X. Peng, J. Tang, L.-Ch. Qin **Ferromagnetic microwires enabled polymer composites for sensing applications** Composites Part A: Applied Science and Manufacturing 41 (2010), pp. 1823-1828

[2.23] J. Carbonell, H. García-Miquel, J. Sánchez-Dehesa **Double negative metamaterials based on ferromagnetic microwires** Phys. Rev. B 81 (2010), pp. 024401-6

[2.24] L. V. Panina, M. Ipatov, V. Zhukova, A. Zhukov, J. Gonzalez **Microwave metamaterials with ferromagnetic microwires** Appl. Phys. A: Mater. Sci. Proces. 103 (2011), pp. 653-657

[2.25] L.-Ph. Carignan, A. Yelon, D. Menard, Ch. Caloz **Ferromagnetic Nanowire Metamaterials: Theory and Applications** IEEE Trans. Microw. Theor. Tech. 59 (2011), pp. 2568-2586

[2.26] L. Liu, K. N. Rozanov, M. Abshinova **Tunable properties of microwire composites at microwave frequency** Appl. Phys. A: Mater. Sci. Proces. 110 (2013), pp. 275-279

[2.27] D. P. Makhnovskiy, L. V. Panina, C. Garcia, A. P. Zhukov, J. Gonzalez **Experimental demonstration of tunable scattering spectra at microwave frequencies in composite media containing CoFeCrSiB glass-coated amorphous ferromagnetic wires and comparison with theory** Phys. Rev. B 74 (2006), pp. 064205-15

[2.28] H. Chiriac and T.-A. Ovari **Magnetic properties of amorphous glass-covered wires** J. Magn. Magn. Mat. 249 (2002), pp. 46-54

[2.29] A. Zhukov, V. Zhukova, J. M. Blanco, A. F. Cobeño, M. Vazquez, J. Gonzalez **Magnetostriction in glass-coated magnetic microwires** J. Magn. Magn. Mat. 258/259 (2003), pp. 151-157

[2.30] A. Zhukov, V. Zhukov, J. M. Blanco, J. Gonzalez **Recent research on magnetic properties of glass-coated microwires** J. Magn. Magn. Mat. 294 (2005), pp. 182-192

[2.31] M. J. Sablik and D. C. Jiles **Modeling the effect of torsional stress on hysteretic magnetization** IEEE Trans. Magn. 35 (1999), pp. 498-504

[2.32] A. Aharoni **Introduction to the theory of ferromagnetism** Oxford University Press (2002)

[2.33] L. V. Panina, S. I. Sandacci, D. P. Makhnovskiy **Stress effect on magneto-impedance (MI) in amorphous wires at GHz frequencies and application to stress-tuneable microwave composite materials** J. Appl. Phys. 97 (2005), pp. 013701-6

[2.34] D. P. Makhnovskiy, L. V. Panina, D. J. Mapps **Field-dependent surface impedance tensor in amorphous wires with two types of magnetic anisotropy: helical and circumferential** Phys. Rev. B 63 (2001), pp. 144424-40

[2.35] **Construction materials: their nature and behaviour, 4th edition**, edited by J. M. Illston and P. L J. Domone, Spon Press (2010)

[2.36] A.-L. Adenot-Engelvin, Ch. Dudek, F. Bertin, O. Acher **Thermal stability up to 400 ^{0}C of the magnetic properties of Finemet-based nanocrystallized glass-coated microwires** J. Magn. Magn. Mat. 316 (2007), pp. 831-833

[2.37] S. I. Sandacci, D. P. Makhnovskiy, L. V. Panina **Valve-like behavior of the magnetoimpedance in the GHz range** J. Magn. Magn. Mat. 272/276 (2004), pp. 1855-1857

[2.38] P. Doris, J. Bruestlova, M. Bartlova **Curie temperature in ferromagnetic materials and visualized magnetic domains** 3rd International Symposium for Engineering Education, 2010, University College Cork, Ireland

[4.1] D. P. Makhnovskiy and L. V. Panina, **"Field dependent permittivity of composite materials containing ferromagnetic wires"**, Journal of Applied Physics 93, 4120 (2003)

[4.2] Landau and Lifshitz, ***"Electrodynamics of continuous media"*** http://www.amazon.com/Electrodynamics-Continuous-Media-Second-Theoretical/dp/0750626348

[4.3] M. Hiebel, ***"Fundamentals of Vector Network Analysis"***, Rohde&Schwarz, Fifth edition 2011

[4.4] B. C. Wadell, ***"Transmission Line Design Handbook",*** Artech House, Norwood, MA 1991

[4.5] G. H. Bryant, ***"Principles of microwave measurements"***, Peter Peregrinus Ltd, 1988.

[4.6] G. F. Engen, C. A. Hoer, **"Thru-Reflect-Line: An improved technique for calibrating the dual six-port automatic network analyser"**, IEEE Transactions on Microwave Theory and Techniques, Vol. 27, pp. 987-983, 1979.

[4.7] B. C. Wadell, **"Transmission line design handbook"**, Artech House, 1991.

[4.8] E. F. Kuester and D. C. Chang, **"Propagating modes along a thin wire located above a ground dielectric slab"**, IEEE Transactions on Microwave Theory and Techniques, Vol. 25, pp. 1065-1069, 1977.

[4.9] V. Zhukova et al., **"Studies of magnetic properties of thin microwires with low Curie temperature"**, J. Mag. Magn. Mat. 300, p. 16 (2006).

[4.10] L. Panina and D. Makhnovskiy, **"Microwave permittivity and permeability of magnetic wire composites"**, Phys. Status Solidi A 211, p. 1019 (2014).

[4.11] D. P. Makhnovskiy, L. V. Panina, C. Garcia, A. P. Zhukov, J. Gonzalez **Experimental demonstration of tunable scattering spectra at microwave frequencies in composite media containing CoFeCrSiB glass-coated amorphous ferromagnetic wires and comparison with theory** Phys. Rev. B 74 (2006), pp. 064205-15

[4.12] Wideband horn antenna П6-23М (0.85 – 17.44 GHz): http://mnipi.com/en/produkt/antennyi-izmeritelnyie/antenna-izmeritelnaya-p6-23m.html

[4.15] David Szondy. Gizmag. **"BAE Systems developing "smart skin" for aircraft"**. http://www.gizmag.com/bae-smartskin/33458/

[5.1] G. F. Engen, C. A. Hoer, **"Thru-Reflect-Line: An improved technique for calibrating the dual six-port automatic network analyser"**, IEEE Transactions on Microwave Theory and Techniques, Vol. 27, pp. 987-983, 1979.

[A.1] Worlder. **Worlder Travel Blog - Moldova.** (2007), Available: http://images.travelpod.com/users/worlder/2007-07-europe.1184534940.p1010064.jpg. Last accessed 01 Feb 2016.

Appendix A

Journey and stay in Chisinau, Republic of Moldova

On the 10th of April 2013, at midnight, I took a minibus ("Marshrutka") from my hometown Odessa, Ukraine, to Chisinau, Republic of Moldova. The distance between Odessa and Chisinau is around 130 miles (210 kilometres), and the journey time was approximately six hours. The driver of the minibus dropped me at the "Cosmos" hotel (www.hotel-cosmos.com), located at Constantin Negruzzi Square (Bulevardul Constantin Negruzzi).

"Cosmos" a 19-storey tower hotel, built between 1974 and 1983, is centrally located and offers great views of the surrounding city. It is close to the train station, shopping centres and restaurants. Several minibuses and trolleybuses stop next to the hotel, which can be used for intercity travel. Famous attractions such as Ştefan cel Mare Central Park (Parcul Ştefan cel Mare), the National Museum of History of Moldova (Muzeul Național de Istorie a Moldovei) and the Victory Memorial and Eternal Flame were just a few bus-stops away.

Fig. A.1. "Cosmos" hotel, featuring the architecture of the time [A.1].

During my stay at the hotel, the breakfast offered was wonderful, consisting of local Moldovan and continental European foods. The reception-staff were helpful, and thanks to them I was able to locate MFTI Ltd easily. In the evenings, several traditional restaurants located near the hotel were a great place to try local foods and wine. A buffet-style restaurant "Veranda" located a few minutes from the hotel was one of my favourite places for food and drink. The restaurant had a large selection of dishes at affordable prices, and is a great place for quick lunches and dinners. Popular East-European dishes such as Borsch (Борщ), a beetroot and beef soup, and Pelmeni (Пельмени), dumplings filled with minced meats, served at this restaurant were extremely tasty.

Journey from Chisinau, Republic of Moldova to Plymouth, United Kingdom.

On the following morning, at 06:00, I took a flight from Chisinau International Airport, Moldova, to Bucharest Henri Coandă International Airport. The aircraft on this route was a twin-turboprop "ATR 42" (Aerei da Trasporto Regionale 42). This was my first experience flying in a turboprop aircraft and on this flight I realised just how loud turboprop engines are. After a short wait in Bucharest, I caught my connecting flight to Heathrow Airport, London. The rest of the journey, to Plymouth, continued on a National Express coach.

Brief closing thoughts regarding this visit

This was a great starting point for my research project. I also enjoyed my free time in Chisinau. I had a great time in the city centre and visited various local restaurants and shopping malls. I was also able to visit local landmarks, parks and historical sites. I even enjoyed the feelings of Soviet-era nostalgia during my time in this city.

I would like to thank Dr Dmitriy Makhnovskiy for arranging this memorable visit. I would also like to thank Mr Vladimir Larin and his colleagues, for their hospitality and their time spent on making my visit to MFTI Ltd interesting and informative.

Appendix B

Algorithm (Fortran) for the calculation of the time delay

```
USE MSIMSLMD

INTEGER NS
REAL pi
PARAMETER (NS=5000)
! NS is the maximum number of frequency points
PARAMETER (pi=3.14159265358979323846264338327795)

REAL A(NS),argument(NS),delta,line(NS),ReS(NS),ImS(NS),f(NS)
REAL meanx,meany,Sxx,Sxy,vshift,alfa,deltat
INTEGER m,i

WRITE(*,*)'*****************************************************'
WRITE(*,*)''
WRITE(*,*)'The model used:'
WRITE(*,*)''
WRITE(*,*)'S=A(f)*exp(-i*alfa*f), where:'
WRITE(*,*)'f is the frequency'
WRITE(*,*)'A>0 is an amplitude factor'
WRITE(*,*)'alfa=2*pi*deltat is a positive parameter'
WRITE(*,*)'deltat is a time delay'
WRITE(*,*)''
WRITE(*,*)'Argument=alfa*f (rad) is the argument of exp.'
WRITE(*,*)''
WRITE(*,*)'The program calculates the 2D array {f, argument(f)}'
WRITE(*,*)'and then the delay time.'
WRITE(*,*)''
WRITE(*,*)'The input file must be named "S.txt".'
WRITE(*,*)''
WRITE(*,*)'The first column in S.txt is the frequency f'
WRITE(*,*)'measured in Hz.'
WRITE(*,*)'The second column is Re[S(f)].'
WRITE(*,*)'The third column is Im[S(f)].'
WRITE(*,*)'All numbers in this file are real'
WRITE(*,*)''
WRITE(*,*)'*****************************************************'
PAUSE

! Reading from the file
OPEN(10,FILE='S.txt')
DO m=1,NS
   READ(10,*) f(m),ReS(m),ImS(m)
END DO
CLOSE(10)

! Calculation of the amplitude factor
DO m=1,NS
   A(m)=SQRT(ReS(m)**2+ImS(m)**2)
END DO

! Calculation of the exponent argument
DO m=1,NS
   argument(m)=ATAN2(ImS(m),ReS(m))
END DO

! Assembly of the pieces of argument into a continuous line.
i=0
line(1)=argument(1)
IF(argument(5).LT.argument(1)) THEN
```

```
DO m=2,NS
   delta=ABS(argument(m)-argument(m-1))
   IF(delta.LE.pi) THEN
       line(m)=argument(m)-i*2.0*pi
   ELSE
       i=i+1
       line(m)=argument(m)-i*2.0*pi
   END IF
END DO

ELSE

DO m=2,NS
   delta=ABS(argument(m)-argument(m-1))
   IF(delta.LE.pi) THEN
       line(m)=argument(m)+i*2.0*pi
   ELSE
       i=i+1
       line(m)=argument(m)+i*2.0*pi
   END IF
END DO

END IF

! Recovery of the alfa parameter
! by means of the least-squares approximation.
meanx=0.0
DO m=1,NS
   meanx=meanx+f(m)
END DO
meanx=meanx/NS

meany=0.0
DO m=1,NS
   meany=meany+line(m)
END DO
meany=meany/NS

Sxx=0.0
DO m=1,NS
   Sxx=Sxx+f(m)**2
END DO
Sxx=Sxx-NS*meanx**2

Sxy=0.0
DO m=1,NS
   Sxy=Sxy+f(m)*line(m)
END DO
Sxy=Sxy-NS*meanx*meany

alfa=Sxy/Sxx
vshift=meany-alfa*meanx
deltat=ABS(alfa)/(2.0*pi)


WRITE(*,*)'*****************************************************'
WRITE(*,*)''
WRITE(*,*)'deltat=', deltat
WRITE(*,*)'vertical shift=', vshift
WRITE(*,*)''
WRITE(*,*)'*****************************************************'
PAUSE

WRITE(*,*)'*****************************************************'
WRITE(*,*)''
WRITE(*,*)'The output file is "line.txt"'
WRITE(*,*)'The first column is the frequency in Hz,'
WRITE(*,*)'and the second column is the argument in radians.'
WRITE(*,*)''
WRITE(*,*)'*****************************************************'
PAUSE

! Writing to the file.
OPEN(20,FILE='line.txt')
DO m=1,NS
   WRITE(20,*) f(m),line(m)
END DO
CLOSE(20)

STOP
END
```

Appendix C

Algorithm (Fortran) for the optimisation of Δt (see Eq. (4.20))

```
USE MSIMSLMD

INTEGER NS,N
REAL pi
COMPLEX iunit

PARAMETER (NS=5000)! Number of frequency points
PARAMETER (N=10000)! Number of steps in searching the global minimum
PARAMETER (pi=3.14159265358979323846264338327795)
PARAMETER (iunit=(0.0,1.0))! complex unit

! f - frequency (real array)
! ReSM - Real part of the measured S-parameter (real array)
! ImSM - Imaginary part of the measured S-parameter (real array)
! argument - argument of the measured S-parameter (real array)
! A - amplitude of the measured S-parameter (real array)
! SC - corrected S-parameter (complex array)

REAL A(NS),argument(NS),ReSM(NS),ImSM(NS),f(NS),step,Func(NS)
REAL Integral(N),min, deltata,error
COMPLEX SC(NS)
INTEGER m,k,flag

! Deltata is an estimation for the TDR time delay of the adapters
WRITE(*,*)'Enter an approximation for the time delay in ps'
READ(*,*) deltata
deltata=deltata*1.0E-12

! Error is a confidence interval for Deltata
WRITE(*,*)'Enter the error in ps (usually 5 ps)'
READ(*,*) error
error=error*1.0E-12

step=2.0*error/(N-1)

DO k=1,N

   delta=deltata-error+step*(k-1)

   OPEN(10,FILE='SM.txt')! Reading from the file
   DO m=1,NS
      READ(10,*) f(m),ReSM(m),ImSM(m)
   END DO
   CLOSE(10)

   DO m=1,NS
      A(m)=SQRT(ReSM(m)**2+ImSM(m)**2)
      argument(m)=ATAN2(ImSM(m),ReSM(m))
   END DO

   DO m=1,NS
      SC(m)=A(m)*CEXP(iunit*argument(m)+iunit*2.0*pi*f(m)*delta)
      Func(m)=ABS(A(m)-ABS(REAL(SC(m))))
   END DO

   ! Integration using the trapezium method
   Integral(k)=0.0
   DO m=1,NS-1
   Integral(k)=Integral(k)+(Func(m)+Func(m+1))*(f(m+1)-f(m))/2.0
   END DO
   Integral(k)=Integral(k)/(f(NS)-f(1))

END DO


OPEN(20,FILE='IntegValues.txt')! Writing to the file
DO k=1,N
   WRITE(20,*) k,Integral(k)
END DO
CLOSE(20)

! Global minimum
min=Integral(1)
DO k=2,N
   IF(Integral(k).LE.min) THEN
       min=Integral(k)
       flag=k
   ELSE
       CONTINUE
   END IF
END DO

delta=deltata-error+step*(flag-1)
WRITE(*,*)'Optimised time delay=',delta

PAUSE

STOP
END
```

Appendix D

Program code for TRL written in Fortan

```
      USE MSIMSLMD

      INTEGER N,k
      PARAMETER (N=1601)
      DOUBLE PRECISION f(N),x(N),y(N),flag
      DOUBLE COMPLEX unit,im
      PARAMETER (unit=(1.0,0.0),im=(0.0,1.0))
      DOUBLE COMPLEX SN11(N),SN12(N),SN21(N),SN22(N),STH11(N),STH12(N)
      DOUBLE COMPLEX STH21(N),STH22(N),SLINE11(N),SLINE12(N)
      DOUBLE COMPLEX SLINE21(N),SLINE22(N),SRE11(N),SRE22(N)
      DOUBLE COMPLEX t11,t12,t21,t22,h11,h12,h21,h22
      DOUBLE COMPLEX InvPTH(2,2),PLINE(2,2),PLTH(2,2)
      DOUBLE COMPLEX alfa(N),beta(N),hi(N),a(N),b(N),c(N),ror(N)
      DOUBLE COMPLEX root1,root2,D,hibeta,Ra,Rbeta,Ref,PD(2,2),PN(2,2)
      DOUBLE COMPLEX InvPA(2,2),InvPB(2,2),Res(2,2),Right(2,2),norm
      DOUBLE COMPLEX SA11(N),SA12(N),SA21(N),SA22(N)
      DOUBLE COMPLEX SB11(N),SB12(N),SB21(N),SB22(N)
      DOUBLE COMPLEX SD11(N),SD12(N),SD21(N),SD22(N)

c     **********************< Block A >*******************************
      OPEN(10,FILE='SN11.txt')
      OPEN(20,FILE='SN12.txt')
      OPEN(30,FILE='SN21.txt')
      OPEN(40,FILE='SN22.txt')
      OPEN(50,FILE='STH11.txt')
      OPEN(60,FILE='STH12.txt')
      OPEN(70,FILE='STH21.txt')
      OPEN(80,FILE='STH22.txt')
      OPEN(90,FILE='SLINE11.txt')
      OPEN(100,FILE='SLINE12.txt')
      OPEN(110,FILE='SLINE21.txt')
      OPEN(120,FILE='SLINE22.txt')
      OPEN(130,FILE='SRE11.txt')
      OPEN(140,FILE='SRE22.txt')

      DO k=1,N

         READ(10,*) f(k),x(k),y(k)
         SN11(k)=x(k)*unit+y(k)*im

         READ(20,*) f(k),x(k),y(k)
         SN12(k)=x(k)*unit+y(k)*im

         READ(30,*) f(k),x(k),y(k)
         SN21(k)=x(k)*unit+y(k)*im

         READ(40,*) f(k),x(k),y(k)
         SN22(k)=x(k)*unit+y(k)*im

         READ(50,*) f(k),x(k),y(k)
         STH11(k)=x(k)*unit+y(k)*im

         READ(60,*) f(k),x(k),y(k)
         STH12(k)=x(k)*unit+y(k)*im

         READ(70,*) f(k),x(k),y(k)
         STH21(k)=x(k)*unit+y(k)*im

         READ(80,*) f(k),x(k),y(k)
         STH22(k)=x(k)*unit+y(k)*im
```

```
      READ(90,*) f(k),x(k),y(k)
      SLINE11(k)=x(k)*unit+y(k)*im

      READ(100,*) f(k),x(k),y(k)
      SLINE12(k)=x(k)*unit+y(k)*im

      READ(110,*) f(k),x(k),y(k)
      SLINE21(k)=x(k)*unit+y(k)*im

      READ(120,*) f(k),x(k),y(k)
      SLINE22(k)=x(k)*unit+y(k)*im

      READ(130,*) f(k),x(k),y(k)
      SRE11(k)=x(k)*unit+y(k)*im

      READ(140,*) f(k),x(k),y(k)
      SRE22(k)=x(k)*unit+y(k)*im

    END DO

    CLOSE(10)
    CLOSE(20)
    CLOSE(30)
    CLOSE(40)
    CLOSE(50)
    CLOSE(60)
    CLOSE(70)
    CLOSE(80)
    CLOSE(90)
    CLOSE(100)
    CLOSE(110)
    CLOSE(120)
    CLOSE(130)
    CLOSE(140)

    DO k=1,N
c   **********************< Block B >*******************************
      InvPTH(1,1)=unit/STH21(k)
      InvPTH(1,2)=-STH22(k)/STH21(k)
      InvPTH(2,1)=STH11(k)/STH21(k)
      InvPTH(2,2)=(STH12(k)*STH21(k)-STH22(k)*STH11(k))/STH21(k)

c   **********************< Block C >*******************************
      PLINE(1,1)=(SLINE12(k)*SLINE21(k)-SLINE22(k)*SLINE11(k))
      PLINE(1,1)=PLINE(1,1)/SLINE12(k)
      PLINE(1,2)=SLINE22(k)/SLINE12(k)
      PLINE(2,1)=-SLINE11(k)/SLINE12(k)
      PLINE(2,2)=unit/SLINE12(k)

c   **********************< Block D >*******************************
      CALL CMM2x2(InvPTH,PLINE,PLTH)

      h11=PLTH(1,1)
      h12=PLTH(1,2)
      h21=PLTH(2,1)
      h22=PLTH(2,2)


c   **********************< Block E >*******************************
      t11=(STH12(k)*STH21(k)-STH22(k)*STH11(k))/STH12(k)
      t12=STH22(k)/STH12(k)
      t21=-STH11(k)/STH12(k)
      t22=unit/STH12(k)

c   **********************< Block F >*******************************
      D=(h11-h22)**2+4.0*h12*h21
      root1=(h22-h11+CDSQRT(D))/(2.0*h12)
      root2=(h22-h11-CDSQRT(D))/(2.0*h12)

      IF(CDABS(root1).LT.CDABS(root2)) THEN
          hibeta=root2
          alfa(k)=root1
      ELSE
          hibeta=root1
          alfa(k)=root2
      END IF

c   **********************< Block G >*******************************
      Ra=(t21+alfa(k)*t22)/(t11+alfa(k)*t12)
      Rbeta=(t11+alfa(k)*t12)/(hibeta*t22-t21)
      b(k)=(hibeta*t12-t11)/(hibeta*t22-t21)

c   **********************< Block H >*******************************
      root1=Rbeta*(SRE22(k)-b(k))*(hibeta+SRE11(k))
      root1=root1/((unit-Ra*SRE22(k))*(SRE11(k)-alfa(k)))
      root1=CDSQRT(root1)
      root2=-root1

      Ref=(SRE22(k)-b(k))/(root1*(unit-Ra*SRE22(k)))
c     WRITE(*,*)'Reflection=',Ref
c     PAUSE
      IF(DBLE(Ref).GT.0.0) THEN
          c(k)=root1
      ELSE
          c(k)=root2
      END IF

c   **********************< Block I >*******************************
      a(k)=-c(k)*Ra
      beta(k)=Rbeta/c(k)
      hi(k)=hibeta*beta(k)

c   **********************< Block J >*******************************
      ror(k)=t12/(c(k)*beta(k)+b(k))
      ror(k)=ror(k)+t22/(-alfa(k)*beta(k)+unit)
      ror(k)=ror(k)+t21/(-a(k)*hi(k)-alfa(k))
      ror(k)=ror(k)+t11/(c(k)*hi(k)-b(k)*alfa(k))
      ror(k)=ror(k)/4.0
c     write(*,*)'ro*r=',t12/(c(k)*beta(k)+b(k))
c     write(*,*)'ro*r=',t22/(-alfa(k)*beta+unit)
c     write(*,*)'ro*r=',t21/(-a(k)*hi(k)-alfa(k))
c     write(*,*)'ro*r=',t11/(c(k)*hi(k)-b(k)*alfa(k))
c     PAUSE

    END DO
```

```
      DO k=1,N
c     **********************< Block K >*******************************
         PN(1,1)=(SN12(k)*SN21(k)-SN22(k)*SN11(k))/SN12(k)
         PN(1,2)=SN22(k)/SN12(k)
         PN(2,1)=-SN11(k)/SN12(k)
         PN(2,2)=unit/SN12(k)

         InvPA(1,1)=unit
         InvPA(1,2)=-beta(k)
         InvPA(2,1)=alfa(k)
         InvPA(2,2)=hi(k)

         InvPB(1,1)=unit
         InvPB(1,2)=-b(k)
         InvPB(2,1)=a(k)
         InvPB(2,2)=c(k)

         CALL CMM2x2(PN,InvPA,Res)
         Right(1,1)=Res(1,1)
         Right(1,2)=Res(1,2)
         Right(2,1)=Res(2,1)
         Right(2,2)=Res(2,2)

         CALL CMM2x2(InvPB,Right,Res)
         norm=ror(k)*(hi(k)+alfa(k)*beta(k))*(c(k)+a(k)*b(k))
         PD(1,1)=Res(1,1)/norm
         PD(1,2)=Res(1,2)/norm
         PD(2,1)=Res(2,1)/norm
         PD(2,2)=Res(2,2)/norm
c     **********************< Block L >*******************************
         SD11(k)=-PD(2,1)/PD(2,2)
         SD12(k)=unit/PD(2,2)
         SD21(k)=PD(1,1)-PD(1,2)*PD(2,1)/PD(2,2)
         SD22(k)=PD(1,2)/PD(2,2)
c     **********************< Block M >*******************************
         SA11(k)=alfa(k)
         SA22(k)=beta(k)
         SA21(k)=hi(k)*CDSQRT(hi(k)+alfa(k)*beta(k))

         SB11(k)=a(k)
         SB22(k)=b(k)
         SB21(k)=c(k)*CDSQRT(c(k)+a(k)*b(k))

      END DO
c     **********************< Block N >*******************************
      CALL Arg(f,SA21,flag)
      DO k=1,N
         SA21(k)=SA21(k)*flag
         SA12(k)=SA21(k)
      END DO

      CALL Arg(f,SB21,flag)
      DO k=1,N
         SB21(k)=SB21(k)*flag
         SB12(k)=SB21(k)
      END DO


c     **********************< Block O >*******************************
      OPEN(150,FILE='SA11.txt')
      OPEN(160,FILE='SA12.txt')
      OPEN(170,FILE='SA21.txt')
      OPEN(180,FILE='SA22.txt')
      OPEN(190,FILE='SB11.txt')
      OPEN(200,FILE='SB12.txt')
      OPEN(210,FILE='SB21.txt')
      OPEN(220,FILE='SB22.txt')
      OPEN(230,FILE='SD11.txt')
      OPEN(240,FILE='SD12.txt')
      OPEN(250,FILE='SD21.txt')
      OPEN(260,FILE='SD22.txt')

      DO k=1,N

         WRITE(150,*) REAL(f(k)),REAL(SA11(k)),IMAG(SA11(k))
         WRITE(160,*) REAL(f(k)),REAL(SA12(k)),IMAG(SA12(k))
         WRITE(170,*) REAL(f(k)),REAL(SA21(k)),IMAG(SA21(k))
         WRITE(180,*) REAL(f(k)),REAL(SA22(k)),IMAG(SA22(k))
         WRITE(190,*) REAL(f(k)),REAL(SB11(k)),IMAG(SB11(k))
         WRITE(200,*) REAL(f(k)),REAL(SB12(k)),IMAG(SB12(k))
         WRITE(210,*) REAL(f(k)),REAL(SB21(k)),IMAG(SB21(k))
         WRITE(220,*) REAL(f(k)),REAL(SB22(k)),IMAG(SB22(k))
         WRITE(230,*) REAL(f(k)),REAL(SD11(k)),IMAG(SD11(k))
         WRITE(240,*) REAL(f(k)),REAL(SD12(k)),IMAG(SD12(k))
         WRITE(250,*) REAL(f(k)),REAL(SD21(k)),IMAG(SD21(k))
         WRITE(260,*) REAL(f(k)),REAL(SD22(k)),IMAG(SD22(k))

      END DO

      CLOSE(150)
      CLOSE(160)
      CLOSE(170)
      CLOSE(180)
      CLOSE(190)
      CLOSE(200)
      CLOSE(210)
      CLOSE(220)
      CLOSE(230)
      CLOSE(240)
      CLOSE(250)
      CLOSE(260)

      STOP
      END


      SUBROUTINE CMM2x2(A,B,C)
      DOUBLE COMPLEX A(2,2),B(2,2),C(2,2)

      C(1,1)=A(1,1)*B(1,1)+A(1,2)*B(2,1)
      C(1,2)=A(1,1)*B(1,2)+A(1,2)*B(2,2)
      C(2,1)=A(2,1)*B(1,1)+A(2,2)*B(2,1)
      C(2,2)=A(2,1)*B(1,2)+A(2,2)*B(2,2)

      RETURN
      END
```

```
      SUBROUTINE Arg(f,S,flag)

      INTEGER NS,m,i,spoint
      DOUBLE PRECISION pi,zero
      PARAMETER (NS=1601,spoint=5)
      PARAMETER (pi=3.14159265358979323846264338327795,zero=0.0)
      DOUBLE COMPLEX S(NS)
      DOUBLE PRECISION argument(NS),delta,line(NS)
      DOUBLE PRECISION ReS,ImS,f(NS),flag
      DOUBLE PRECISION meanx,meany,Sxx,Sxy,alfa,vshift

      DO m=1,NS
         ReS=DBLE(S(m))
         ImS=DIMAG(S(m))
         argument(m)=DATAN2(ImS,ReS)
      END DO

      i=0
      line(1)=argument(1)
      IF(argument(spoint).LT.argument(1)) THEN
          DO m=2,NS
             delta=DABS(argument(m)-argument(m-1))
             IF(delta.LE.pi) THEN
                 line(m)=argument(m)-i*2.0*pi
             ELSE
                 i=i+1
                 line(m)=argument(m)-i*2.0*pi
             END IF
          END DO
      ELSE
          DO m=2,NS
             delta=DABS(argument(m)-argument(m-1))
             IF(delta.LE.pi) THEN
                 line(m)=argument(m)+i*2.0*pi
             ELSE
                 i=i+1
                 line(m)=argument(m)+i*2.0*pi
             END IF
          END DO
      END IF

      meanx=0.0
      DO m=1,NS
         meanx=meanx+f(m)
      END DO
      meanx=meanx/NS

      meany=0.0
      DO m=1,NS
         meany=meany+line(m)
      END DO
      meany=meany/NS

      Sxx=0.0
      DO m=1,NS
         Sxx=Sxx+f(m)**2
      END DO
      Sxx=Sxx-NS*meanx**2


      Sxy=0.0
      DO m=1,NS
         Sxy=Sxy+f(m)*line(m)
      END DO
      Sxy=Sxy-NS*meanx*meany

      alfa=Sxy/Sxx
      vshift=meany-alfa*meanx
c     WRITE(*,*)'Initial phase for S-parameter = ',vshift
c     PAUSE

      IF(DABS(vshift).GT.pi/4.0) THEN
          flag=-1.0
      ELSE
          flag=1.0
      END IF

      RETURN

      END
```